POLITECNICO
MILANO 1863

SCUOLA DI INGEGNERIA INDUSTRIALE
E DELL'INFORMAZIONE

Templated synthesis of titanium dioxide sol-gel for water purification

Tesi di Laurea Magistrale in
Materials Engineering and Nanotechnology - Ingegneria dei Materiali e delle Nanotecnologie

Author: **Luca Alietti**

Student ID: 964919
Advisor: Prof. Maria Vittoria DIAMANTI
Academic Year: 2021-2022

Abstract

Water contamination resulting from dye-polluted industrial wastewater is an increasingly concerning topic, as it endangers the aquatic ecosystem. The research has been focusing on finding clean and sustainable ways to remove the pollutants dispersed in water. A promising solution has been found in photocatalytic materials, able to transform pollutants into harmless species. Moreover, the sol-gel route for the synthesis of such photocatalysts has been proven really versatile and effective. This work aimed at testing the photocatalytic activity of sol-gel synthesized titanium dioxide thin films, in order to find high performance formulations, while keeping the synthesis as sustainable and environmentally clean as possible. In the first chapter, the state of art concerning water pollution and the usage of titanium dioxide photocatalysts to overcome this issue was summarized. The main structures, properties, and the aspects of the sol-gel synthesis of such material were presented in detail. In particular, the effect of surfactants and nanocellulosic materials on the properties of the sol-gel and the produced thin films was described and further investigated in this work. Chapter 2 presented the materials and the procedures followed for the synthesis and testing of the TiO_2 sol-gels. The formulation was conducted varying different parameters such as the type of solvent, the amount of titanium precursor, the order of addition of the reagents and the type of templating agent. Three types of surfactants were used (sodium dodecyl sulfate, Lutensol ON70 and Ecosurf eh-3) and two types of nanocellulose were implemented in the sol-gel synthesis of TiO_2. Each formulation was naturally aged for maximum 8 weeks while performing tests every two weeks. The samples to be tested were all deposited with the dip-coating method onto glass substrates and annealed. They were subjected to a first two hours screening photocatalytic test, measuring the degradation of a rhodamine B solution. After the best samples were determined, they, alongside other samples, were subjected to a longer photocatalytic test, lasting 6 hours. To further characterize the prepared samples, Dynamic Light Scattering analysis and Scanning Electron Microscopy were used to determine the average particles size, inside the sol-gel, and to analyze the surface morphology of the dip-coated samples, respectively. In the third chapter, these results were shown and discussed. The photocatalytic tests revealed that the water and Ecosurf eh-3 based sol-gels were the best performing ones in terms of how quickly they could degrade the dye-polluted solution. Organic solvents based formulations were quite mediocre in terms of photoactivity, while presenting

better aesthetic appearance. In addition, the nanocellulose-based ones, were also not outstanding in terms of photocatalytic properties. In conclusion, this work contributed in finding new and well-performing solutions for the treatment of dye-polluted wastewater while also reducing the overall environmental impact of the materials synthesis by using non-toxic, weakly harmful and clean reagents to produce TiO_2 photocatalytic thin films.

Keywords: titanium dioxide, photocatalysis, sol-gel, surfactants, nanocellulose.

Abstract in lingua italiana

La contaminazione acquatica derivante dall'inquinamento da coloranti delle acque reflue industriali è un problema sempre più importante al quale la ricerca sta provando a trovare una soluzione che sia sostenibile e in grado di ridurne l'impatto. Promettenti in questo campo sono i materiali fotocatalitici, capaci di trasformare gli inquinanti in specie non pericolose. Questo lavoro di tesi si è posto come obiettivo il testare l'attività fotocatalitica di diversi rivestimenti contenenti biossido di titanio e sintetizzati tramite tecnologia sol-gel, con lo scopo ultimo di individuare le formulazioni migliori, mantenendo al contempo il processo di sintesi il più sostenibile possibile. Nel primo capitolo è stato riassunto lo stato dell'arte riguardante l'inquinamento delle acque e l'utilizzo di fotocatalizzatori a base di biossido di titanio per superare questo problema. Sono state presentate in dettaglio le principali strutture, le proprietà e gli aspetti della sintesi sol-gel di questi materiali. In particolare, l'effetto dei surfattanti e della nanocellulosa sulle proprietà del sol-gel e dei film sottili prodotti è stato descritto e poi successivamente approfondito in questo lavoro. Nel capitolo 2 sono stati presentati i materiali e le procedure seguite per la sintesi e la sperimentazione dei sol-gel di TiO_2. La formulazione è stata condotta variando diversi parametri come il tipo di solvente, la quantità di precursore, l'ordine di aggiunta dei reagenti e il tipo di agente "template". Tre differenti surfattanti (sodio dodecil solfato, Lutensol ON70 e Ecosurf eh-3) e due tipi di nanocellulosa sono stati utilizzati nella sintesi del TiO_2. Ciascuna formulazione è stata lasciata reagire per un massimo di 8 settimane, eseguendo test sui campioni ogni 2 settimane. Tutti i film sottili testati, sono stati prodotti tramite rivestimento ad immersione su substrati in vetro e successivamente ricotti. Inizialmene sono stati testati con un processo breve di degradazione fotocatalitica di una soluzione di rodamina B, della durata di 2 ore. Una volta identificati i campioni migliori, questi, assieme ad altri, sono stati testati tramite un processo di fotocatalisi più lungo, della durata di 6 ore. Per arricchire la caratterizzazione dei campioni prodotti, sono state condotte analisi con tecniche di diffusione dinamica della luce e di microscopia elettronica a scansione, per determinare, rispettivamente, il diametro medio delle particelle sintetizzate e la morfologia superficiale dei rivestimenti. Nel terzo capitolo, i risultati delle analisi sono stati riportati e discussi. I test di fotocatalisi hanno dimostrato come i sol-gel a base di acqua e Ecosurf eh-3 fossero i migliori nel degradare velocemente le soluzioni di colorante. Le formulazioni create usando solventi organici hanno mostrato risultati inferi-

ori, nonostante i rivestimenti fossero esteticamente eccellenti. Infine, anche quelle basate sulla nanocellulosa hanno portato a risultati relativamente mediocri. In conclusione, questo lavoro di tesi ha contribuito a individuare nuove e performanti soluzioni per il trattamento delle acque contaminate dai coloranti, mantenendo allo stesso tempo basso l'impatto ambientale legato alla sintesi dei film sottili di TiO_2, dato l'utilizzo di reagenti atossici, puri e poco pericolosi.

Parole chiave: biossido di titanio, fotocatalisi, sol-gel, surfattanti, nanocellulosa

Contents

Abstract **i**

Abstract in lingua italiana **iii**

Contents **v**

1 Introduction **1**

1.1 State of art: water pollution and treatments 1
1.2 Industrial dyes 2
1.2.1 Rhodamine B 3
1.3 Dye-pollutants disposal and degradation 4
1.3.1 Photocatalysis 5
1.4 Titianium dioxide 8
1.4.1 Crystalline structure 8
1.4.2 Electronic properties 10
1.4.3 Photocatalytic properties 11
1.4.4 Titanium dioxide applications 13
1.5 Sol-gel method 14
1.5.1 The metal alkoxide route 15
1.5.2 Precursors 17
1.5.3 Peptizing or chelating agents 19
1.5.4 Templating agents 20
1.5.5 Parameters influencing sol-gel formulations 21
1.6 Surfactants 23
1.6.1 Ionic surfactants 24
1.6.2 Non-ionic surfactants 25
1.6.3 Surfactants application in sol-gel chemistry 25
1.7 Nanocellulose 26

1.7.1 Cellulose . . . 27
1.7.2 Nanostructured cellulose production methods and properties . . . 27
1.7.3 Acid hydrolysis . . . 28
1.7.4 Nanocellulose in sol-gel technology . . . 29
1.8 Deposition techniques . . . 30
1.8.1 Dip-coating . . . 30
1.8.2 Calcination thermal treatment . . . 32
1.9 Noteworthy TiO_2 sol-gel formulations . . . 32

2 Materials and methods 35
2.1 Raw materials . . . 35
2.1.1 Precursor . . . 36
2.1.2 Solvents . . . 37
2.1.3 Catalyst . . . 38
2.1.4 Surfactants . . . 38
2.1.5 Templating agent . . . 40
2.1.6 Materials for nanocellulose synthesis . . . 41
2.2 Acid hydrolysis for nanocellulose synthesis . . . 42
2.3 Sol-gel nomenclature . . . 43
2.4 Sol-gel synthesis . . . 44
2.4.1 Normal addition method . . . 45
2.4.2 Reverse addition method . . . 46
2.4.3 Ultrasonication for accelerated condensation . . . 47
2.5 Deposition method: dip-coating . . . 48
2.6 Thermal treatment: calcination . . . 49
2.7 Photocatalytic degradation tests . . . 50
2.7.1 UV-LED photocatalytic degradation test . . . 50
2.7.2 UV-VIS photocatalytic degradation test . . . 53
2.7.3 Photolysis . . . 55
2.8 Samples characterization . . . 56
2.8.1 Scanning Electron Microscopy (SEM) . . . 56
2.8.2 Energy Dispersive X-Ray Spectroscopy (EDX) . . . 57
2.8.3 Dynamic Light Scattering (DLS) . . . 58

3 Results and discussion 61
3.1 Crystalline nanocellulose synthesis results . . . 61
3.2 Data collection methodology . . . 63
3.3 Photolysis results . . . 66

3.4 UV-VIS photocatalysis results and comparison 69
3.4.1 Isopropanol-based sol-gels 69
3.4.2 Ethanol-based sol-gels 79
3.4.3 Ultrasonicated sol-gels 82
3.4.4 Water-based sol-gels 84
3.5 UV-LED photocatalysis results and comparison 100
3.6 Sol-gels characterization 104
3.6.1 Dynamic Light Scattering 104
3.6.2 Scanning Electron Microscopy 109
3.7 Samples photoactivity trend 117

4 Conclusions and future perspectives **119**

Bibliography **121**

A Appendix A **131**

List of Figures **133**

List of Tables **139**

List of Symbols **141**

1 | Introduction

1.1. State of art: water pollution and treatments

Environmental pollution is surely one the biggest problems of the world of today. It is present in many different forms that concern mainly air and water contamination. The latter is particularly dangerous for the aquatic ecosystem, causing severe problems to plants and organisms. Among the many causes of water pollution, industrial wastewater containing high quantities and different kinds of dyes is one of the most prevalent.

Industrial colorants are often classified as harmful, toxic, non-biodegradable and even carcinogenic compounds [1, 2]. Many sectors make use of these colorants for various purposes that space from the application in paper, textile, plastics and apparel industries, to give a specific colour to the products, to the applications that exploit their other properties, such as fluorescence, in order to monitor the manufacturing processes [3]. Around 20% of the aforementioned dyes is reported to end up in the wastewater, mainly due to losses during synthesis and processing operations [2]. Furthermore, these compounds are very persistent in water and even small quantities (in the order of few ppms) are capable of changing the colour of the polluted water [1, 4]. In recent years, research has been focusing more and more on clean, effective and sustainable ways to reduce this dye-induced contamination. Nowadays, it is important also to match the sustainability standards in order to solve the problem of water pollution without introducing more waste into the environment and avoiding the usage of toxic or harmful products that may cause further issues. Many different approaches have been attempted to reach this goal: membrane filtration, adsorption techniques, ion-exchange removal, photocatalytic degradation and others [2]. Among those, photocatalysis stands out as a fast, efficient and reliable process. Filtration and adsorption approaches have flaws related to the efficacy of the filtration or to the mechanical stability of the adsorbant, as well as its need to be substituted or regenerated when saturated [2]. Photodegradation, on the other hand, has been proven to be a good method to reduce the concentration of pollutants in wastewaters, and it became continuously more prevalent in the research field, and, more recently, also in some industrial applications. The process is based on the use of a photocatalyst which is a semiconductor material able to absorb radiation and then catalyse the degradation reaction of the dye [1]. A material which is typically used for

this aim is titanium dioxide; more details about this and about the photocatalytic process will be explained further in this work.

TiO_2 can be synthesized in many different ways, one of which is the sol-gel method. This approach is quite simple and at the same time reliable, making it interesting from the research point of view [5, 6]. One of the aims of this work is to improve the synthesis of titanium sol-gels in order to obtain a stable and highly photoactive sol of TiO_2 nanoparticles, by modifying the standard formulation already produced in previous thesis works with surfactants and cellulose at the nano-scale.

1.2. Industrial dyes

Dyes can be classified with different criteria, which may depend on their chemical structure or their usage and application method. A classification made on the colorant usage is reported in the following:

- acid dyes: they are water-soluble anionic dyes that are used to dye protein fibers, such as wool and silk. They are called "acid dyes" because they require an acidic environment to bind to the fibers. Acid dyes are used in the textile industry to produce a wide range of colors, including bright and deep shades;
- basic dyes: these water-soluble dyes are used to dye synthetic fibers, such as nylon and acrylics. They are called "basic dyes" because they require a basic environment to bind to the fibers. Basic dyes are often used to produce bright and intense colors. They are used when brightness of shade was more important than the resistance to colour change or fading due to exposure to light sources or washing. These dyes are also referred as "cationic dyes" because they yield coloured cations in solution;
- disperse dyes: these dyes are used to dye synthetic fibers, such as polyester and acetate. They are called "disperse dyes" because they are insoluble in water and must be dispersed in a carrier fluid, such as hydrocarbons or phenols, before being applied to the fibers. Disperse dyes are often used to produce bright and deep shades;
- reactive dyes: these dyes are used to dye cellulosic fibers, such as cotton and rayon. They are called "reactive dyes" because they chemically react with the fibers to form a covalent bond. Dyes which contain azo groups (-N=N-) fall under this category. Reactive dyes are often used to produce a wide range of colors, including bright and pastel shades;
- vat dyes: these dyes are used to dye cellulosic fibers, such as cotton and linen. They are called "vat dyes" because they require a vatting process to become soluble in water to be

applied to the fibers. This process involves the reduction of the colorant in an alkaline bath, commonly done using sodium hydrogensulfite. Vat dyes are often used to produce deep and rich shades [3].

Another classification can be made based on the chemical nature of the dye, identifying inorganic or organic colorants. The former are typically made from inorganic compounds, such as metal salts or oxides, and are often used in the production of pigments and coloring agents for paints, ceramics, and plastics. On the other hand, organic dyes are typically derived from natural sources, such as plants or animals, or are synthesized using organic compounds, such as aromatic hydrocarbons or heterocyclic compounds. They are widely used in the textile, paper, and cosmetic industries [3]. The industries that are prevalently responsible for water pollution involving dye-contaminated wastewaters are the ones using mainly organic compounds. Rhodamine B falls under this category and, due to its importance in this research, it will be discussed more in details in the following section.

1.2.1. Rhodamine B

Rhodamine B is a synthetic organic basic (cationic) dye that belongs to the class of xanthene dyes. A xanthene dye is a type of synthetic organic dye that contains a xanthene ring as its chromophore. The xanthene ring is a rigid structure composed of three fused aromatic rings, which gives the dye its distinctive color and chemical properties [3]. The chemical structure of Rhodamine B (Figure 1.1) consists indeed of a xanthene core to which two diethylamino groups, responsible for the dye fluorescence properties, are attached [3, 7, 8].

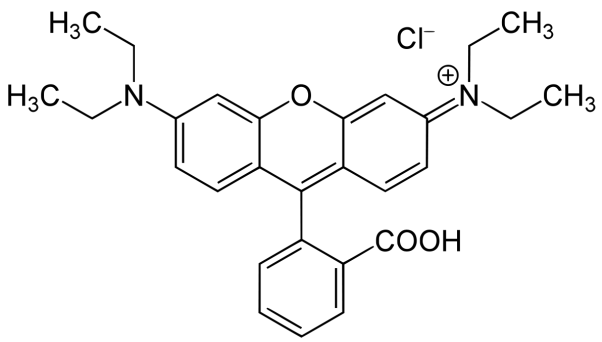

Figure 1.1: Rhodamine B chemical structure.

Rhodamine B is a versatile dye that is relatively cheap and easy to produce, which has contributed to its widespread use in industrial applications. Hence, it is commonly used as a dye for textiles, paper, and plastics. It can be used to dye a wide range of materials, including cotton, silk, wool, and nylon, and produces a bright and long-lasting pink to red color. The

dye is also used as a fluorescent tracer in the oil and gas industry, where it is injected into oil reservoirs to track the flow of fluids [3, 8]. Due to its extensive usage in industrial applications, it can end up being discharged into wastewater streams along with other pollutants, and if not properly treated, it can have adverse effects on aquatic life and ecosystems. Moreover, it is a non-biodegradable compound that is difficult to remove from wastewater using conventional treatment methods, such as coagulation, flocculation, and sedimentation. This is because it is highly stable and can persist in the environment for long periods, posing a risk of bioaccumulation and biomagnification in aquatic organisms [1, 9]. Also, rhodamine B and other industrial dyes can also impact the aesthetic quality of water bodies by imparting color and reducing clarity, which can have social and economic implications for local communities that rely on water resources [1].

Rhodamine B is often used for photocatalytic degradation tests because it is a highly stable dye that is difficult to degrade under normal conditions. This makes it a good candidate for testing the efficiency of photocatalytic degradation processes, which use a catalyst and light to break down organic compounds into smaller and less harmful molecules. Additionally, Rhodamine B has a well-defined absorption spectrum and emits strong fluorescence, which allows for easy monitoring of its degradation and the evaluation of the efficiency of the photocatalytic process. Moreover, Rhodamine B has been widely used as a model organic pollutant in studies of photocatalytic degradation processes, so the results obtained using this dye can be compared with those obtained in other studies, which helps to establish a common benchmark and facilitate the comparison of results [10].

1.3. Dye-pollutants disposal and degradation

Several treatments are available to reduce pollution caused by dye-contaminated wastewater. The main objectives are the removal of such pollutants from the water bodies and their degradation (mineralization) into non-harmful substances. The main processes to achieve these goals are summarized in Figure 1.2. Advanced oxidation processes (AOPs) are among the best in terms of effectiveness in degrading the colorants. Increasingly more interest is put towards these treatments in order to optimize them and making them also cost-effective [7]. Photocatalysis surely is one of the main AOPs widely researched for the degradation of organic dyes; indeed, it is central also to this work and will discussed in details in the following.

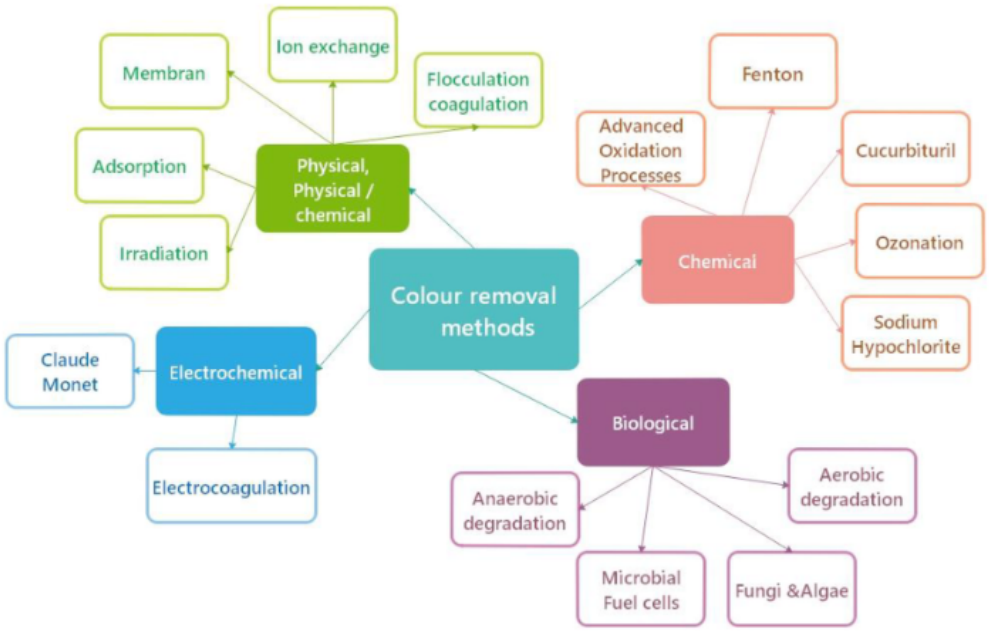

Figure 1.2: Main methods used for dye-polluted wastewater treatment [7].

1.3.1. Photocatalysis

In general, a photocatalyst is a material capable of absorbing light and accelerates a chemical reaction. Semiconductors are a class of materials typically employed in this field. They are in between conductors and insulators since they show an energy gap between the valence and conduction bands but this is not so big, allowing for the absorption of light in an accessible range of wavelengths (λ) (Figure 1.3) [11].

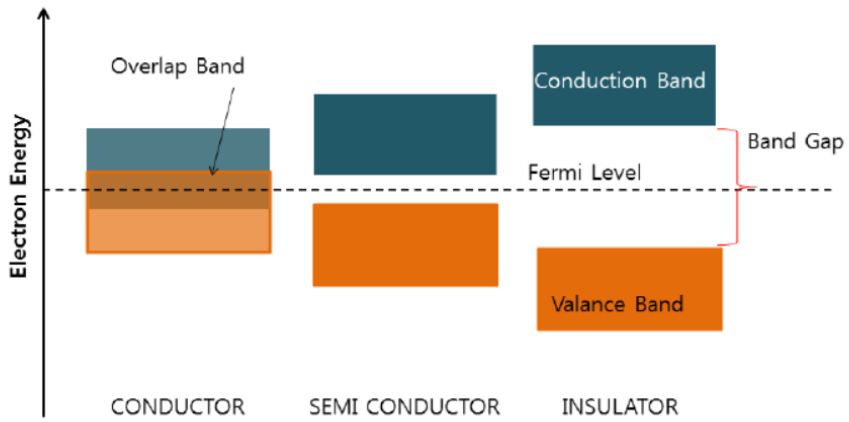

Figure 1.3: Valence and conduction bands in: conductors, semiconductors and insulators [12].

Typically used semiconductors for photocatalysis have band gaps that allow them to absorb visible or UV light. After absorbing a photon with an energy ($h\nu$) that matches the one of the gap, a photo-generated electron-hole pair is created. The absorption of the radiation promotes an electron to the conduction band (e_{CB}^-) while leaving an equivalently positively charged hole in the valence band (h_{VB}^+) (Equation (1.1)) (Figure 1.4) [13–16]..

$$Semiconductor + h\nu \rightarrow e_{CB}^- + h_{VB}^+ \tag{1.1}$$

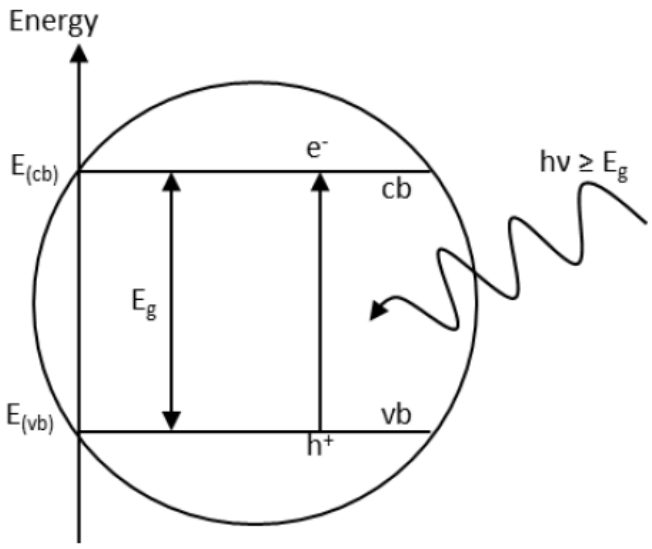

Figure 1.4: Schematic representation of the electron-hole pair through the absorption of light. (E_g=bandgap energy, vb=valence band, cb=conduction band) [11].

In presence of pollutant adsorbates onto the photocatalyst, the charge carriers can move to the surface of the catalyst and initiate the redox reaction. The positive holes are responsible for the production of $^{\bullet}OH$ radicals through the oxidation of water or OH^- (Equation (1.3)). These hydroxyl radicals are extremely reactive and can subsequently oxidize organic compounds, producing at the end CO_2 and H_2O (Equation (1.4)). On the other hand, electrons excited to the conduction band can be quickly trapped by the molecular oxygen adsrobed on the photocatalyst, which is then reduced to generate a superoxide radical anion (Equation (1.5)). This species, in presence of H^+ ions can further react to produce a hydroperoxyl radical (Equation (1.6)). The latter can undergo further electrochemical reduction yielding H_2O_2 (Equation (1.7)). The previously mentioned radicals can also enhance the degradation reaction of pollutants by creating new reaction pathways as shown in Equations (1.8) and (1.9) [13–16].

$$e^-_{CB} + h^+_{VB} \rightarrow energy \tag{1.2}$$

$$H_2O + h^+_{VB} \rightarrow {}^{\bullet}OH \tag{1.3}$$

$${}^{\bullet}OH + org.pollutant \rightarrow H_2O + CO_2 \tag{1.4}$$

$$O_2 + e^-_{CB} \rightarrow O_2^{\bullet -} \tag{1.5}$$

$$O_2^{\bullet -} + H^+ \rightarrow {}^{\bullet}OOH \tag{1.6}$$

$${}^{\bullet}OOH + {}^{\bullet}OOH \rightarrow H_2O_2 + O_2 \tag{1.7}$$

$$O_2^{\bullet -} + org.pollutant \rightarrow H_2O + CO_2 \tag{1.8}$$

$${}^{\bullet}OOH + org.pollutant \rightarrow H_2O + CO_2 \tag{1.9}$$

Photocatalysis can be used in many fields of application as summarized in Figure 1.5. The main advantages connected to this this advanced oxidation process are:

- the catalysts are usually non-toxic and reusable;
- the reaction byproducts can reach simply CO_2 and H_2O in case of complete mineralization;
- the degradation of dyes is non-selective, meaning that various pollutants can be degraded simultaneously;
- the activation mechanism is based on light (visible or UV) irradiation which is considered as a renewable source [17].

Overall, it is a versatile and clean process aimed at reducing water pollution and it is accessible through many different materials. In the context of this work, titanium dioxide is furtherly investigated for its role as a photocatalytic material.

Figure 1.5: Fields of application of photocatalysis [18].

1.4. Titianium dioxide

Titanium belongs to the IVA group of elements and is widely distributed in the Earth's crust, it is in fact the ninth most abundant. Its average concentration in the crust of the planet is 4400 mg/kg (ca. 0.6% by weight) [19, 20]. Due to its high affinity to oxygen, Ti does not exist in the pure metallic state in nature, in fact it is mostly found in its +4 oxidation state; also the +3 and +2 states exist even though they are far less common. Moreover, Ti^{2+} and Ti^{3+} compounds are readily oxidized to the tetravalent state by air, water, and other oxidizing agents [19]. TiO_2 is the natural occuring oxide form of Ti and it also known as Titanium (IV) oxide, titania or Ti white [21].

1.4.1. Crystalline structure

Titanium dioxide can exhibit three different polymorph structures: rutile, anatase, and brookite. In nature, the only stable occuring one is rutile. On the other hand, anatase and brookite are metastable and, in particular, the latter is rarely researched due to its synthesis being fairly difficult to perform [20]. In all the three forms titanium (Ti^{4+}) atoms are coordinated to six oxygen (O^{2-}) atoms to form an octahedral structure (TiO_6) (Figure 1.6).

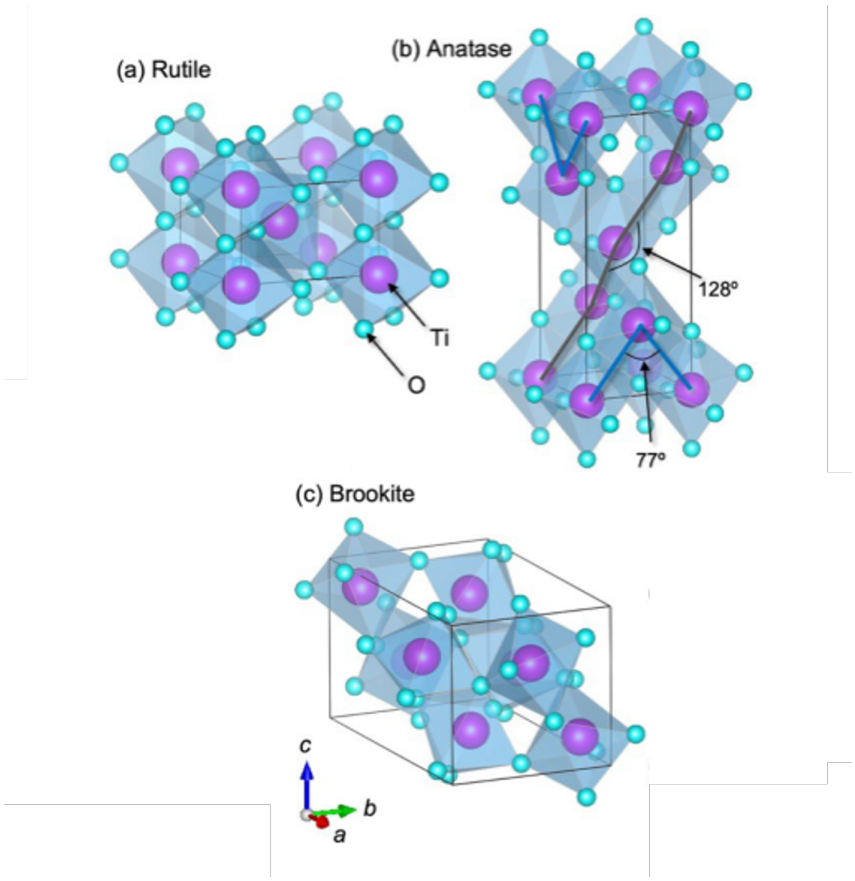

Figure 1.6: Crystal structures of TiO_2 three polymorphs: (a) rutile; (b) anatase; (c) brookite [22].

Rutile and anatase show a tetragonal geomatry while brookite exhibit an orthorombic one. More in details, rutile consists in a slightly distorted TiO_6 octahedron while anatase structure is made by highly distorted octahedral units. Moreover, each octahedral unit of the rutile structure is surrounded by ten close octahedrons; instead, anatase units are in contact with eight neighbour octahedrons. For these two polymorphs there are also differences in the Ti-Ti and Ti-O bonds length. For anatase the first one is longer than rutile one, while the latter is instead shorter for anatase with respect to rutile (Table 1.1). This discrepancy is reflected in these polymorphs having distinct mass densities; indeed, anatase and also brookite are the less dense structures. Their metastable nature causes them to convert to rutile phase and this effect is enhanced and sped up by thermal treatments at temperatures between 400°C and 1200°C, depending on parameters such as TiO_2 synthesis method and heat flow conditions [23, 24]. In particular, the anatase to rutile conversion is reconstructive and irreversible since it involves the breaking and reforming of the material bonds. The TiO_2 phase is the main factor influencing the material final properties, hence, researching the various aspects of polymorph-to-polymorph transitions is of fundamental importance [24]. Among the different forms of titanium dioxide, anatase and rutile

are the most used in various fields of application while brookite, given its large cell volume and synthesis complexity, is barely present in research literature [23, 24].

Table 1.1: TiO_2 polymorphs main properties [20, 23].

Property	Rutile	Anatase	Brookite
Refractive index	2.72	2.52	2.63
Dielectric constant	114	31	-
Crystal lattice	Tetragonal	Tetragonal	Orthorhombic
Lattice constant ($\AA$)	a=b=4593 c=2959	a=b=3784 c=9515	a=9184 b=5447 c=5145
Molecule per cell	2	4	8
Volume ($\AA^3$)	62.07	136.25	257.38
Density (g/cm^3)	4.13	3.79	3.99

1.4.2. Electronic properties

Titanium dioxide is classified as a wide bandgap semiconductor with values that change depending on the specific crystalline phase: 3.02 for rutile, 3.2 for anatase and 2.96 for brookite. TiO_2 is also a n-type semiconducting material due to oxygen vacancies being the most prevalent defect inside its crystalline structure (Figure 1.7).

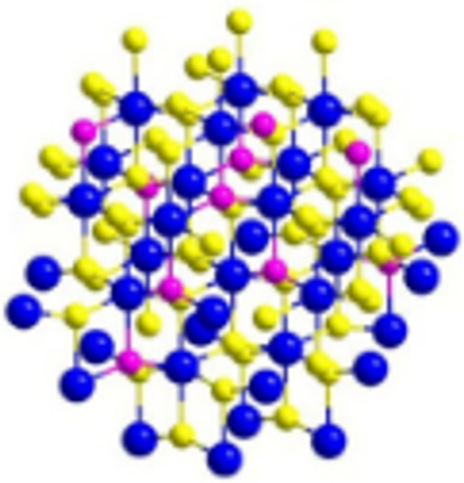

Figure 1.7: Oxygen vacancies (coloured in magenta) present inside the crystal lattice of TiO_2. Ti atoms are coloured in blue and O atoms are coloured in yellow [25].

In general, the electronic behaviour is deeply connected to the crystal structure and the material composition. Structural defects are inevitably present in every polycrystalline material. Point defects occur when atoms are missing from their constituent position in the lattice (vacancies) or when external atoms occupy the empty space in between atomic sites (interstitials). These defects contribute to the electrical properties of the material in two ways: providing ionization to it or producing an ionic current in response to the application of an external electric field. Oxygen vacancies occur when oxygen atoms are missing from the TiO_2 crystal lattice, leaving behind an electron that can contribute to the electronic properties of the material. These electrons act as shallow donor states, introducing additional electrons into the conduction band of the TiO_2 material and increasing its electrical conductivity [23, 25]. The n-type nature of titanium dioxide means that the majority carrier is the negatively charged electron. When TiO_2 is illuminated with light that has sufficient energy to generate electron-hole pairs, these electrons can be excited from the valence band to the conduction band, increasing the number of free electrons available to participate in electrical conduction [23, 25]. This last concept is also key to the photocatalytic properties of titanium dioxide and will be discussed more in details in the next sub-section.

1.4.3. Photocatalytic properties

Titanium dioxide photocatalytic capabilities became an increasingly researched topic after the discovery made by Fujima and Honda in 1972 about the possibility of splitting water into oxygen and hydrogen using TiO_2 semiconductor materials in a photo-electrochemical cell [13]. The semiconducting nature of titanium dioxide allows it to interact and absorb light radiation possessing sufficient energy (or wavelength) to create reactive oxidizing species (ROS) able to cause the photocatalytic degradation of pollutants. As seen before, the light energy must be enough to match the material bandgap; in the case of TiO_2 and in particular anatase, UV radiation ($\lambda \leq 390$ nm) is needed to match the gap of 3.2 eV. The absorption of a photon is able to excite an electron to the conduction band (${e_{CB}}^-$) leaving behind a positive hole in the valence band (${h_{VB}}^+$); this can be written in the compact form of Equation (1.10) [13].

$$TiO_2 + h\nu \rightarrow e^-_{CB} + h^+_{VB} \tag{1.10}$$

The photo-generated charge carriers can either be trapped as Ti^{3+} and O^{2-} in the lattice of the material or recombine with a consequent energy dissipation (Equation (1.2)), the latter representing the main limiting factor in semiconductor photocatalysis [13, 14]. The subsequent steps were already reported in 1.3.1. In Figure 1.8 the photocatalytic reactions are visually summarized.

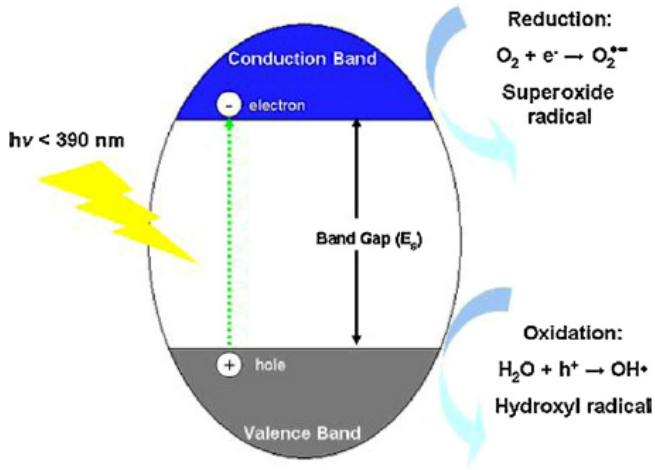

Figure 1.8: Schematic representation of the TiO_2 photocatalytic process [13].

It has to be underlined that the charge carriers dynamics, hence the photocatalytic activity of titanium dioxide, is strongly related to the crystalline structure. Indeed, it has been demonstrated that the anatase phase shows an higher photoactivity compared to the rutile phase. This is because the overall reaction efficiency is determined by the rate of the oxidation reaction (which depends on the amount of photo-generated charge carriers) and the rate of the electron-hole recombination. These are strongly related to the carriers dynamics which is inherently influenced by the potential barrier present in the subsurface region of the photocatalyst, in the so called space charge layer (SCL). This barrier is responsible for the TiO_2 band structure bending. Its effect is negligible for systems (TiO_2 particles) with dimensions lower than 10 nm while it becomes fundamental for systems with sizes bigger than 20 nm. The band bending is higher in the case of anatase resulting in an higher relaxation time for the charge carriers (due to the surface hole trapping); on the other hand, rutile surface band bending is lower, leading to a quicker bulk charge recombination. This difference in the lifetime of the photo-generated carriers is maintained also at the smaller nanoscale showing the intrinsic nature of this disparity in photoactivity between the two polymorphs and highlighting the fundamental role of the TiO_2 surface defects [26]. The photocatalytic performance of titanium dioxide is influenced by many factors including the more intrinsic one mentioned above, but also:

- particle size and structure, which influence the amount of adsorbate, hence the rate of reaction;
- surface area, which again determines the size of the exposed area useful for the reaction;
- concentration of the pollutant solution: higher initial concentrations usually lead to slower reaction kinetics while keeping a fixed amount of catalyst;

- pH: the acidic or alkaline nature of the solution can influence the surface charge of TiO_2, resulting in different adsorpion efficiency;
- reaction temperature, which is strictly connected to the reaction rate;
- light intensity and irradiation time [2].

Overall, titanium dioxide is an advantageous material to be used as a photocatalyst due to a good trade-off between the efficiency of the reaction, the stability of the material, and the low cost [2, 27].

1.4.4. Titanium dioxide applications

Titanium dioxide, due to its versatility, is widely employed in many different applications. TiO_2 is commonly used as a white pigment, able to produce excellent opacity and brightness while being also very stable to the UV and solar radiation. These characteristics make it suitable for industrial sectors like:

- paints and coatings;
- plastics, where the light stability improves the weathering resistance of the products;
- textiles;
- ceramics;
- cosmetics, in particular in sunscreen, again, for its UV-blocking properties [28, 29].

Titanium dioxide is used also as a filler element in adhesives and paper production. However, the interest shown towards this material in advanced scientific and industrial applications focuses on its nanometric form. TiO_2 nanoparticles and thin films are widely employed in the field of catalysis and most importantly photocatalysis. Titanium dioxide is very important in the chemical sector as a catalyst for the water splitting reaction. Its photocatalytic properties, previously mentioned in this work, make it a suitable material for a plethora of applications, some of them are shown in Table 1.2 [28].

Table 1.2: The main applications exploiting TiO_2 photocatalytic properties [28].

Self-cleaning	Material for residential and office buildings	Exterior tiles, kitchen and bathroom components, interior furnishings, plastic surfaces, building stones
	Indoor and outdoor lamps and related systems	Translucent paper for indoor lamp covers, coatings on fluorescent lamps and highway tunnel lamp cover glass
	Materials for roads	Tunnel wall, soundproofed wall, traffic signs and reflectors
	Others	Tent material, clothes for hospital garments and uniforms and spray coating for cars
Air-cleaning	Indoor air cleaners	Room air cleaner, photocatalyst-equipped air conditioners and interior air cleaner for factories
	Outdoor air purifiers	Concrete for highways, roadways or footpaths, tunnel walls, soundproofed walls and building
Water disinfection	Drinking water	Purification river water, groundwater, lakes and water storage tanks
	Others	Fish feeding tanks, drainage water and industrial wastewater
Antitumor activity	Cancer therapy	Endoscopic-like instruments
Self-sterilizing	Hospital tiles	To cover the floor and walls of operating rooms, silicone rubber for medical catheters and hospital garments and uniforms

Other important fields of application of titanium dioxide are dye-sensitized solar cells (DSSCs), where it is used mostly as an electrodic material, and gas-sensors, where the presence of oxygen vacancies in the lattice structure has a key role [11].

Nanometric TiO_2 is surely central for the aim of this work, in particular for its photocatalytic applications. The advantages connected to this material in terms of anti-pollution, non-toxicity and sustainability are very promising. For these reasons, cleaner and efficient synthesis routes have been researched and will be discussed in details further in this thesis.

1.5. Sol-gel method

The sol-gel method is a versatile wet chemical technique used to make several types of organic or inorganic polymers and ceramic materials [30]. A typical sol-gel process involves the formation of a colloidal suspension (a sol) through the subsequent reactions of hydrolysis and polymerization of a precursor which is typically an inorganic metal salt or a metal-organic compound, like a metal alkoxide (in this case the bulk sol-gel process is referred as "the alkoxide route"). After complete polymerization, an integrated network is formed and it takes the name of "gel". The sol is defined as a dispersion of one phase into another, where 1-1000 nm sized particles are dispersed in a wet medium [11, 23, 30]. On the other hand, the gel is a sponge-like solid whose pores are filled with the liquid phase [23]. This technique is particularly popular due to the several advantages it offers:

- it allows the production of high purity and homogeneity materials;
- it does not require high temperatures and pressures to be performed;
- it allows for complex shapes and geometries to be easily and homogeneously coated;

- it enables a good control of the reaction and deposition parameters such as the microstructure of the final coating or the ease in adding doping elements [11, 23].

In the following, a more detailed description of the metal alkoxide route will be presented, highlighting the reactions involve and the steps to reach the nanostructured product.

1.5.1. The metal alkoxide route

The metal alkoxide process involves several reactions and steps, which are explained in detail below:

1. Hydrolysis reaction: the first step in the metal alkoxide process is the hydrolysis of metal alkoxides. These are soluble compounds which are formed by the reaction of a metal oxide with an alcohol. The general formula for a metal alkoxide is $M(OR)_n$, where M is the metal, R is the alkyl group (C_nH_{2n+1}), and n is the number of alkoxide groups. The hydrolysis reaction involves the reaction of the metal alkoxide with water or with an OH-bearing organic solvent to form a metal hydroxide and an alcohol (Equation (1.11)) [11, 30, 31].

$$M(OR)_n + H_2O \rightarrow MOH + {}_nROH \tag{1.11}$$

   The hydrolysis step is usually carried out in the presence of an acid or a base catalyst to increase the rate of reaction;

2. Condensation reaction: the second step is the condensation of metal hydroxides to form a sol. The metal hydroxides formed in the hydrolysis reaction are unstable and tend to condense to form metal oxide oligomers. The condensation reaction involves the reaction of the previously formed metal hydroxides with each other or with the former alkoxides to form M-O-M bonds (Equations (1.12) and (1.13)) [11, 30, 31].

$$M(OH)_n + M(OH)_n \rightarrow M - O - M + {}_nROH \quad (alcohol\ condensation) \tag{1.12}$$

$$M(OH)_n + M(OR)_n \rightarrow M - O - M + H_2O \quad (water\ condensation) \tag{1.13}$$

   The produced metal oxide oligomers are the fundamental building blocks of the porous interconnected network. While the condensation reaction proceeds, the gel starts forming and the overall viscosity of the solution increases [11, 31]. The final product of the first two reactions is strongly influenced by several factors such as: reactivity of the metal alkoxide, temperature and pH of the reaction medium, amount of water or HO-bearing

species present in the reaction, and presence of additives [11];

3. Ageing: the sol is then aged to form a gel. This process allows the metal oxide oligomers to continue to condense and cross-link to form a more compact and less porous three-dimensional network structure. The ageing process is usually carried out at room temperature and can take several days, depending on the type of metal alkoxide and the solvent used [31];

4. Drying: the gel is then dried to remove the solvent and any unreacted reagents. Different drying methods can be used, including atmospheric/thermal drying, supercritical drying, and freeze-drying, each of which has different effects on the gel network structure. High-temperature heating of the porous gel leads to densification, resulting in the removal of pores and the production of a xerogel. However, the xerogel has a relatively low surface area and pore volume, and the gel may experience high shrinkage. In contrast, supercritical drying produces aerogels that have a high pore volume and surface area, and the original gel network remains mostly intact. The third drying method involves freezing the solvents to form a cryogel, which experiences relatively lower shrinkage than xerogel [31–33];

5. Calcination: the dried gel is then calcined at a high temperature to form the final ceramic nanoparticles. Calcination involves the removal of any remaining organic material and the transformation of the metal oxide oligomers to form the crystalline ceramic nanoparticles. The calcination temperature and time depend on the type of ceramic and the desired particle size and morphology [11, 31].

The different reaction steps involved in the sol-gel process are summarized in Figure 1.9.

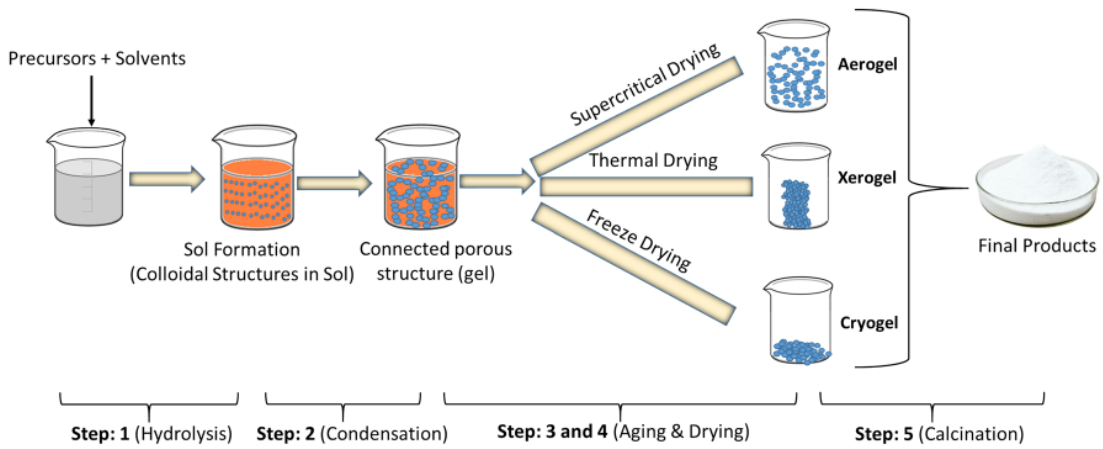

Figure 1.9: Steps of the sol-gel method for the preparation of metal oxide nanoparticles [31].

Moreover, the versatility of the sol-gel method allows for a wide variety of final products, made by tailoring the reaction and deposition paths after the sol formation. Some examples are:

- dip- or spray-coated substrates which are then calcined to obtain dense films;
- precipitation to obtain ultra-fine particles arrays;
- spin-coated ceramic fibers [11, 30, 34].

These last examples are visually grouped and summarized in Figure 1.10.

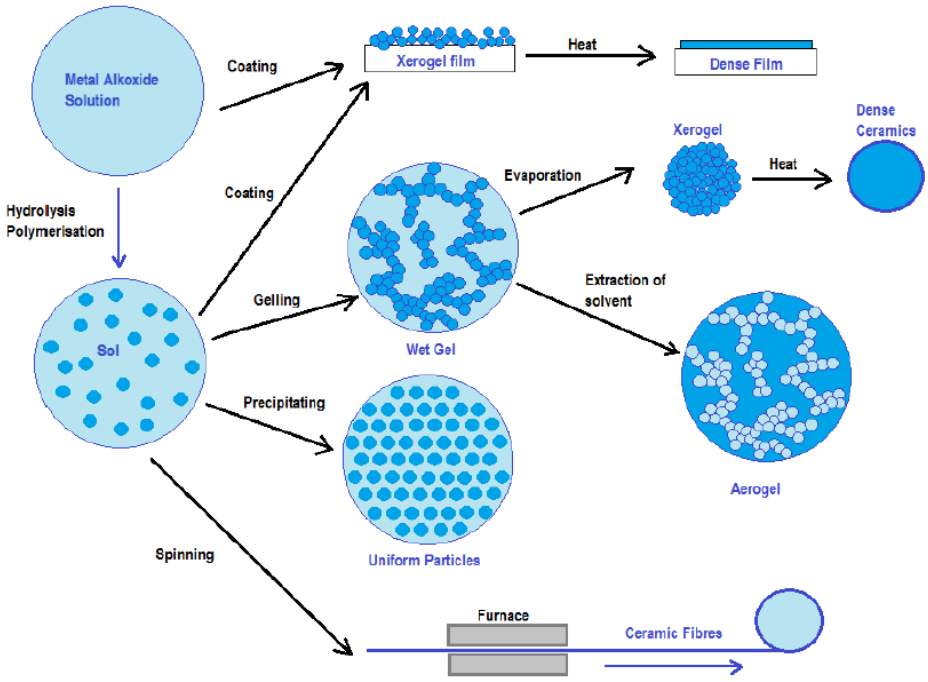

Figure 1.10: Scheme of the possible sol-gel process routes and steps to tailor the final product's morphology [11].

The dip-coating deposition technique will be subject of further discussion later in this work due to its central role in samples preparation. Now the main components of a sol-gel reaction will be presented more in detail.

1.5.2. Precursors

Due to the widespread use of the alkoxide sol-gel method, the most important precursors are metal alkoxides. Their main characteristic is the high reactivity of the M-O-R (where M is the metal and R is the alkyl group C_nH_{2n+1}) towards OH-bearing solvents, most importantly water, to readily produce the metal hydroxide molecule alongside with an alcohol, as it was reported

previously [11, 35, 36]. There are, however, more features that make these compounds suitable for the sol-gel preparation of nanoparticles. The most relevant aspects are:

- the ionic character of the M-O bond: the metal element influences the electronegativity difference of the bond, which is then reflected in variations in reactivity and solubility. The polar character of the metal-oxygen and oxygen-carbon bonds is what determines the high reactivity towards the hydrolysis reaction;
- the effect of the alkyl chain, which again determines the reactivity of the bond. In particular, the R group can modify the polarity of the O-R bond through the donation or subtraction of electronic charges;
- the nature and dimension of the alkyl substituent: the dimension of the R group is directly connected to its steric hindrance, and this affects the level of alkoxide-oligomerization. In general, higher bulkiness and branching of the akyl chain lead to a decrease in the degree of association of the alkoxide molecules. This is directly reflected in variations regarding the sol-gel process, affecting the molecular-level homogeneity of the system;
- the nature and size of the metal atom: alongside with the last point, also the dimension of the M atom affects the degree of alkoxide oligomerization. In particular, bigger atoms have stronger tendency in increasing the coordination number, hence, the degree of association increases [35]

Alongside with these chemical characteristics, also some physical properties of metal alkoxides are fundamental for their central role in sol-gel technology. Examples of these are:

- solubility: metal alkoxides are soluble in many organic solvents, such as ethanol and isopropanol. This makes them easy to dissolve and allows for easy handling and processing in the sol-gel technique;
- low molecular weight (depending on the R chain length): metal alkoxides have a relatively low molecular weight, making them easy to handle and react in the sol-gel process. The low molecular weight also allows for the formation of nanoparticles with controlled properties, such as particle size and shape;
- volatility: this is strictly connected to the last point. The high volatility in metal alkoxides is significant because it facilitates the production of pure precursors through distillation. Nonetheless, this property should be considered during the sol-gel synthesis to prevent undesirable alterations in composition in multi-component solutions.
- stability: metal alkoxides are stable under certain conditions, such as dry and air-free conditions. This characteristic makes them suitable for long-term storage [35, 36].

Metal alkoxides are also very versatile from the production point of view, as they can be synthesized from various metals and various types of alcohols, leading to a wide range of compounds with different properties.

Sol-gel preparations utilize not only alkoxides as precursors, but also inorganic and organic salts. The introduction of certain oxides in multi-component systems is achieved through the use of these salts, especially in cases where the use of alkoxides may not be feasible or required. The utilization of these alternatives to alkoxides entails a distinct chemistry that presents several challenges, including the elimination of anions from the system. Overall, this may lead to various differences in the chemical and physical properties, as well as the structure and microstructure of the final products. The most used inorganic salts are:

- nitrates: they are mainly used to introduce elements from the I and II groups into the sol-gel. They are used in alternative to the corresponding alkoxides due to them having lower solubility in their parent alcohol. Nitrates can however lead to issues regarding the crystallization of the gel during the drying step [35];
- chlorides: also chlorides are used instead of the corresponding alkoxides to overcome solubility issues. They are also cheaper but they require acidic environments (with the addition of peptizing agents such as H_3PO_4) to allow the formation of a sol-gel due to high gelation rates in basic solutions [35].

On the other hand, the most relevant organic salts are:

- carboxylates: the chemical properties of carboxylate salts can enhance the hydrolysis reaction, leading to the formation of hydroxides and free acid. Additionally, the range of bonding modes between -COO^- and metal ions, such as ionic, bridging, and chelate bonds, can be advantageous in achieving homogeneous gels in multi-component systems. Moreover, acetates of the I and II groups metals are favorable precursors due to their water solubility, low volatility, and facile purification by crystallization from solutions. Additionally, they undergo thermal decomposition between 150 to 450°C to produce oxides [35];
- acetylacetonates: the main advantage connected to these complex precursors is the high thermal and kinetic stability [35].

1.5.3. Peptizing or chelating agents

In sol-gel chemistry, peptization is the process responsible for the dispersion of agglomerated particles to form a stable colloidal suspension by adding a controlled amount of electrolyte which takes the name of peptizing agent (or chelating agent). Upon addition to the sol, the

peptizing agent undergoes dissociation into its constituent ions which subsequently adsorb onto the surface of the particles, forming a layer that induces repulsive forces among them. The thickness of this layer is determined by the concentration of peptizing agent and the duration of the peptization process. As the adsorbed layer thickens, the distance between the particles increases, leading to the creation of larger pores [37, 38]. Common peptizing agents used in sol-gel formulations include acids (such as hydrochloric acid or acetic acid), bases (such as ammonia or sodium hydroxide), surfactants (such as cetyltrimethylammonium bromide), polymers (such as polyethylene glycol or polyvinyl alcohol), and, to some extent, organic solvents [39]. Articles in literature report the beneficial effect of peptization in titanium dioxide sol-gels comparing it with the unpeptized ones. In the case of acid chelating agents, H^+ ions are readily adsorbed onto the surface of TiO_2 particles; due to them having the same surface charge, they are repelled through the so called "double-layer repulsion effect", leading at the end to a stable sol formation with minimum levels of aggregation. On the other hand, unpeptized sol-gels show strong particles agglomeration in non-uniform clusters [40]. Surfactants and their role in the sol-gel chemistry will be discussed more in detail later in this work due to their importance in the sol-gel synthesis optimization.

1.5.4. Templating agents

Templating agents are organic or inorganic molecules that are used to control the size, shape, and texture of the resulting materials during the sol-gel process. The main usage of such agents is for the production of mesoporous structures because they are able to create a supporting structure for the nanoparticles and leave controlled porosity after their removal [23, 41, 42]. Templating agents are mainly classified into two types:

- soft templates: they are typically organic molecules that are incorporated into the sol-gel precursor solution, where they assemble into micelles or other structures that guide the growth of the sol-gel material. The organic template is subsequently removed from the final material by heating or washing. The advantages of using soft templates include their ability to create materials with moderately controlled morphologies and pore structures, as well as their ease of removal from the final material. However, the main disadvantage is that they can be difficult to control, and the resulting materials may have a higher degree of disorder compared to those synthesized using hard templates. Examples of soft templates are amphiphilic molecules like surfactants (ionic or non-ionic), block copolymers, and other organic molecules [23, 41, 42];
- hard templates: these are usually pre-formed solid particles that are used as molds for the synthesis of sol-gel materials. The shape and size of the template determine the morphol-

ogy and size of the sol-gel material that is formed around it. The template is subsequently removed from the final material by chemical (extraction techniques, dissolution) or physical (annealing) means, leaving behind the desired morphology. The advantages of using hard templates include the ability to create highly ordered and controlled morphologies, as well as the ability to synthesize nanocomposite materials. However, the main disadvantage is that they can be difficult to remove from the final material, which can result in residual impurities or defects. Examples of hard templates are: pre-formed nanoparticles, nanocrystalline cellulose, and other porous solids [23, 41, 43, 44].

In Figure 1.11 the two routes of soft- and hard-templating to obtain mesoporous titanium dioxide via the sol-gel technology are visually summarized and can be extended to other metal oxides preparation.

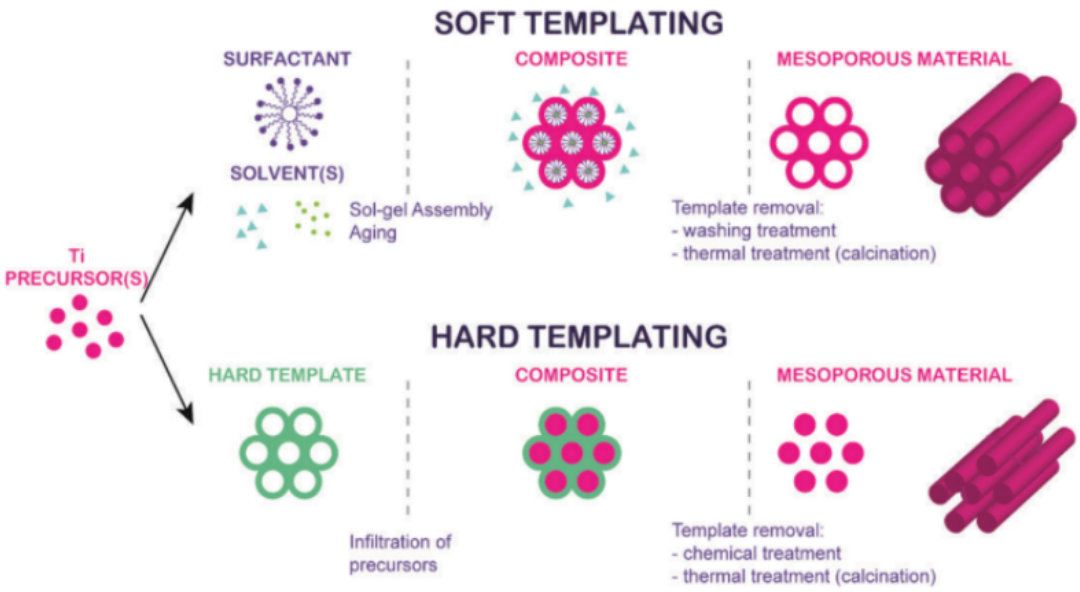

Figure 1.11: Scheme of the soft and hard template-assisted synthesis of TiO_2 controlled mesoporous strcutures [41].

As previously said, surfactants and also nanocellulose (and their employment in sol-gel formulation) will be analyzed more in depth in subsequent sections due to their central role in this research work.

1.5.5. Parameters influencing sol-gel formulations

The features of a sol-gel formulation are strongly dependent on several parameters that will be reported below, which determine the structure of the synthesized nanoparticles, hence the

properties of the final product coated with the solution.

- Precursor type: the nature of the precursor influences the solubility in the liquid solvent and the reactivity towards the reactions of hydrolysis and condensation, ultimately affecting the size, morphology, and chemical composition of the final particles. As seen before, the precursor is typically a metal alkoxide, which is a compound containing a metal ion bonded to an organic group. The length of the alkyl chain and the nature of the functional groups that may be present in these compounds have effects on both the solution and the final deposited films, in particular on properties like durability and protectiveness [45]. Different metal alkoxides can be used to prepare nanoparticles of different metals or metal oxides. For example, titanium tetraisopropoxide (TTIP) is a common precursor for the synthesis of titanium dioxide nanoparticles, while tetraethylorthosilicate (TEOS) is a common precursor for the synthesis of silica nanoparticles [11, 45];

- Solvent: the solvent, which represents most of the liquid phase of a sol-gel formulation, can affect the solubility of the precursor, the rate of hydrolysis and condensation, and the final size and morphology of the nanoparticles. Common solvents used in sol-gel synthesis include ethanol, methanol, and water. Water is often used as a co-solvent to increase the hydrolysis rate of the precursor, while ethanol or methanol can be used to control the rate of condensation and prevent agglomeration of the nanoparticles. Moreover, the volatility of this component is also an important aspect since it can affect the final deposited products. In particular, high evaporation rates are traduced in cracked films and they also influence the particles distribution density [45, 46];

- pH: the pH of the sol-gel can influence the hydrolysis and condensation reactions that occur during the process. In general, the pH can affect the size, morphology, and properties of the final nanoparticles or thin films [45]. For what concerns the former reaction, it has been demonstrated that it is typically acid-catalyzed and at low pH values (acidic conditions), the hydrolysis is faster, as the protons in the acidic solution can facilitate the cleavage of metal-alkoxide bonds. The pH of the solution can also affect the rate and extent of condensation, as it can influence the availability of hydroxyl groups and the stability of the metal complexes [11, 45]. About the effect on particle size and morphology it has been reported, in the example of TiO_2 nanoparticles, that increasing the pH can lead to larger particle sizes, as the hydroxyl ions in the basic solution can inhibit the growth of small particles. Conversely, decreasing the pH can result in smaller particles [47, 48];

- Temperature: the temperature at which the sol-gel synthesis is carried out can influence the hydrolysis and condensation rates, as well as the crystal structure and morphology of the resulting nanoparticles. Higher temperatures generally result in faster hydrolysis and

condensation rates, which can lead to larger particles with more crystalline structures. However, high temperatures can also cause the nanoparticles to agglomerate or can lead to strongly gelled solutions [32, 45, 49];

- Order of addition of the reagents: the order of addition of the reagents can play a significant role in determining the properties of the resulting sol-gels. The two main methods of adding reagents in sol-gel synthesis are normal addition and reverse addition. The former involves adding the precursor to the solvent (water or other hydrolyzing agent). This method typically results in a relatively rapid hydrolysis and condensation of metal alkoxides, leading to a relatively homogeneous sol-gel solution. However, because the hydrolysis and condensation reactions occur simultaneously, it can be difficult to control the size and distribution of the resulting nanoparticles. In contrast, reverse addition involves adding the water or other hydrolyzing agent to the precursor. This method typically results in a slower, more controlled hydrolysis and condensation of the precursor, allowing for better control over the size and distribution of the resulting nanoparticles. Moreover, the order of addition can also affect the properties of the resulting deposited thin films. In particular, it can affect their homogeneity, as well as the crystal structure and orientation of the nanoparticles within the films [50, 51].

1.6. Surfactants

Surfactants are a class of organic compounds that display amphiphilic behavior. This unique property is attributed to the presence of both hydrophilic and hydrophobic components, commonly referred to as the "polar head" and "non-polar tail", respectively (Figure 1.12(a)). Upon dissolution of surfactants in solvents, the hydrophobic portion perturbs the solvent structure, resulting in an increase in the system's free energy. Consequently, the surfactant spontaneously reorients itself to minimize the contact between the solvent and the hydrophobic group, leading to a decrease in the system free energy. In the case of apolar solvents, of course, the opposite situation occurs [11, 52]. Surfactant molecules can also spontaneously organize themselves in specifically-shaped structures called micelles, which can be spherical, cylindrical or sheet-like (Figure 1.12(b)). In the more common case of spherical micelles in a polar solvent, the molecular structure exposes the hydrophilic heads towards the solvent and the hydrophobic groups towards the inner part [11].

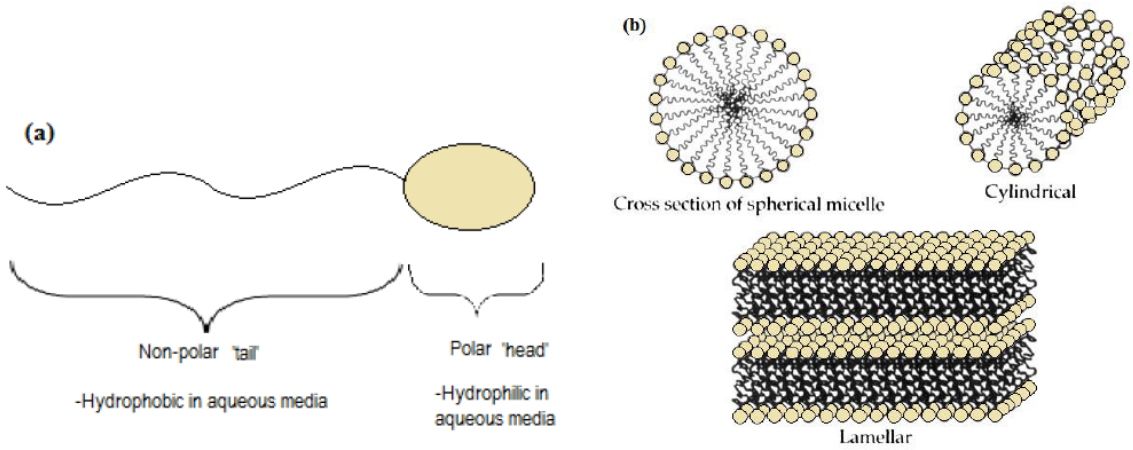

Figure 1.12: (a) General representation of a surfactant molecule; (b) micellar structures formed from the self-organization of the surfactant molecules [11].

The classification of surfactants is based on their chemical nature, which divides them into two main categories: ionic and non-ionic.

1.6.1. Ionic surfactants

Ionic surfactants are compounds that contain a charged hydrophilic group, also known as the head group, and a hydrophobic tail. These surfactants can be further classified into four types: anionic, cationic, zwitterionic, and amphoteric [11, 52].

- Anionic: these surfactants have a negatively charged head group, which makes them soluble in water. The most common types of anionic surfactants are alkyl sulfates (like sodium dodecyl sulfate), alkylbenzene sulfonates, and alkyl ether sulfates [53];
- Cationic: cationic surfactants have a positively charged head group, which makes them also soluble in water. These surfactants are commonly used as antimicrobial agents and fabric softeners. Examples of cationic surfactants include alkyl trimethylammonium salts and alkyl pyridinium salts [53];
- Zwitterionic: these surfactants have both a positive and negative charge. They are used in personal care products such as shampoos, conditioners, and shower gels. Betaine, sulfobetaine, and amine oxide are common examples of zwitterionic surfactants [53];
- Amphoteric: they have both positive and negative charges on their hydrophilic head groups, but their charge varies with pH. These surfactants are widely used in the production of personal care products such as facial cleansers, body washes, and hair condi-

tioners. Examples of amphoteric surfactants include cocamidopropyl betaine and lauryl betaine [53].

1.6.2. Non-ionic surfactants

Non-ionic surfactants do not have a charged head group, but they have a polar group such as hydroxyl, ether, or amide, and a hydrophobic tail. Moreover, they do not bear any sulphur or nitrogen group. The most common categories of non-ionic surfactants are: variations of polyethylene ethoxylates, such as polyethylene glycol (PEG), and alkyl polyglucosides (APGs) (Figure 1.13) [11, 53].

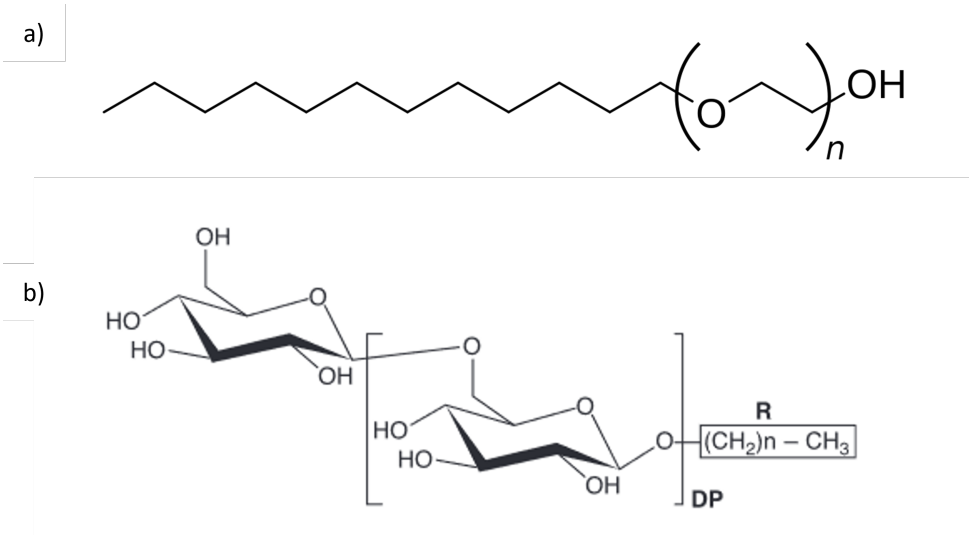

Figure 1.13: Typical structures of common non-ionic surfactants: a) polyethylene ethoxylate, b) alkyl polyglucoside. (R=alkyl chain, DP=degree of polymerization) [11, 54].

1.6.3. Surfactants application in sol-gel chemistry

Surfactants are widely used in the preparation of sol-gel formulations due to their ability to act as spacers for the synthesized particles, leading towards more homogeneous solutions. In general, surfactants are added to the sol-gel formulation to control the particle size, morphology, and stability of the resulting nanoparticles [55, 56]. As seen in previous sections, surfactants can act both as peptizing and templating agents. In the former case, they can adsorb onto the surface of the growing nanoparticles, forming a protective layer that prevents aggregation and stabilizes them. The surfactant layer can also control the growth and morphology of the nanoparticles by selectively binding to certain facets and influencing the direction of crystal growth. In addition, surfactants can influence the surface charge and surface area of the nanoparticles, which can in turn affect their reactivity, adsorption, and dispersibility. They can also act as pore-directing

agents due to their amphiphilic nature and ability to form micellar structures [11]. The latter are exploited to either create templates for the production of highly porous materials with controlled pore size or to better control the hydrolysis and condensation reactions due to the fact that water is less available inside the micellar structures [11, 57]. Ionic surfactants have been shown to be less effective for the production of porous oxides (especially for thin films applications) due to the electrostatic-induced binding between them and the particles that makes it hard to remove the template with extraction methods or heat treatments [11, 58].

List of commonly used surfactants

In this brief subsection a list of the most important surfactants used in sol-gel chemistry is presented. All the information is collected in Table 1.3.

Table 1.3: List of the most used surfactants in sol-gel formulations.

Surfactant	Chemical structure	Type	Reference
CTAB	cetyltrimethylammonium bromide	cationic	[59]
SDS	sodium dodecyl sulfate	anionic	[59]
PEG	polyethylene glycol	non-ionic	[60]
Tween® 20	polyoxyethylene sorbitan monolaurate	non-ionic	[11]
Triton^{TM} X-100	polyethylene glycol tert-octylphenyl ether	non-ionic	[11]
PVP	polyvinylpyrrolidone	non-ionic	[59]
Brij® 35, 58	polyoxyethylene lauryl ether (di-block copolymer)	non-ionic	[56]
Lutensol® ON70	alkyl polyethylene glycol ether	non-ionic	[61]
P-123	pluronic triblock copolymer	non-ionic	[62]
DTAB	dodecyltrimethylammonium bromide	cationic	[63]

1.7. Nanocellulose

In this section, nanostructured cellulose alongside its applications in sol-gel technology will be discussed. Prior to that, a brief introduction on cellulose and, in particular, its crystalline form will be presented.

1.7.1. Cellulose

Cellulose is a biopolymer that is found in plant cell walls and is one of the most abundant and renewable resources on the planet. It is a complex carbohydrate that is composed of repeating units of glucose molecules linked together in a linear chain. Cellulose is a vital material for many industries, including the paper and pulp industry, the textile industry, and the biofuels industry. It is also an important material for engineering applications, including as a reinforcement material in composites [64, 65].

The structure of cellulose is composed of linear chains of glucose molecules linked together by highly directional β-1,4 glucosidic bonds (Figure 1.14) [64, 66]. The glucose molecules are oriented in such a way that they form an elementary micro-fibril structure with strong intermolecular and intramolecular hydrogen bonds between hydroxyl groups and oxygens od adjacent chains and within the same fibril respectively. These fibrils contain both highly ordered (crystalline) regions and disordered (amorphous-like) regions within their structure. The strength of the hydrogen bonds between the glucose chains gives cellulose its high strength and stiffness [64, 65]. Crystalline cellulose is present in several polymorphs (I, II, III, IV), among which cellulose I is the most important since it is the natural occurring structure, present for example in wood, cotton, and plants [64].

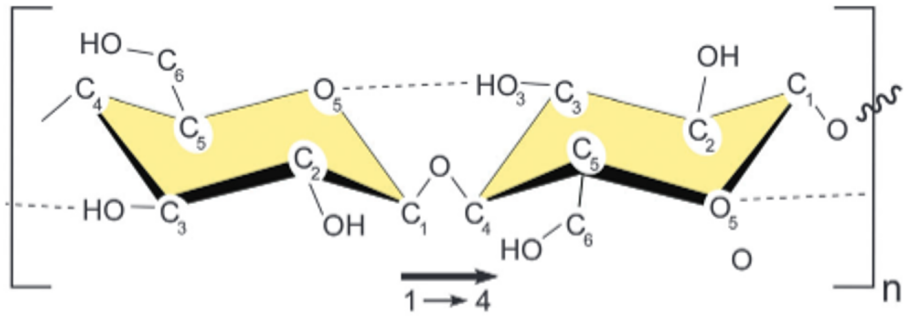

Figure 1.14: Chemical structure of the cellulose repeating unit; in the picture the directionality of the β-1,4 glucosidic bond and the intramolecular hydrogen bonds (dashed line) are highlighted [64].

1.7.2. Nanostructured cellulose production methods and properties

Crystalline cellulose can be extracted from several sources such as wood, plants, algae, tunicates or biomasses from agricultural waste through chemical treatments that separate it from

other molecules such as lignin and hemicelluloses [67]. Nanocellulose can then be produced using mechanical methods, like high-pressure homogenization, or chemical treatments, like strong-acid mediated hydrolysis [68]. Mechanical destruction procedures often require pre-treatments to reduce the required energy for the cellulose defibrillation; TEMPO-oxidation (2,2,6,6-tetramethylpiperidine-1-oxyl) process is a noteworthy treatment that can be used to directly produce nanocellulose or to modify the cellulose functionality, thus reducing the amount of energy needed to produce the nanocellulose via mechanical methods [64, 69]. Two main nano-sized structures are obtainable through the aforementioned processes: cellulose nanofibrils (CNF), which show a higher aspect ratio and greater flexibility, and cellulose nanocrystals (CNC), which possess a lower aspect ratio and a higher degree of crystallinity. CNFs are mainly produced through mechanical disintegration while CNCs are obtained via acid hydrolysis [69]. The former show more amorphous regions with respect to the latter, in which the chemical treatment causes the amorphous parts of the cellulose molecule to be attacked first and then destroyed, leading to a more crystalline material at the end [70, 71]. Atomic force microscopy images of these two types of nanocellulose are illustrated in Figure 1.15.

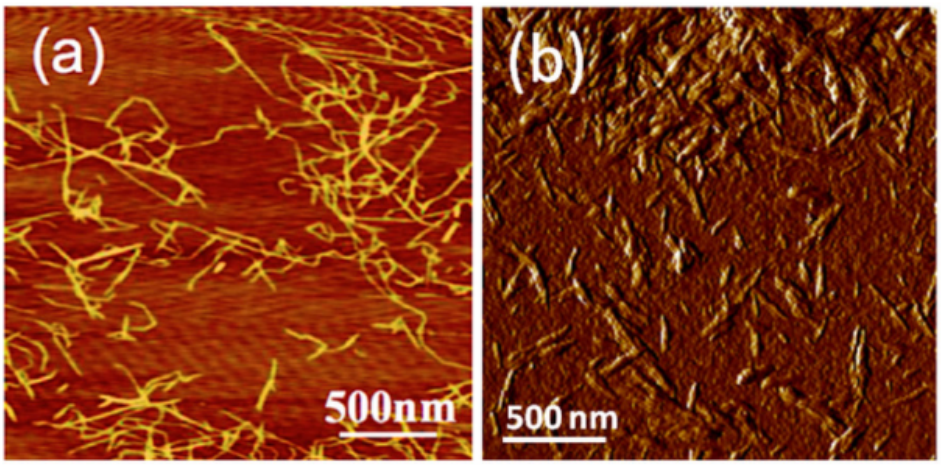

Figure 1.15: AFM images of (a) cellulose nanofibrils (CNF) and (b) cellulose nanocrystals (CNC) [69, 72, 73].

1.7.3. Acid hydrolysis

As previously mentioned, acid hydrolysis is a chemical treatment employed in the production of nanocellulose, in particular CNCs. This method involves the usage of a strong acid to remove (hydrolyze) the amorphous part of the cellulose sources. Sulfuric acid is typically used since it confers a negative surface charge to the particles, creating a more stable suspension at the end of the synthesis. Even at the nano-scale cellulose is not soluble in water, so it is important to

maximize the dispersibility to obtain homogenous suspensions [64]. The acid hydrolysis route typically consists in the following steps:

1. cellulose is added to a solution of sulfuric acid and the reaction goes on for a given amount of time;
2. the reaction is quenched through the dilution with water;
3. the resulting mixture goes through a series of centrifugation and washing/rinsing steps to remove the majority of the acidity;
4. a dialysis is performed to extract the last contents of acid;
5. the final dispersion can be subjected to an ultra-sonication step to produce a stable and homogeneous suspension [64, 74].

1.7.4. Nanocellulose in sol-gel technology

Nanocellulose can be added to sol-gel formulation with the primary aim of creating controlled porosity for the synthesis of highly mesoporous metal oxides, acting so as a templating agent [75]. Having homogeneous and controlled voids in the final product is favorable to maximize the surface area, thus enhancing several properties such as the photocatalytic activity in the case of TiO_2 thin films [76]. Nanocellulose offers many advantages as a templating agent: CNCs are rigid and thermally stable, allowing for a good formation of the oxide crystalline phase during calcination without the risk of the collapsing of the template and the subsequent decrease in surface area; moreover, it is a widely available and sustainable material, making it an interesting alternative to other synthetic templates [43, 75]. While the main advantage is nanocellulose having the combined benefits of soft- and hard-templating agents, it can be exploited also for creating nanocomposites through the sol-gel method. This is possible and favored by the presence of oxygenated functional groups that promote the nucleation and growth of metal oxide nanoparticles. For example, titanium dioxide particles can easily anchor themselves to the hydroxyl groups of the CNCs and then grow, ultimately forming the NC-TiO_2 nanocomposite [43]. This material has been reported to show higher photocatalytic properties, as well as enhanced mechanical stability.

Overall, nanocellulose covers an important role in sol-gel technology, in fact, in this work it has been deeply investigated.

1.8. Deposition techniques

The high versatility of the sol-gel method stands also in the wide variety of deposition techniques available to obtain thin films of oxide nanoparticles. Among those, the most commonly used ones are: dip-coating, spin-coating, spray coating (or spray pyrolysis) and electrophoretic deposition (EPD) [77]. Between these techniques, dip-coating is the one offering the best advantages in terms of cost and versatility and since it was extensively used in the experimental part of this thesis, it will be discussed in details in the following. The other deposition methods were not employed in this work, hence they will just be visually reported in Figure 1.16.

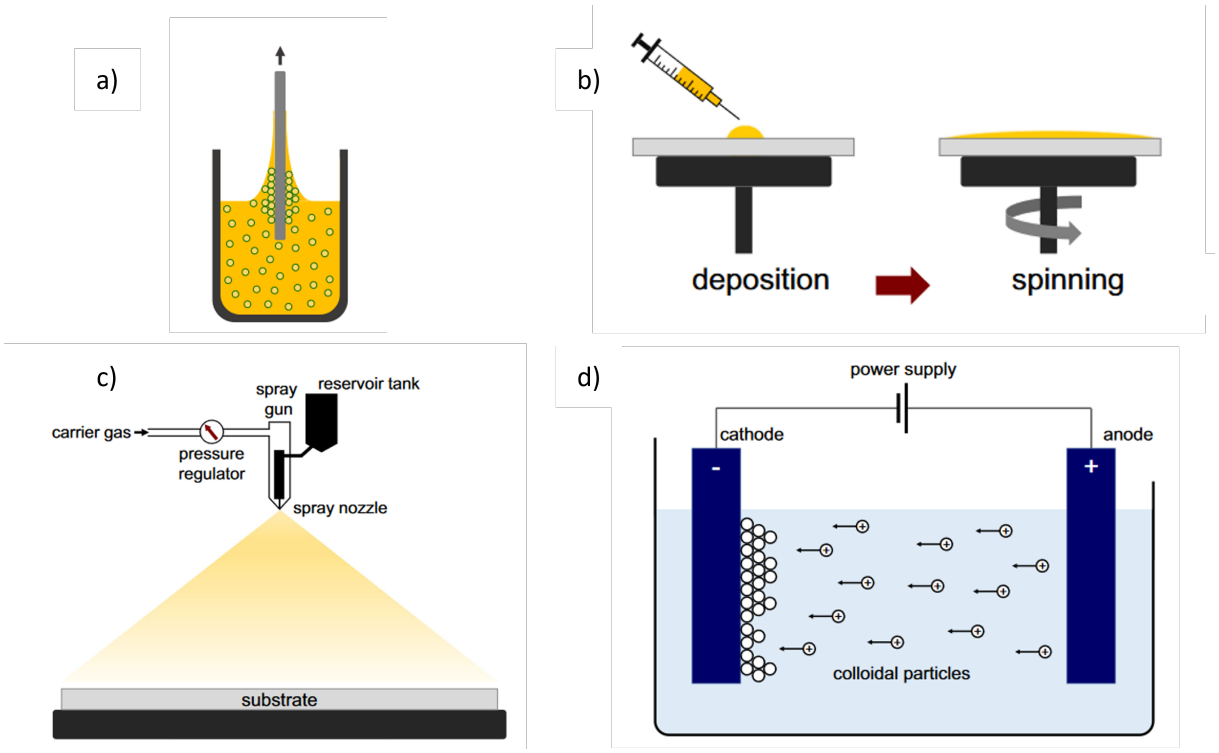

Figure 1.16: Schematic illustration of the most commonly used techniques to obtain thin films from sol-gel solutions: a) dip-coating, b) spin-coating, c) spray coating, d) electrophoretic deposition. (Adapted from [77]).

1.8.1. Dip-coating

Dip-coating is the most used wet-chemical technique to generate thin metal oxide films. It is advantageous with respect to spin-coating since it does not require any specialized equipment. To apply this technique, a substrate is immersed into a sol-gel solution containing the chemical precursor and then extracted at a controlled rate. The thin film thickness is determined by the forces acting at the liquid surface stagnation point. When the substrate is withdrawn at a quicker

pace, more fluid is brought up to the surface before it can return to the solution, causing thicker films to form [11]. The stages of the dip-coating process are summarized in Figure 1.17.

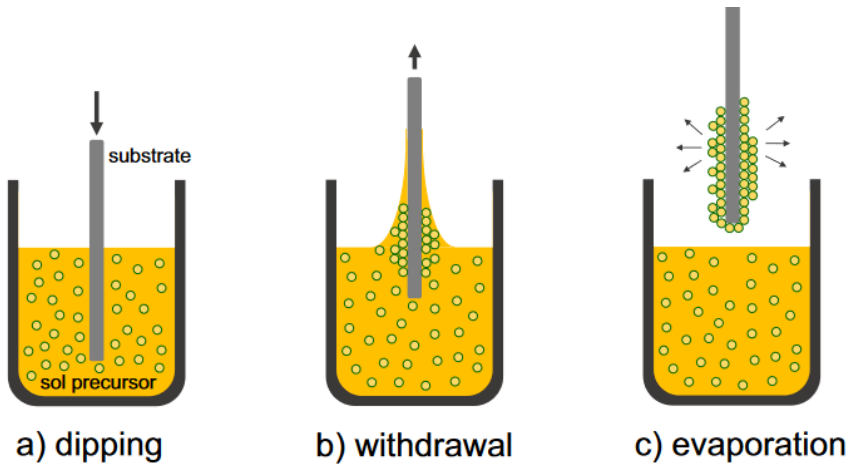

Figure 1.17: Schematic illustration of the dip-coating process highlighting the main stages: a) dipping of the substrate, b) withdrawal of the substrate, c) draining and evaporation of the solvent [77].

An advantage of dip coating is that it permits the application of a thin film on both sides of the substrate, which enhances the coating effectiveness and reduces the number of necessary dips. This technique is commonly used to generate oxide thin film coatings over large areas, such as on bulk glass. A single coating can produce thin films up to 1μm, and additional layers can be added later on. Since sol-gel derived precipitates are frequently amorphous, they must be further heat-treated to promote crystallization.

As previously mentioned, the thickness of the coating can be controlled through the speed of the dipping and withdrawal steps; moreover, the viscosity, density, and surface tension of the solution have an impact on the thickness of the resulting film [11]. This parameter can in general be predicted with the Landau-Levich equation (Equation (1.14)) if the withdrawal speed is such that the shear rates acting on the system maintain a Newtonian regime of flow [78].

$$h = 0.94 \frac{(\eta \cdot v)^{2/3}}{\gamma_{LV}^{1/6}(\rho \cdot g)^{1/2}} \tag{1.14}$$

Where h=thickness, η=viscosity, v=withdrawal velocity, γ_{LV}=liquid-vapor surface tension, ρ=density, and g=gravity constant.

Other notable advantages in using the dip-coating technique are the low cost, the simple operative requirements, the feasibility at room temperature, the fact that vacuum is not required, and the possibility to homogeneously coat complex-shaped substrates [77].

1.8.2. Calcination thermal treatment

After deposition, the metal oxide nanoparticles require a thermal treatment to be consolidated onto the substrate. A calcination treatment is usually performed by heating the coated samples at temperatures of 100°C to even 500°C, depending on the type of sol, substrate, and application envisioned. This step has different and subsequent effects on the treated material:

1. evaporation of residual solvent at T < 200°C and consolidation of the film framework accompanied by an uniaxial shrinkage along the normal direction;
2. pyrolysis of the eventually present template at T=250-300°C causing an increment in porosity;
3. nucleation and growth of the crystalline phase at T > 300°C [23].

Calcination temperature is the fundamental parameter to control in order to avoid the collapse of the mesoporous structure, indeed, it should be below the thermal stability value for the deposited thin film [23]. Moreover, this heat treatment is fundamental in the case of titanium dioxide nanoparticles synthesized through the sol-gel method since the development of the anatase crystalline phase is achievable through annealing only. In particular, for TiO_2 the calcination temperature should be kept at around 500°C since high temperatures may lead to undesired results such as phase transition to rutile structure (at T>700°) or excessive particle aggregation via the mechanism of diffusive sintering, which leads to a decrease in surface area [23, 79–81]. These effects are reflected in a change in the properties of the material, such as photocatalytic activity or optical properties [82].

1.9. Noteworthy TiO_2 sol-gel formulations

In this brief section, a table containing some already tested formulations for the sol-gel synthesis of TiO_2 is presented below (Table 1.4). All these formulations were found analyzing recent literature works. Most of them dealt with organic colorants and obtained positive results from the UV photocatalytic degradation tests. Different parameters were also investigated among different works, for example, Arconada et al. researched the relationship between the TiO_2 deposited film thickness and the photocatalytic degradation of methyl orange; while Cernigoj et al. focussed on finding the optimal amount of dip-coated layers to obtain a sufficient photoactive material for the degradation of Plasmocorinth B, an azo dye compound.

Most of these works focussed on the correlation between the amount of surfactant or templating agent and the photocatalytic properties shown by the final deposited products. Promising results were obtained, for example, in the study of Toro et al., where a sol-gel synthesized TiO_2-

nanocellulose nanocomposite coating was able to almost completely degrade the methyl orange test solution in just 3 hours.

Eventhough different works followed different procedures and tests, it was possible to highlight several benefits given by the addition of surfactants or nanocellulose to the formulation of titanium dioxide sol-gels for photocatalytic applications, hence supporting the aim of this current work.

Table 1.4: Formulations for the sol-gel synthesis of photocatalytic TiO_2 found from literature review. (TBT = titanium(IV) butoxide, DEA = diethanolamine, DCIP = 2,6-dichloroindophenol, TEOT = titanium ethoxide).

	Precursor		Solvent		Chelating Agent		Surfactant/Templating agent		Tested with	Reference
	Name	Qt.	Name	Qt.	Name	Qt.	Name	Qt.		
1.	TTIP	1 molar	Ethanol	40 molar	Acetic Acid	1 molar	SDS	0.05 molar	Methyl orange	[83]
			Distilled water	2 molar						
2.	TTIP	1 molar	Ethanol	40 molar	Acetic Acid	1 molar	Brij 58	0.07 molar	Methyl orange	[83]
			Distilled water	2 molar						
3.	TTIP	1 molar	Ethanol	40 molar	Acetyl-acetone	1 molar	F127	0.5 mmolar	Methyl orange	[83]
			Distilled water	2 molar						
4.	TTIP	1 molar	Isopropanol	45 molar	Acetic Acid	6 molar	Tween 20	0.5 - 3.0 molar	Methylene blue	[58]
5.	TTIP	1 molar	Isopropanol	45 molar	Acetic Acid	6 molar	Triton X-100	0.5 - 3.0 molar	Methylene blue	[58]
6.	TTIP	1 molar	2-methoxyethanol	0.075 molar	Acetic Acid	1 molar	Triton X-100	15 wt.%	Plasmocorinth B (azo dye)	[84]
7.	TTIP	30 mL	Bi-distilled water	50 mL	HCl	1.86 mL	P123	3 g	Methyl orange	[62]
8.	TBT	10 mL	Ethanol	35 mL	DEA	1 molar vs TBT	CTAB	-	-	[85]
9.	TTIP	8 mL	Ethanol	23.2 mL	HNO_3	0.2 mL	-	-	DCIP	[86]
			Ethyl acetylacetate	2.75 mL						
10.	TEOT	14.4 mL	Butan-1-ol	56 mL	HCl	10.2 mL	P123	5 g	DCIP	[86]
11.	TTIP	28.13 g	Ethanol	260.7 mL	HCl	1 mL (11 mmol)	Lutensol ON70	0.47 g	Siloxane	[61]
12.	TBT	-	Distilled water	100 mL	Acetic Acid	1:2 vol. vs TBT	CNC	-	Methyl orange	[43]

2 | Materials and methods

2.1. Raw materials

The main goal of this work was to synthesize photocatalytic TiO_2 through the sol-gel technique by modifying the formulations with different templates and surfactants, in order to achieve high photoactivity in smaller time windows compared to previous works. The used reagents were also carefully selected in order to eliminate or reduce as much as possible the employment of toxic and harmful substances. Water purification was the goal application for the synthesized and deposited material, hence, it was inherently challenging to achieve good results while limiting the usage of reagents such as acetylacetonate or dimethylacetamide. In Table 2.1 the reagents employed for the preparation of sol-gels are summarized. They will be presented more in detail in the next sections.

Table 2.1: List of reagents used in sol-gel formulations. (Abv. = abbreviated).

Type	Reagent	Abv. name	Purchaased from
Precursor	Titanium(IV) isopropoxide 97%	TTIP	Sigma Aldrich
Solvent	Water	H_2O	-
	Isopropanol	*i*-PrOH	Sigma Aldrich
	Ethanol	EtOH	Sigma Aldrich
Chelating agent	Glacial acetic acid 99.5%	AA	Sigma Aldrich
Catalyst	Hydrochloric acid 37%	HCl	Sigma Aldrich
Surfactant	Sodium dodecyl sulfate	SDS	Sigma Aldrich
	Lutensol ON70	LUT70	BASF
	Ecosurf eh-3	ECH3	Sigma Aldrich
Templating agent	Cellulose nanofibers (3% solids slurry)	CNF	Maine University

Alongside with the sol-gel synthesis also the production of cellulose nanocrystals was performed, in order to compare their templating effect to the commercially available nanocellulose products. The route of acid hydrolysis was chosen due to the ease of execution, the quality of the final product and the flexibility of the cellulose sources, which in principle could be derived

from industrial waste. In this work, the reagents used for this reaction were: commercially available cotton, distilled water and sulfuric acid 96% purchased from Sigma Aldrich.

2.1.1. Precursor

Titanium(IV) isopropoxide (TTIP)

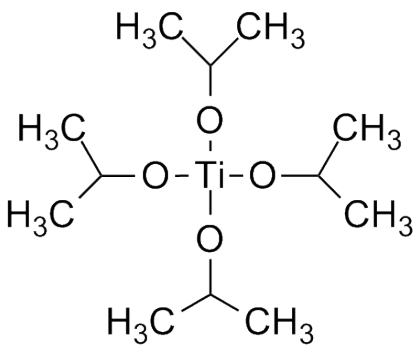

Figure 2.1: TTIP molecular structure.

TTIP (Figure 2.1) is the most commonly used metal alkoxide precursor for the production of nanostructured TiO_2 due to its high reactivity with water and other OH-bearing molecules. TTIP has also been proven to be the better metal alkoxide precursors like titanium butoxide or titanium ethoxide, as stated in previous works [87]. TTIP properties are summarized in Table 2.2.

Table 2.2: TTIP properties.

Property	
Chemical formula	$C_{12}H_{28}O_4Ti$
Molecular weight	284.22 g/mol
Appearance	Colorless to light-yellow liquid
Density at 20°C	0.96 g/cm^3
Melting point	17°C
Boiling point	232°C
Hazards	Flammable liquid and vapour, eye irritant

2.1.2. Solvents

Water

Water is the cleanest and safest solvent for the production of TiO_2 thin films via the sol-gel method. The hydrolysis reaction readily starts when H_2O and the precursor come in contact. The ratio between the two reagents is a key factor to control the reaction rate and so the stability of the sol itself. Lower amounts of water can cause quick gelation of the system. Sol-gels synthesized with water usually show higher photoactivity of the final product, however, the deposited thin films have poor aesthetical appearence.

Isopropanol

Isopropanol is an organic solvent used in the non-aqueous preparation of sol-gels. Its main advantages are that it is non-toxic and has high precursor solubility. Moreover, it shows a controlled rate of hydrolysis reaction, leading to more controlled nanoparticles formation. Its high volatility allows also for faster drying and for the formation of porous deposited films, in principle enhancing their surface area. The main drawbacks are, the cost, which is higher than more commonly available solvents, and the fact that it does not come from renewable sources.

Ethanol

Ethanol is an organic solvent that can be derived from the fermentation of renewable sources such as sugar and yeast. This aspect alongside its non-toxicity make it interesting for a green sol-gel synthesis. Ethanol shows also high solubility towards TTIP and allows for stable sols. It also shows good wettability in the final deposited thin films, leading to homogeneous surfaces, good from an aesthetic point of view. The main disadvantage is that the photocatalytic activity of the produced films tends to be lower than the one of water-based sol-gels.

Chelating agent

Glacial acetic acid

Glacial acetic acid is the second simplest carboxylic acid and it is commonly used in sol-gel technology for its peptizing effect. There are several advantages in using this reagent among other chelating agents. Indeed, it is highly reactive towards alkoxide precursors, it is relatively inexpensive and, in principle, can be produced from renewable sources, such as biomass or waste streams from the wood pulp and paper industries. Even though it is non-toxic, it still is a corrosive substance and must be handled with care. Overall, it is a quite green choice for the preparation of sol-gels, matching the aim of this work.

2.1.3. Catalyst

Hydrochloric acid (37%)

Hydrochloric acid is employed as a catalyst for the hydrolysis reaction in sol-gel technology. Due to its high acidity, it is added in very small quantities, as otherwise it would modify the pH to levels which may cause unstable gelation. It is a toxic reagent and must be handled with care due to its high corrosivity. In this work it was used in a small amount (11 mmol) just for the preparation of a sol-gel described in literature for comparison purposes [61].

2.1.4. Surfactants

Sodium dodecyl sulfate (SDS)

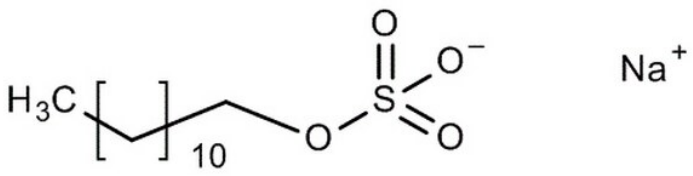

Figure 2.2: Sodium dodecyl sulfate molecular structure.

Sodium dodecyl sulfate is an anionic surfactant commonly employed in sol-gel formulations to improve the dispersibility of the precursor. SDS is soluble both in water and organic solvents, but to a lesser extent in the latter. Its ionic nature makes it difficult to control the stability of the produced nanoparticles and can even cause them to precipitate if present in too high quantities. It is overall a promising reagent but has many downsides concerning the toxicity. Its usage should be limited due to these reason and in this work it was employed in few formulations to have a comparison between ionic and non-ionic surfactants. SDS properties are summarized in Table 2.3.

Table 2.3: Sodium dodecyl sulfate properties.

Property	
Chemical formula	$C_{12}H_{25}NaO_4S$
Molecular weight	288.38 g/mol
Appearance	White fine flakes
Hazards	Flammable solid, skin and eye irritant, toxic if inhaled or ingested, toxic for aquatic organisms

Lutensol® ON70

Lutensol® ON70 is a non-ionic surfactant belonging to the group of alkyl polyethylene glycol ethers made from a saturated, synthetic, short-chain fatty alcohol. Its role in the sol-gel formulation is to enhance the stability of the sol by establishing better homogeneity in the system. Moreover, non-ionic surfactants are widely employed for their pore-forming capabilities in the final deposited thin films. Lutensol® ON70 is a high purity reagent with the advantage of being also relatively inexpensive. Its main properties are summarized in Table 2.4.

Table 2.4: Lutensol® ON70 properties. (R=saturated, synthetic, short-chain fatty alcohol).

Property	
Chemical formula	$RO(CH_2CH_2O)_7H$
Molecular weight	approx. 470 g/mol
Appearance	Cloudy colorless liquid
Hazards	Eye irritant

Ecosurf eh-3

Ecosurf eh-3 is a non-ionic surfactant belonging to the group of alcohol ethoxylates. The main benefits that it brings to sol-gel formulations are connected to its non-ionic nature, as for the previous surfactant. It is also highly soluble in water and all polar organic solvents. This reagent is more promising than other similar surfactants from the sustainability point of view. It is, in fact, readily bio-degradable and shows low to none aquatic toxicity, based on the concentration. Ecosurf eh-3 main properties are summarized in Table 2.5.

Table 2.5: Ecosurf eh-3 properties.

Property	
Chemical formula	$C_8H_{18}O \cdot (C_3H_6O)_x \cdot (C_2H_4O)_y$
Molecular weight	Unknown to public
Appearance	Pale yellow liquid
Density at 20°C	0.976 g/cm^3
Critical micelle concentration at 25°C	480 ppm
Hazards	Eye irritant

Since the molecular weight of this product is not available as a public information, the amount used in the sol-gels prepared in this work was based on the critical micelle concentration.

2.1.5. Templating agent

Cellulose nanofibers (CNF)

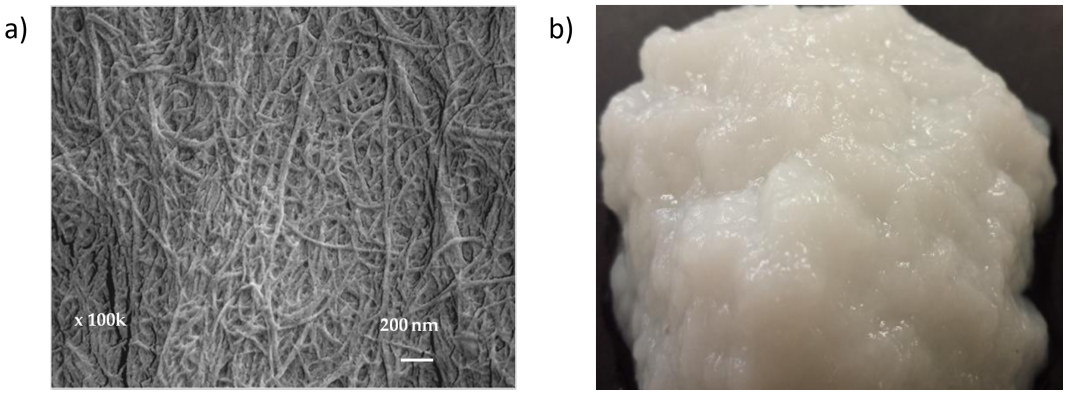

Figure 2.3: a) SEM image of Maine University cellulose nanofibers; b) 3% CNF slurry appearance [88].

Cellulose nanofibers purchased from Maine University were chosen as one of the templating agents employed in the sol-gel preparation (Figure 2.3). As seen in section 1.7.4 the addition of this material can lead to various benefits for the final synthesized product. Moreover, cellulosic materials are sustainable and non-toxic. The CNC used in this work was in the form of a 3 wt% aqueous gel which is a cheap but high quality product that due to its hydrophilic nature allows for homogeneous dispersion in water. The main properties of this material are reported in Table 2.6.

Table 2.6: 3% CNF slurry properties [88].

Property	
Appearance	White wet solid
Density at 20°C	1.0 g/cm^3
Fiber dimensions	Nominal diameter of 50 nm Length of 100s of μm
Hazards	-

2.1.6. Materials for nanocellulose synthesis

Sulfuric acid (96%)

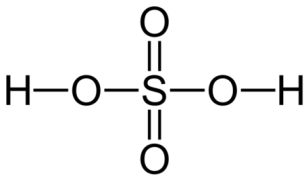

Figure 2.4: Sulfuric acid molecular structure.

Sulfuric acid is the most commonly used strong acid to produce cellulose nanocrystals via the acid hydrolysis method. This reagent is very reactive towards the breaking of the glucosidic bonds and then consequent removal of the amorphous part of the cellulose macromolecule. The overall effect is the size reduction of the fibers which reaches the nanometer scale. Even if sulfuric acid is not a harmless reagent, its usage is quite essential to reach good results in shorter times. The concentration of the acid is the parameter which mostly affects the reaction, alongside the reaction temperature. Highly concentrated sulfuric acid leads to fast and uncontrolled hydrolysis reactions causing degradation to the cellulose fibers and producing undesired by-products. The concentration strongly influences the rate of hydrolysis, hence, the final nanocellulose size. For the previously mentioned reasons, in this work, sulfuric acid 96% was diluted to a concentration of 64% which was high enough to allow for a fast reaction time without causing strong increments in the temperature and eventually leading to a pure, non-degraded nanocrystalline cellulose product. In Table 2.7 the main properties of sulfuric acid are reported.

Table 2.7: Sulfuric acid properties.

Property	
Chemical formula	H_2SO_4
Molecular weight	98.08 g/mol
Appearance	Colorless oily liquid
Density at 20°C	1.84 g/cm^3
Melting point	10°C
Boiling point	337°C
Hazards	Corrosive to skin, corrosive to metals, eye irritant

2.2. Acid hydrolysis for nanocellulose synthesis

For the acid hydrolysis method, sulfuric acid was employed as the acid catalyst. In the following, all the steps and the amounts of reagents used will be listed.

1. 83 mL of sulfuric acid 64% were prepared by diluting the starting reagent which was at a concentration of 96%;
2. 1.5 g of commercially available cotton (100% cellulose) were slowly ground using a coffee grinder, to avoid heating up the fibers;
3. the diluted sulfuric acid was added to a round-bottomed flask and heated to the temperature of 45°C using a heating plate equipped with a thermostatic oil bath. The solution was also put under magnetic stirring at 500 rpm;
4. the ground cotton was added slowly to the acid. The cotton immediately dissolved upon touching the solution and the ongoing reaction was quite exothermic. Due to this fact, the round-bottomed flask was carefully handled to avoid exceeding the temperature of 45°C;
5. the reaction was kept under stirring for 2 hours till the color of the suspension changed to a yellowish tone. In this step, the reaction time and the acid concentration are crucial and if they exceed certain levels they may lead to the burning and decomposition of the cellulose, resulting in a dark brown color of the suspension;
6. the reaction was stopped and the acidic suspension was quickly quenched with 450 mL of cold Milli-Q distilled water (at 10°C);
7. the suspension was left overnight in the fridge to allow the separation between the deposit

and the supernatant;

8. most of the supernatant was initially removed with a pipette, paying attention not to remove the nanocellulose;
9. the remaining suspension was subjected to a centrifuge cycle: it was split in several flasks and put inside the centrifuge for 15 minutes at 4000 rpm. This step was performed to further remove the supernatant which was, indeed, separated from the solid deposit;
10. a series of 4 washing steps were performed again using the centrifuge: the previously obtained deposit was collected in few flasks and diluted with Milli-Q distilled water before subjecting it to a 15 minutes centrifuge cycle at 4000 rpm. The transparent supernatant was then removed and the step was repeated 3 more times. This procedure was performed to reduce the level of acidity of the nanocellulose suspension. It was stopped after the 4th centrifuge since the supernatant was becoming more opaque, indicating the presence of dispersed nanocellulose;
11. the remaining suspension was collected in a beaker and neutralized using a 0.1 M solution of NaOH, prepared with the solid salt purchased from Sigma Aldrich. The neutralization was not stoichiometric but was precisely monitored using a pH-meter, till the value read on the instrument was close to 7.00;
12. the precipitate salt ($NaSO_4$) was removed through a filtration step using a vacuum pump to better recover the suspension containing the nano-sized cellulose.

The final product was then stored in glass vials and tested with the Dynamic Light Scattering technique to check the size of the suspended nanocrystals. This technique will be discussed later in this chapter and the results concerning the produced nanocellulose will be presented further in this work.

2.3. Sol-gel nomenclature

In this brief section, the nomenclature used for the prepared sol-gel formulations will be explained. In Figure 2.5 the general scheme is represented.

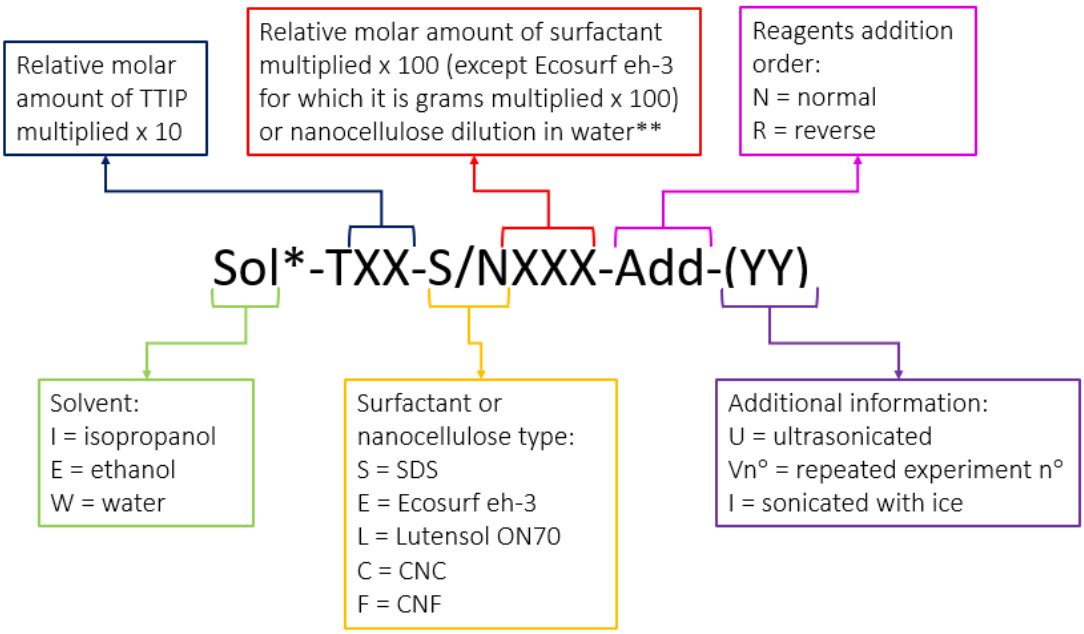

Figure 2.5: General code for the prepared sol-gel formulations denomination.

*In the case of three specific formulations, where the water solvent was used in a different relative molar amount, this amount was reported in the code right after the letter "W". In all the other cases, the relative molar amount o solvent was not different in between formulations, for this reason, the number that indicates it is now present in the code.

**The value present in the code refers to the water dilution in weight, such as 1:x, where x is the mass of water and 1 represents the weight of the 3% slurry, in the case of CNF, or the solid part present in the suspension. in the case of CNC. The latter refers to the weight of CNC plus the residual amount of $NaSO_4$. To make the code more readable, dilutions bigger than 1:1000 are shortened to just 1 digit. In particular, in this work there are two cases where this happens: dilutions 1:6699 and 1:3364, which become C6 and C3, respectively, in the coded name.

I-T12-L20-N and W-T10-F200-R are two examples to better understand the coded nomenclature.

2.4. Sol-gel synthesis

The main scope of this work was to optimize the synthesis step of the titanium dioxide sol-gels. Different formulations and addition methods have been used and will be reported in the

following. Overall, a total of 45 formulations have been prepared. In Table 2.8, just few of them are reported, being the ones that led to the best results or the ones exploiting novel reagents, like nanocellulose. In Appendix A all the prepared sol-gels are reported in detail.

Table 2.8: Some of the prepared sol-gel formulations.

Sol-gel	TTIP [g]	Solvent [g]	Chelating agent [g]	Surfactant/Templating agent [g]	Molar ratio
I-T12-L20-N	6.82	54.09 *i*-PrOH	6.00 AA	1.88 Lutensol ON70	1.2:45:5:0.2
E-T10-L7-R	5.68	36.86 EtOH	1.20 AA	0.66 Lutensol ON70	1:40:1:0.07
W-T12-F200-R	6.82	35.82 H_2O	6.00 AA	0.18 CNF 3%	1:100:5
W-T12-L20-N	6.82	36.00 H_2O	6.00 AA	1.88 Lutensol ON70	1.2:100:5:0.2
W-T12-E5-N	6.82	36.00 H_2O	6.00 AA	0.05 Ecosurf eh-3	1.2:100:5:x
W-T12-C3-R-I	6.82	34.46 H_2O	6.00 AA	1.54 CNC 0.70%	1:100:5

The two main procedures followed for the sol-gel preparation were the normal addition method and the reverse addition method. They were briefly described in subsection 1.5.5 and will now be presented, explaining their features and focusing on how they were used in this work.

2.4.1. Normal addition method

In the normal addition method, the precursor is added to the solvent. In particular, for the sol-gels prepared with this addition order, the preparation steps were:

- for surfactant-based sol-gels:
    1. the surfactant was firstly added to the solvent in a 100 mL beaker and put under magnetic stirring for 10 minutes to allow its dispersion;
    2. acetic acid was then added dropwise to the mix and stirred for 10 minutes;
    3. TTIP was finally added dropwise to the solution and stirred at max speed for 1 hour. Typically, strong gelation occurred during this step, therefore, when that happened, manual mixing was performed to break the gel;
    4. the sol-gel was sonicated for 15 minutes in the Falc ultrasonic bath (Figure 2.6).

Figure 2.6: Falc ultrasonic bath.

- for nanocellulose-based sol-gels:
    1. the nanocellulose fibers slurry or the crystalline nanocellulose dispersion were diluted to the desired level by adding them to distilled water in a 100 mL beaker. To ensure a good homogeneity, the dispersion was put under magnetic stirring for 10 minutes and further sonicated for 15 minutes;
    2. acetic acid was then added dropwise to the mix and stirred for 10 minutes;
    3. TTIP was finally added dropwise to the solution and stirred at max speed for 1 hour. Typically, strong gelation occurred during this step, therefore, when that happened, manual mixing was performed to break the gel.

In addition to the previously described procedures, there were two surfactant-based sol-gels (E-T10-L7-R, E-T10-S5-R) prepared by adding acetic acid to TTIP first and then putting this mixture dropwise in the solvent solution containing the surfactant. Each intermediate solution was stirred for 10 minutes and the final solution was stirred for 1 hour followed by a 15 minutes sonication.

2.4.2. Reverse addition method

In the reverse addition method, the solvent is added to the precursor. In particular, for the sol-gels prepared with this addition order, the preparation steps were:

- for surfactant-based sol-gels:
    1. the surfactant was firstly added to the solvent in a 100 mL beaker and put under magnetic stirring for 10 minutes to allow its dispersion;

2. acetic acid was then added to TTIP and stirred for 10 minutes;
3. the solvent and surfactant solution was slowly added to the precursor solution and stirred at max speed for 1 hour. Typically, strong gelation occurred during this step, therefore, when that happened, manual mixing was performed to break the gel;
4. the sol-gel was sonicated for 15 minutes in the Falc ultrasonic bath.

- for nanocellulose-based sol-gels:
  1. the nanocellulose fibers slurry or the crystalline nanocellulose dispersion were diluted to the desired level by adding them to distilled water in a 100 mL beaker. To ensure a good homogeneity, the dispersion was put under magnetic stirring for 10 minutes and further sonicated for 15 minutes;
  2. acetic acid was then added to TTIP and stirred for 10 minutes;
  3. the nanocellulose dispersion was slowly added to the precursor solution and stirred at max speed for 1 hour. Typically, strong gelation occurred during this step, therefore, when that happened, manual mixing was performed to break the gel.

The only exceptions to these procedures were the sol-gels "M", "LA12M2", and "LA14M3", which were synthesized following the method reported by Antonello et al. [61]. This consisted in the following steps:

1. ethanol was added to TTIP to form a 0.6 M solution and stirred for 5 minutes;
2. HCl was added to the previous solution and stirred for 5 minutes more;
3. Lutensol ON70 was added to the other portion of ethanol and stirred for 10 minutes;
4. the latter was added to the first solution (0.6 M TTIP in ethanol and HCl) and stirred at medium speed for 1 hour.

2.4.3. Ultrasonication for accelerated condensation

A different preparation approach was followed for two sol-gels, namely "I-T12-L20-N-U" and "E-T10-L7-R-U" (Table 2.9). Indeed, they were prepared following the normal and reverse routes for surfactant-based formulations, respectively, but instead of sonicating the final solutions for 15 minutes, they were put inside the Falc ultrasonic bath for 2 hours. This step was chosen to test the effect of the increased reaction temperature on the sol-gels. The ultrasonic waves produced by the machine, in fact, established a ramping increase in the solutions temperature. This increase was monitored every 20 minutes with a thermometer inserted in each solution and also in the water of the bath itself. Moreover, this 2 hours sonication step was

repeated every week for 4 weeks to compare the effect of the temperature-enhanced ageing to the effect of natural ageing.

Table 2.9: Ultrasonicated sol-gel formulations.

Sol-gel	TTIP [g]	Solvent [g]	Chelating agent [g]	Surfactant [g]	Molar ratio
I-T12-L20-N-U	6.82	54.09 *i*-PrOH	6.00 AA	1.88 Lutensol ON70	1.2:45:5:0.2
E-T10-L7-R-U	5.68	36.86 EtOH	1.20 AA	0.66 Lutensol ON70	1:40:1:0.07

2.5. Deposition method: dip-coating

To deposit the prepared TiO_2 sol-gels onto the glass substrates (size: 2.5 *x* 2.5 *x* 0.3 cm), the dip-coating technique has been adopted. To perform it, a built-in dip coater was used (Figure 2.7a). The glass slide was appropriately held in place by a metallic clamp which was properly attached to the movable part of the instrument to allow its up and down movement. The dip coater was controlled via the program Arduino and the code is reported in Figure 2.7b. The highlighted values are the the pulse speed of the apparatus for the descent and the ascent, expressed in μs. These values are readily convertible to the dip speed in mm/min as reported in Table 2.10.

Figure 2.7: a) Dip coater apparatus, b) Arduino code to control the instrument speed.

Table 2.10: Conversion values between the pulse speed and the dip speed.

Dip speed [mm/min]	Descent pulse speed [μs]	Ascent pulse speed [μs]
120	5040	5280

All the depositions were performed at a dip speed of 120 mm/min and two layers of material were applied to the substrate, waiting 20 minutes in between each deposition to allow the previous layer to dry; the wait time was reduced to 15 minutes for alcohol-based sol-gels since the solvent was more volatile. All these parameters were chosen based on the results obtained in previous works which investigated the optimal deposition conditions [87]. Another 20-30 minutes wait was performed prior to the calcination step to again allow the drying of the sample and avoid the formation of liquid bubbles on the surface, which may pop during the thermal treatment leaving defects on the coating. Each sol-gel was dip-coated onto a glass slide every two weeks after the preparation date for as long as six weeks (eight in few initial cases), to check the sol ageing in the short-term period.

2.6. Thermal treatment: calcination

The last step for the preparation of the sample was the calcination thermal treatment. This was performed by putting the freshly coated samples in a GEFRAN 1200 muffle-type oven (Figure 2.8) at the temperature of 500°C for two hours. This step is crucial to promote the transformation from amorphous to crystalline TiO_2 and ensure a better adhesion to the glass substrate. Every coated sample was subjected to this same thermal treatment because it was found to be optimal in previous works [87].

Figure 2.8: GEFRAN 1200 muffle-type oven.

2.7. Photocatalytic degradation tests

In this section the two routes followed for the photocatalytic tests are presented. They will be labelled as UV-LED photocatalytic degradation test and UV-VIS photocatalytic degradation test. The former was performed as it is a well established method. The latter, instead, was used as a screening procedure since it is faster to perform but is subjected to higher experimental errors.

2.7.1. UV-LED photocatalytic degradation test

UV-LED photocatalytic tests were carried out in a rhodamine B (RhB) 10^{-5} M aqueous solution. The reaction was conducted in a lab-scale reactor. This consisted in a 100 mL beaker containing 40 mL of the aforementioned RhB solution. The dip-coated samples were put inside the reactor and held suspended by a titanium net that kept the sample at a fixed distance of 3.5 cm from the top of the beaker. An UV light emitting LED was put on top of the system to close the beaker and assure a perpendicular irradiation to the surface of the coated sample. This was made possible by incorporating the LED in a 3D printed PLA (polylactic acid) support, specifically made to fit the diameter of the beaker top part. The RhB solution inside the beaker was also kept under magnetic stirring at a fixed speed to guarantee the continuous supply of the fresh dye-solution to the photoactive sample, allowing for a better homogeneity test solution. The UV-LED test setup is visually summarized in Figure 2.9. The UV LEDs used were Nichia NCSU033B UV SMD-LED. The emission spectrum of this device is reported in Figure 2.10. The LEDs were powered by a potentiostat which outputs a fixed current of 500 mA and regulates

the voltage to keep each LED at its working condition of 3.8 V [89]. Each test lasted six hours and the absorbance of the solution was measured every hour. The instrument used for these measurements was the absorbance spectrophotometer Thermo Scientific^{TM} SPECTRONIC^{TM} 200E (Figure 2.11).

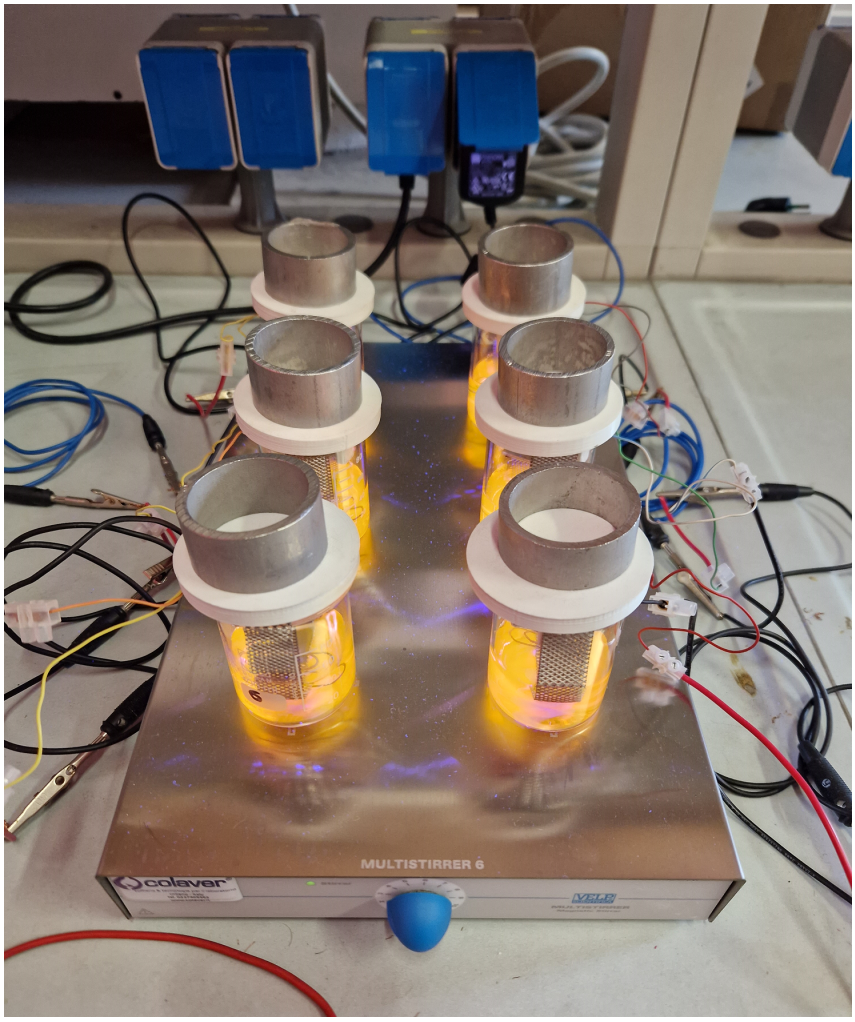

Figure 2.9: UV-LED photocatalytic degradation test laboratory setup.

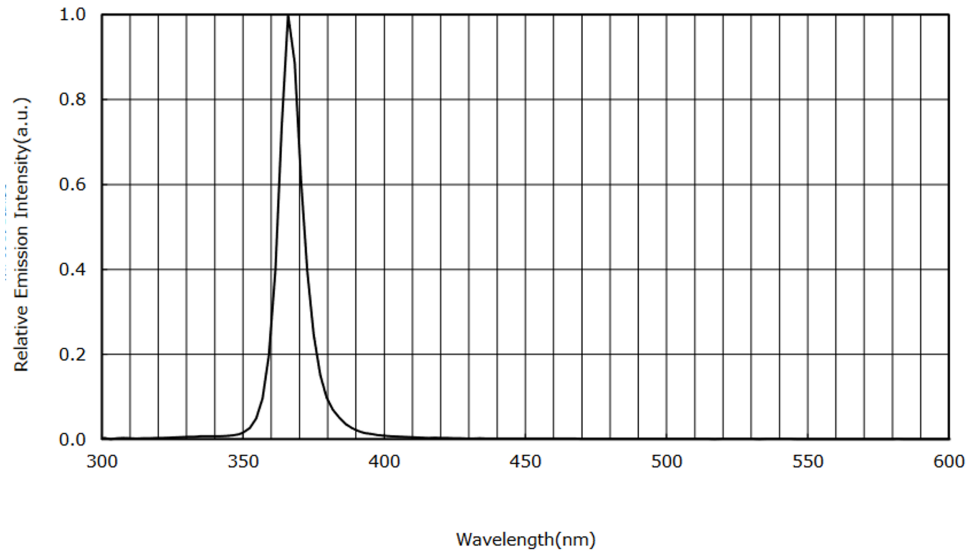

Figure 2.10: Emission spectrum of Nichia NCSU033B UV SMD-LED [89].

Figure 2.11: Spectrophotometer Thermo Scientific^{TM} SPECTRONIC^{TM} 200E [90].

The machine works by emitting a beam of light of wavelengths (λ) between 400 and 700 nm. The instrument then detects the absorbance (A) of the solution by complying the ratio between the intensity after the beam has passed through the dye solution (I) and the emitted intensity (I_0) (Equation (2.1)). The latter is contained in a polystyrene cuvette which is almost transparent and it is placed inside the special slot in the central box of the machine. Using the Lambert-Beer law it is possible to convert the absorbance value (A) output from the spectrophotometer to the

concentration (C) of the dye in the analyzed solution (Equation (2.2)).

$$A = -\log \frac{I}{I_0} \tag{2.1}$$

$$A = l \cdot C \cdot \epsilon \tag{2.2}$$

Where l is the optical path length, and ϵ the absorptivity of the species in solution.

Since all the tests were performed with the same materials and setup, both these values are constants for all the measurements. Due to this fact it was possible to use the absorbance data to compare concentration values and their decrease over irradiation time, and eventually calculate the reaction rate constant (k) for the reaction of photocatalytic degradation of the dye solution. This reaction fits in a pseudo first order kinetic model described by the Langmuir-Hinshelwood equation (Equation (2.3)):

$$\ln \frac{C}{C_0} = -k \cdot t \tag{2.3}$$

where C_0 is the concentration of the dye at time 0, t is the time at which the measurement is taken, and k can be obtained by the slope of the line that interpolates the $\ln \frac{C}{C_0}$ data and the time data.

2.7.2. UV-VIS photocatalytic degradation test

These tests were performed similarly to the ones mentioned in the previous section but the setup was different. The photoactive samples were put inside small plastic transparent dishes containing 8 mL of the rhodamine B solution each; in this case it was a $5 \cdot 10^{-6}$ M solution. Six to eight samples were put under a solar lamp ULTRA-VITALUX 300W E27 (Figure 2.12) at a fixed distance of 60 cm. Samples were arranged to be in iso-irradiance spots where the UV irradiance was close to 1000 μW/cm^2. These spots were identified by first making a grid on the floor and then measuring the average irradiance in each cell through a Konica Minolta UM-10 optical power meter (Figure 2.13).

Figure 2.12: ULTRA-VITALUX 300W E27 solar lamp.

Figure 2.13: Konica Minolta UM-10 optical power meter [91].

The samples were put on a movable sample holder in order to facilitate the measurement step. A Pyrex glass baking dish filled with 500 mL of tap water was held suspended at a fixed distance of 4.5 cm above the samples. Its role was to attenuate the infrared portion of the lamp emitted radiation while allowing the complete passage of the UV light. This was done to reduce as much as possible the evaporation of the Rhb solution, avoiding uncontrollable changes in its concentration during the test. Each test was performed for two hours and measurements were

taken every 15 minutes. Since the irradiance under the lamp was close to 1000 μW/cm^2 but not homogeneously distributed, samples were rotated by one spot after each measurement, creating a situation where each sample was exposed to the same average optical power across the whole test. Moreover, each solution was manually stirred before being put under the lamp to improve the feeding of fresh solution to the photocatalyst, since, overall, the solution is static during the reaction as no magnetic stirring is allowed in this configuration. The setup for this test is visually summarized in Figure 2.14.

Figure 2.14: UV-VIS photocatalysis laboratory setup.

The measurement step is identical to the one mentioned in section 2.7.1 and all the equations reported there are valid also in this case.

2.7.3. Photolysis

For both the techniques presented in the last two subsections, a test without using the photocatalyst was performed in order to understand the amount of photo-induced degradation of the RhB solution caused by just the exposure to UV light. These tests were particularly important

to check the validity of the UV-VIS method, since the small amount of solution and the low concentration of this reagent could have led to unrepresentative results in case of high photolysis.

2.8. Samples characterization

To better understand the structure and the surface features of the deposited TiO_2 thin films, several analyses have been performed. Namely, scanning electron microscopy (SEM) and x-ray diffraction (XRD) were used to investigate some of the samples produced, to identify the structure-to-properties relationship in samples which showed different levels of photocatalytic activity. In addition, also the sol-gels themselves have been characterized, in particular, for what concerns the nanoparticles size and size distribution. The employed technique was the dynamic light scattering in the size measurement mode. All these laboratory techniques will be briefly presented in the following.

2.8.1. Scanning Electron Microscopy (SEM)

SEM is employed to observe the surface of materials. In SEM, high energy electrons are shot on the sample and then the outcoming electrons/X-rays are analysed. These electrons/X-rays do not give only information about the morphology of a material but also on its composition and crystallographic structure. SEM is equipped with a sample holder where the stub should be fixed containing the sample on the surface. Typically, carbon tap is used for sticking the sample to the stub. To be analyzed with SEM, the samples have to be electrically conductive to avoid overcharging on the surface, which could result in extreme brightness or poor images. Hence, non-conductive samples like glass and ceramics are usually sputter-coated with a thin layer of carbon or metals such as gold and platinum. In addition, a requirement for SEM is to operate under a vacuum to avoid interactions between electrons and gas molecules that could cause lower resolution [92].

In this work, the EVO 50 Extended Pressure by Zeiss (Figure 2.15) was used to analyze the surface morphology of the best performing samples alongside some of the worst and mid-performing ones. Whenever possible, it was used also to measure the thickness of the deposited coating.

Figure 2.15: Scanning electron microscope EVO 50 Extended Pressure by Zeiss.

2.8.2. Energy Dispersive X-Ray Spectroscopy (EDX)

EDX spectroscopy is a technique involved in the elemental composition detection of materials analyzed with SEM. EDX is able to identify elements that have atomic numbers higher or equal to the one of boron and can detect them if their concentration is at least 0.1% [93].

The way EDX analysis works is that the electron beam hits the inner shell of an atom, knocking off an electron from the shell, while leaving a positively charged electron hole. When the electron is displaced, it attracts another electron from an outer shell to fill the vacancy. As the electron moves from the outer higher-energy to the inner lower-energy shell of the atom, this energy difference can be released in the form of an X-ray (Figure 2.16). The energy of this X-ray is unique to the specific element and transition and, for this reason, it is possible to differentiate between different elements and ultimately measure their concentration [93].

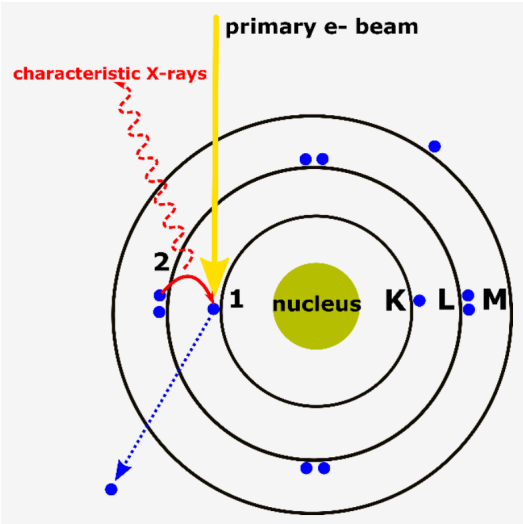

Figure 2.16: Two-step process for the EDX x-ray generation. First, the energy transferred to the atomic electron knocks it off, leaving behind a hole. Second, its position is filled by another electron from a higher energy shell, and the characteristic x-ray is released [93].

In this work, the EDX spectroscopy measurements were performed using a Bruker XFlash® 6-30 detector (Figure 2.17) attached to the SEM equipment. The analysis was performed in the spot mode, to characterize the surface elemental composition of several deposited coatings.

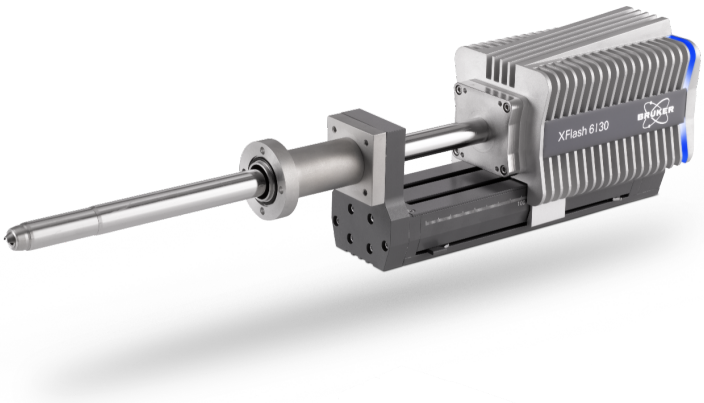

Figure 2.17: Bruker XFlash® 6-30 EDX detector.

2.8.3. Dynamic Light Scattering (DLS)

Dynamic Light Scattering is used to probe particles size and their distribution. The technique is really valuable in monitoring colloidal solutions and, in particular, the gelation and aggregation processes. DLS is based on the study of how coherent light, scattered by a solution containing

diffusing particles, changes with time. The time-correlation function of these scattered intensities provides information about their diffusivity and, most importantly, their size. The typical DLS setup uses a monochromatic emitter (a laser) to direct a parallel beam of coherent light towards a transparent cuvette containing a diluted colloidal solution. Most of the beam will travel through the sample and hit a screen, placed a large distance away from the sample (far-field realisation). On the screen, a large number of macroscopically visible light dots (speckles) appear and continuously move around. These speckles appear due to the constructive interference of the incoming light scattered by the particles in solution. The resulting set of speckle patterns is analyzed by an autocorrelator that compares the intensity of light at each spot over time. The output measure is the hydrodynamic diameter of the particles alongside with the particles size distribution by intensity. The detectable sizes can range from few nanometers to few micrometers [94]. The general setup of the DLS technique and a typical output spectrum are reported respectively in Figure 2.18 and Figure 2.19.

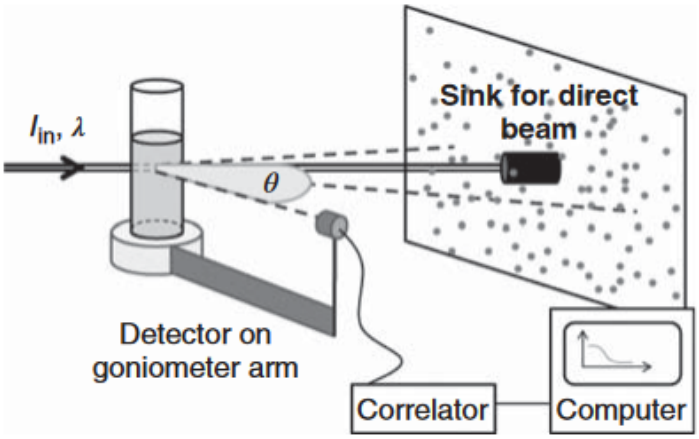

Figure 2.18: General DLS setup. (I_{in}=incident light intensity, λ=monochromatic light wavelength, θ=scattering angle) [94].

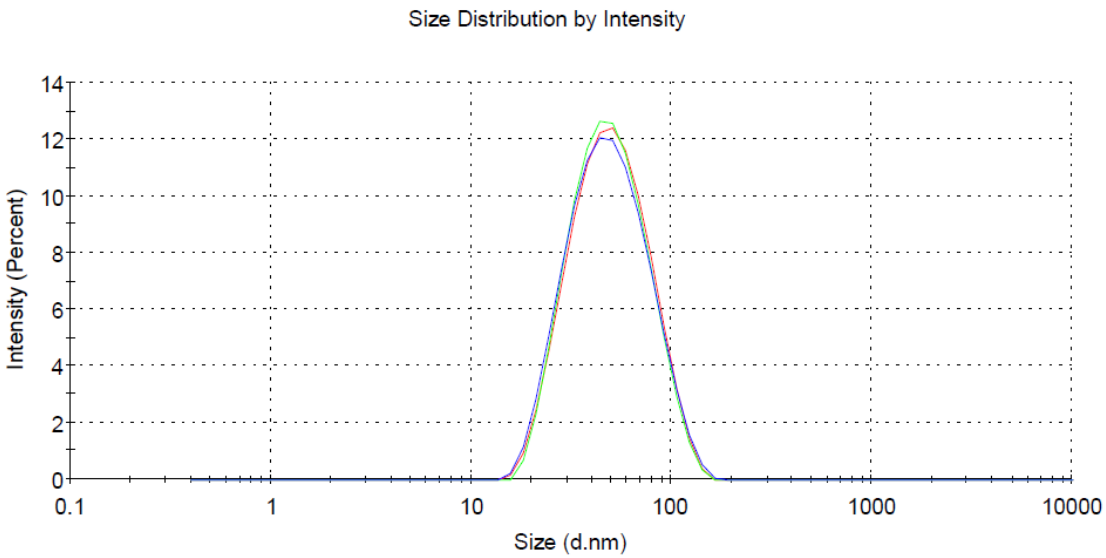

Figure 2.19: Typical spectrum for the particles size distribution, output of the DLS measurement.

In this work the Dynamic Light Scattering measurements were performed using a Zetasizer Nano ZS by Malvern Analytical (Figure 2.20). Each measurement was performed by diluting a small quantity of the analyzed sol-gel in its proper solvent in a volumetric ratio of 1:10 and putting the diluted liquid in a typical disposable sizing cuvette. All the measurements were performed at 25°C with a fixed calibration time of 120 seconds. The output values selected for these experiments were the average particles hydrodynamic diameter, the particles size distribution by intensity, and the correspondent polydispersity index (PdI), the latter being an useful parameter to determine the broadness of the distribution.

Figure 2.20: Zetasizer Nano ZS by Malvern Analytical.

3 | Results and discussion

In this chapter all the results concerning the prepared sol-gels and deposited thin films will be presented and subsequently discussed to clarify what was observed. First of all, a brief overview of a typical UV-VIS photocatalytic test will be presented in order to show the methodology used to collect and report data. In a later section, the results of the photolysis tests are reported to understand, prior to the main discussion, the impact of the experimental conditions on the photocatalytic tests. Further in this chapter all the main tests results will be listed and compared to highlight the best performing samples and the times at which their best performance has been achieved. In the last sections, all the results concerning the characterization tests will be reported, to understand and discuss the trends observed in photoactivity. Prior to the whole discussion, the results concerning crystalline nanocellulose will be shown as they will be useful for later results presentation.

3.1. Crystalline nanocellulose synthesis results

Crystalline nanocellulose was synthesized via the acid hydrolysis method, as presented in section 2.2. The final product was ultrasonicated to obtain a homogeneous dispersion that had a semi-opaque, translucent appearance (Figure 3.1).

Figure 3.1: Appearance of synthesized CNC suspension.

This final product was then tested using the DLS instrument in order to identify the success of the reaction. In particular, this was done by checking the average particle size inside the dispersion. A dilution 1:10 wt. of the latter was prepared for the test. The DLS output results are reported below in Figure 3.2.

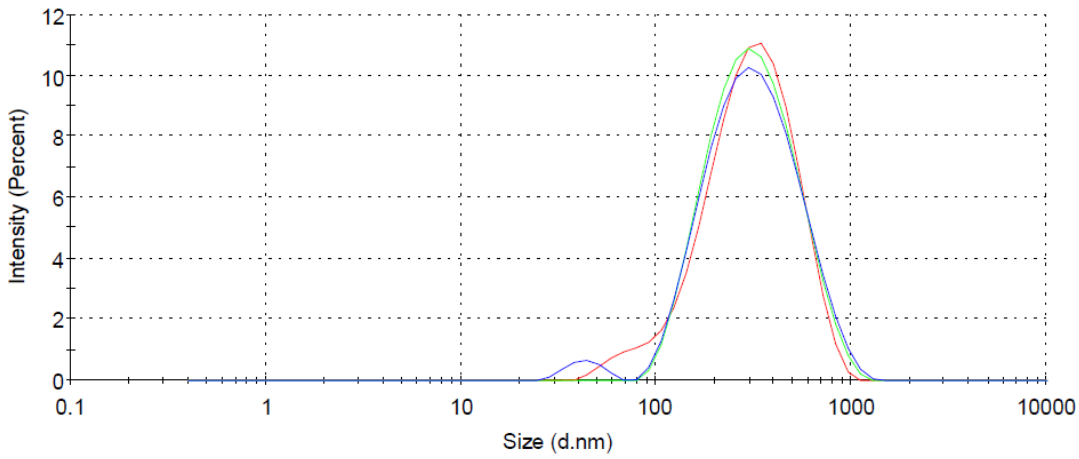

Figure 3.2: Size distribution by intensity plot of CNC synthesized via acid hydrolysis, output of the DLS analysis.

The average diameter of the dispersed particles was identified equal to 254 nm and the polydispersity index (PdI) equal to 0.250. From these results it was possible to confirm the nanometric nature of the syntesized material; the size distribution was also fairly narrow, as the PdI was quite low.

The unknown characteristics of this nanocellulose were its composition, the yield of the reaction and the % of dispersed solid inside the water solution. It was known that the CNC contained residues of $NaSO_4$ as the neutralization reaction was not conducted stoichiometrically. To identify the yield of the hydrolysis it is necessary to perform further purification steps such as dialysis, to selectively remove the Na^+ and SO_4^{2-} ions, and then a drying step to determine the total nanocellulose mass. These steps were not performed during this work due to time reasons, however, to determine the amount of solid present in the water dispersion a drying step was performed. A portion of the nanocellulose suspension was left to evaporate for 14 days in order to measure the mass variation caused by the evaporation of the solvent. This experiment was repeated twice to obtain a more reliable value of the solid amount present in the suspension. The results of these experiments are reported in Table 3.1.

Table 3.1: Results of the evaporation tests to determine the % of solid present in the acid hydrolysis-synthesized CNC dispersion.

Exp. n°	Tare [g]	Initial mass [g]	Final measured mass [g]	Solid mass in dispersion [g]	Solid % in dispersion
1	3.5329	9.9983	3.6032	0.0703	0.70
2	4.3358	25.6698	4.5128	0.1770	0.69

The two experiments were conducted using different volumes of suspension, namely 10 mL and 25 mL, coming from different vials in which the suspension was divided. Each value reported in the table is the mean value of 4 weight measurements, performed using a 4 digits balance. From these results is was possible to identify that the percentage of solid material, present in the nanocellulose dispersion, was 0.70%. This value was later used to prepare dilutions for the sol-gel formulation using CNC as the templating agent.

3.2. Data collection methodology

The experimental procedure of photocatalytic tests has already been described in section 2.7.2 and it involves taking absorbance measurements at set time intervals for a total of 2 or 6 hours, depending on the test type. To ensure the precision of the absorbance values, three measurements were taken every time and the mean value was selected as the actual absorbance of the

rhodamine B solution at each specific time. The tare of the cuvette was then subtracted from the mean value to obtain the real absorbance of the dye solution (Figure 3.3).

Sample n°	1		
Description	E-T10-L7-R W6		
Cuvette tare	0,007		
Time \ Abs values	measured	avg	real
0'	0,425	0,426	0,419
	0,425		
	0,429		
15'	0,408	0,409	0,402
	0,408		
	0,410		
30'	0,393	0,394	0,387
	0,394		
	0,395		
45'	0,379	0,378	0,371
	0,378		
	0,377		
1h	0,358	0.357	0.350
	0.356		

Figure 3.3: Example: collection of absorbance data in a typical UV-VIS photocatalysis test. Highlighted in red: real absorbance obtained subtracting the tare of the cuvette from the average value.

After all the absorbance values were collected, it was possible to elaborate the data in order to obtain first the plot of $\Delta C\%$ vs t, using the Equation (2.2) to link the absorbance data to the RhB solution concentration (Figure 3.4). Then, using Equation (2.3) a new plot was obtained (Figure 3.5) representing $\ln(C/C_0)$ vs t, and from the slope of such plot, the value of the degradation kinetic constant was derived (Figure 3.6). For each sample, these measurements were taken every two weeks for 6 to 8 weeks total, yielding a total of 3 or 4 curves per time-plot and 3 or 4 values of k.

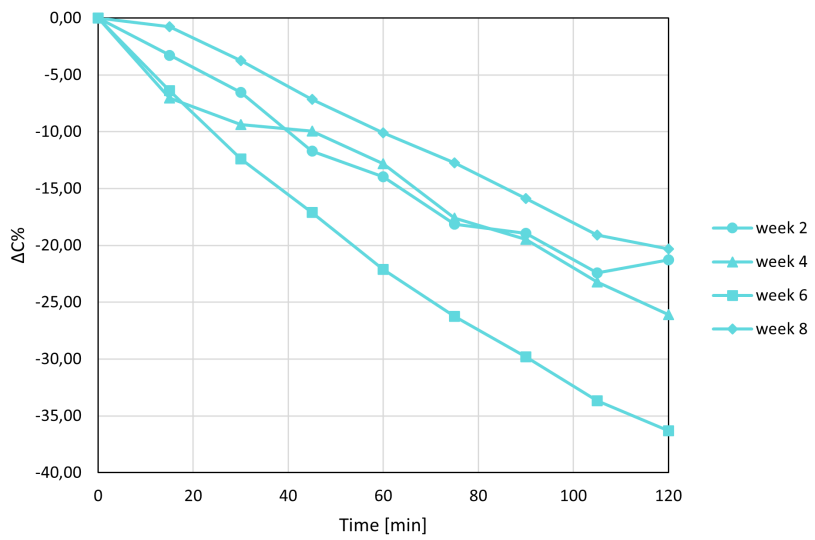

Figure 3.4: Example: ΔC% vs t plot for a sample tested 4 times across 8 weeks.

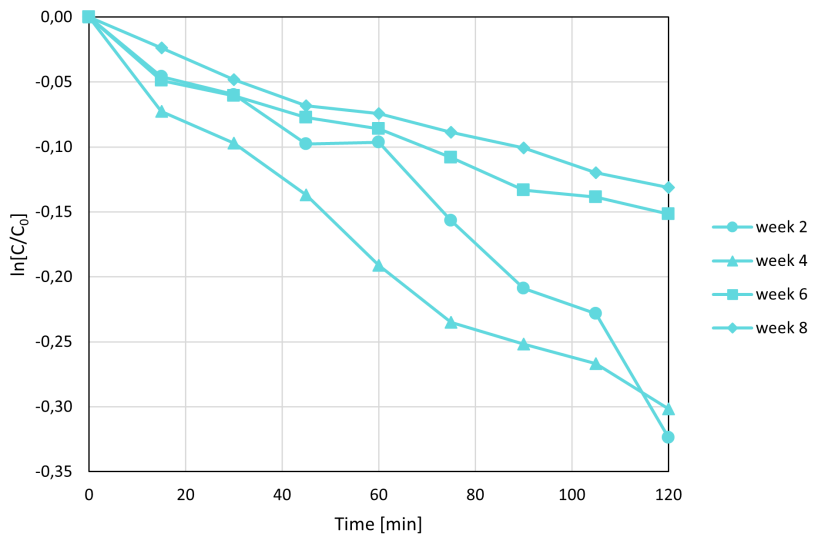

Figure 3.5: Example: $\ln(C/C_0)$ vs t plot for a sample tested 4 times across 8 weeks.

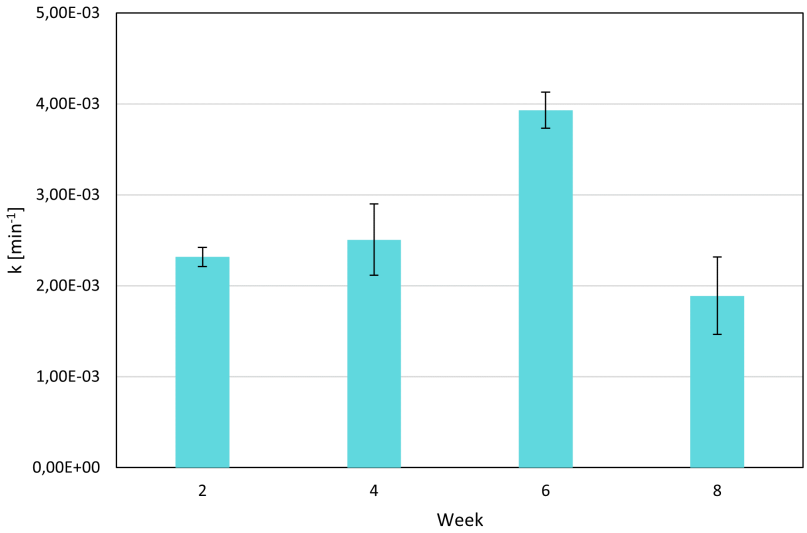

Figure 3.6: Example: kinetic constant values for each 2-week measurement.

3.3. Photolysis results

Before starting with the UV-VIS photocatalytic tests, some degradation tests have been performed without the photocatalyst in order to understand the "error" related to the photo-induced dye degradation and the effect of the solution partial evaporation which was inevitable to a certain extent in this setup.

In Figure 3.7 the results concerning the 2 h photolysis tests are reported. It is possible to see that the effect of exposing the solution to the light source without any TiO_2 catalyst can be quite unpredictable. In most of the cases it led to a very low level of dye degradation, reflected in a small drop in absorbance. In a few cases, the final concentration was higher than the initial one, highlighting a prevalent effect of the solvent evaporation, which in principle led to an increase in RhB concentration inside the dye solution. The experimental error is however quite low if compared to the degradation effect caused by the presence of the photocatalyst. In Figure 3.7, the y-axis scale is set to a range that allows to better visualize the tests results and compare them with each other; however, comparing the "best" photolysis tests (in terms of photodegradation of the dye solution) with an average photocatalytic test result the difference appears evident (Figure 3.8).

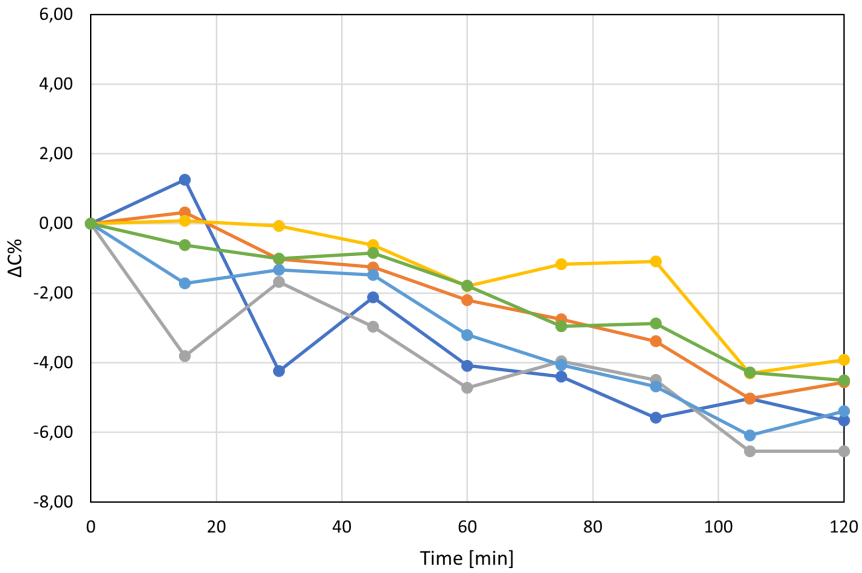

(a) First set of six photolysis tests.

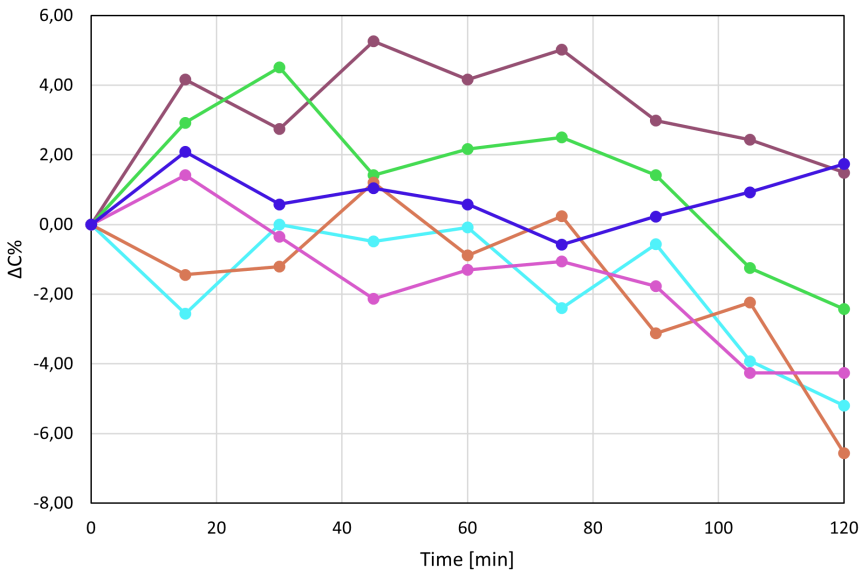

(b) Second set of six photolysis tests.

Figure 3.7: Photolysis tests results (each colored line represents a different test).

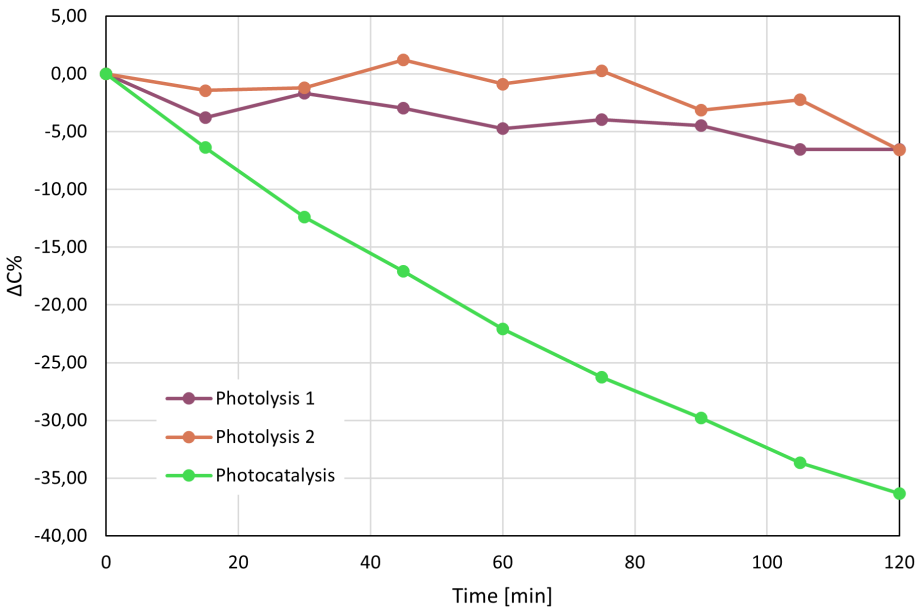

Figure 3.8: Comparison between the photolysis tests that produced the most degradation and an average photocatalysis test.

To fully characterize the UV-VIS photocatalytic tests, also the variation in volume and mass of the RhB solution between the start and the end of the experiment has been monitored to evidence possible evaporation of the solution and explain the observed increase in absorbance. In Table 3.2 all the results of these measurements are listed.

Table 3.2: Volume and mass variation during UV-VIS photolysis tests.

Test n°	Initial volume [mL]	Final volume [mL]	Initial mass [g]	Final mass [g]	Volume change %	Mass change %
1	8.0	7.3	7.84	7.16	-8.75	-8.67
2	8.0	7.4	7.87	7.11	-7.50	-9.66
3	8.0	7.4	7.87	7.18	-7.50	-8.77
4	8.0	7.4	7.86	7.18	-7.50	-8.65
5	8.0	7.3	7.85	7.14	-8.75	-9.04
6	8.0	7.4	7.92	7.15	-7.50	-9.72
7	8.0	7.2	7.87	7.04	-10.0	-10.55
8	8.0	7.2	7.88	7.06	-10.0	-10.41
9	8.0	7.2	7.91	7.07	-10.0	-10.62
10	8.0	7.2	7.86	7.05	-10.0	-10.31
11	8.0	7.4	7.79	7.23	-7.50	-7.19
12	8.0	7.5	7.89	7.34	-6.25	-6.97
Avg	**8.0**	**7.3**	**7.87**	**7.14**	**-8.44**	**-9.21**

It can be seen that an average of 8.5-9% of solution is lost during the test. This can be ascribed both to the evaporation induced by the exposure to the solar lamp and to the inevitable loss of liquid in between measurements, as tiny droplets get stuck in the pipette or in the cuvette. The latter has been found to be less impactful than the actual evaporation as static tests, conducted without collecting the solution every 15 minutes for measurements, revealed that the volume change % was always -7.5%. This meant that the effect related to the pipette was contributing only by a 17% to the total loss of solution. This loss is however quite limited and can be considered small enough to be in the acceptable experimental error range for a test that is not in a controlled and isolated environment.

After all these considerations, it was possible to address the validity and reliability of the UV-VIS photocatalytic tests for the determination of the photoactivity of the TiO_2 thin films. In all the 12 performed photolysis tests the variations observed on absorbance ranged between 2 and 6.5%, hence these limits could be considered as the limit error intrinsic in the experimental setup.

3.4. UV-VIS photocatalysis results and comparison

In this section all the results concerning the sol-gel screening performed by UV-VIS photocatalytic tests will be reported. In particular, a first comparison will be made among deposited sol-gels based on the same solvent, to highlight the differences induced by changing the composition or the preparation technique. Despite few exceptions, all the prepared sol-gels have been tested at least 3 times during the ageing period of 6/8 weeks. The initial formulations have been tested 4 times (up to the 8th week) while the later ones have their results reported up to the 6th week. The reason behind the choices made in this work will be explained further in this chapter. The first step of comparison serves the purpose of identifying the best performing TiO_2 sol-gels which will be subject to further discussion.

3.4.1. Isopropanol-based sol-gels

All the isopropanol-based formulations have been prepared keeping a fixed amount of solvent and acetic acid and varying the type and amount of surfactant while also modifying the quantity of titanium precursor. All the sol-gels have either a 1:45:5 or a 1.2:45:5 molar ratio between titanium(IV) isopropoxide, isopropanol and acetic acid, while the amount of added surfactant changes depending on the type or the order of addition of the reagents. This has been done to check the stability of the solution at higher contents of TTIP starting from a known stable ratio [58].

Sodium dodecyl sulfate based sol-gels

The sol-gels I-T10-S20-N and I-T12-S20-N have been prepared with a fixed ratio of 45:5:0.2 between isopropanol, acetic acid and SDS while the relative molar amount of TTIP is 1 in the first case and 1.2 in the second. In these cases the surfactant was firstly added to the solvent, then acetic acid was put in the solution dropwise and lastly TTIP was added in the same way. The sample I-T12-S20-R has been formulated with the same molar ratio as I-T12-S20-N, but in this case the order of addition was different: a solution of TTIP and acetic acid was poured into the solvent in which the surfactant was previously dissolved. The results for the UV-VIS photocatalytic degradation of rhodamine B solution ($5{\cdot}10^{-6}$ M) are reported in Figure 3.9. For comparison purposes, the curve relative to a known photoactive sample is also reported to set the scale of the graphs and to help identifying the quality of the sol-gels. This sol-gel was prepared and aged for more than two months following the preparation procedure reported by Antonello et al. [61] and it is indicated by the label "X" in the following plots.

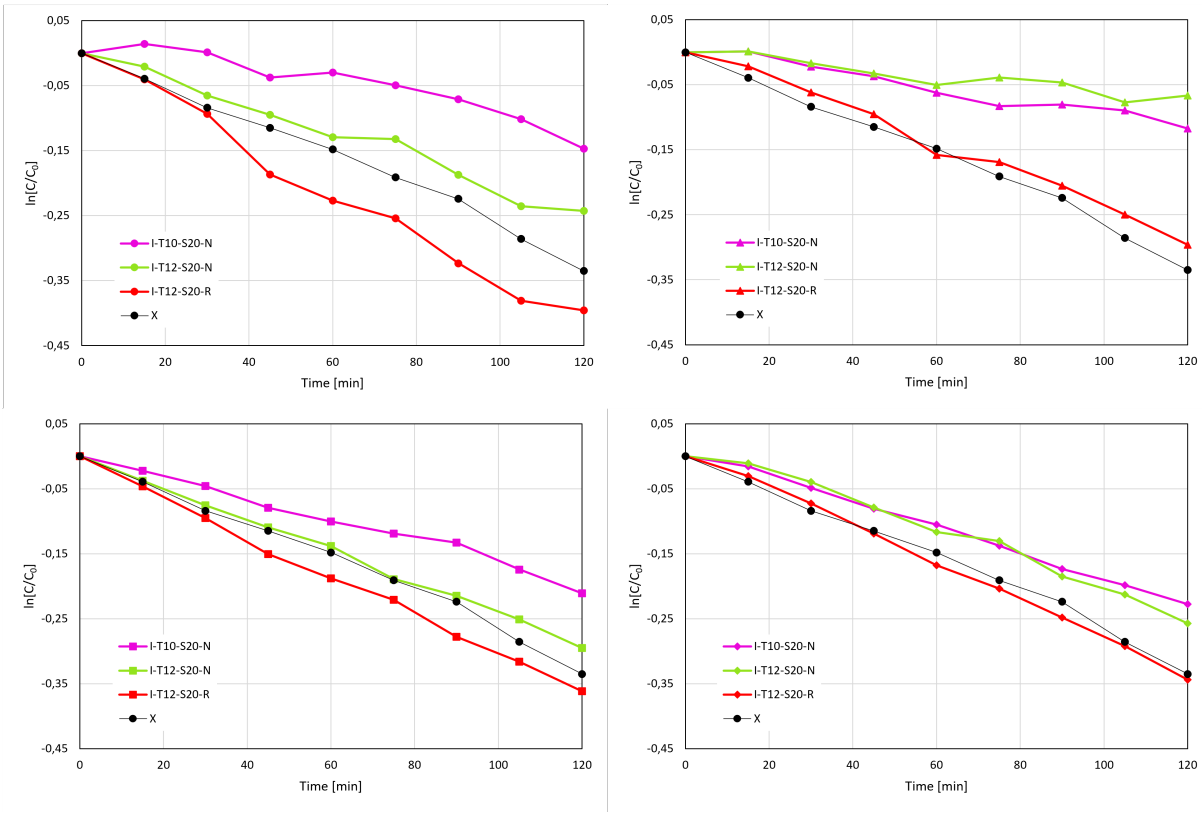

Figure 3.9: Results comparison of UV-VIS photocatalysis for isopropanol and SDS based sol-gels. Each plot compares the results obtained at the same amount of ageing time, namely 2 (top left), 4 (top right), 6 (bottom left), 8 (bottom right) weeks.

These curves show that the trend of the degradation actually follows a pseudo-first-order kinet-

ics, confirming the applicability of the Lambert-Beer law. This is confirmed also by the value of R^2 of the interpolation line, which is at least equal to 0.99 in all the cases shown above.

Below, in Figure 3.10, the photodegradation kinetic constants *k* are also reported.

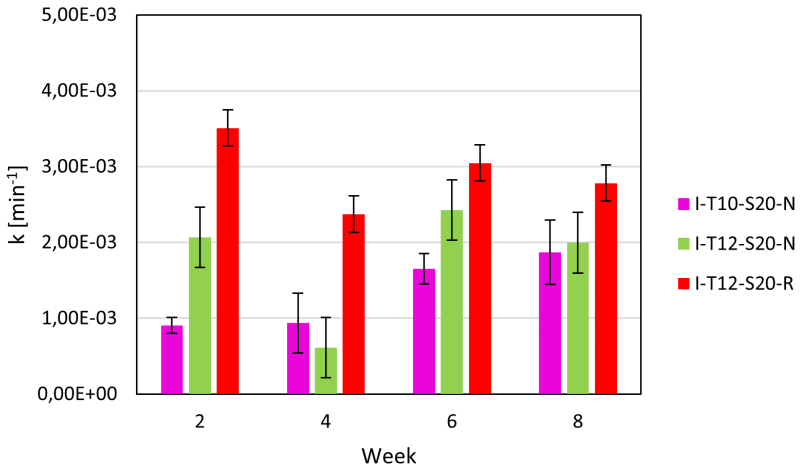

Figure 3.10: Results comparison between the obtained kinetic constants *k* for the isopropanol and SDS based sol-gels at 2, 4, 6, 8 weeks.

Among these sol-gels only the I-T12-S20-R showed a significant photoactivity after 2, 6, and 8 weeks. The fluctuation in the reactivity during week 4 could be ascribed to several factors, but the main one could be the nanoparticles agglomeration and segregation to the bottom of the solution. It could be seen that there was a white precipitate in the bottom of the beaker (Figure 3.11) resulting in a slight reduction in the photoactivity of the final sample. Before each deposition step, a strong mechanical mixing and sonication of the sol-gel has been performed to avoid this phenomenon as much as possible, but still the amount of SDS is high enough to drive the solution to a state of segregation. The increase after 6 weeks could be addressed instead to the condensation reaction that proceeded and took the photoactivity to a level comparable to the one of week 2. A similar trend can be seen for samples I-T10-S20-N and I-T12-S20-N where the drop in photocatalytic activity after 4 weeks is stronger for I-T12-S20-N due to the fact that the amount of precursor was higher, leading to a worse segregation with respect to the other sample, while having a higher photoactivity after 2 and 6 weeks. The phenomenon of segregation due to particles agglomeration was furtherly supported by the DLS analysis which will be reported later in this work.

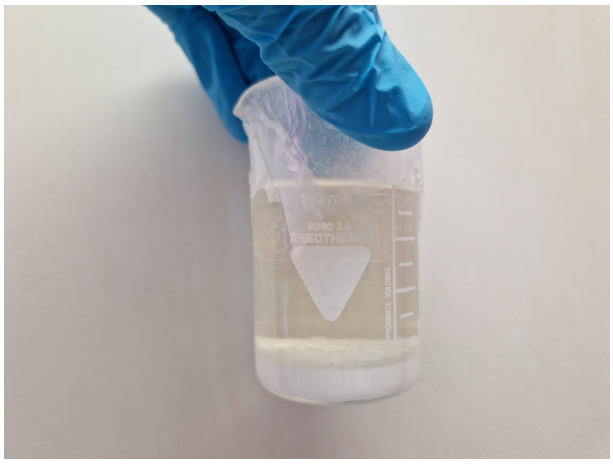

Figure 3.11: Segregation of an isopropanol and SDS based sol-gel (I-T12-S20-N) at the 4th week.

Another parameter tested with these samples was the order of addition of the reagents. From the results it could be seen that the sol-gel created with the reverse addition method (I-T12-S20-R) showed higher photoactivity with respect to the ones made with the normal addition method (I-T10-S20-N and I-T12-S20-N). This could be explained by the fact that during the reverse reaction, the titanium precursor reacts firstly with the acid, forming titanium alkoxide intermediates which are then readily available to be hydrolysed when added to the OH-containing solvent, leading to a more ordered nucleation of particles; on the other hand, by performing the normal addition method, the formation of the titanium intermediates can take place in a less homogeneous way inside the acidified solvent.

SDS-based sol-gels showed a promising but fluctuating reactivity and they were not fully stable during the period in which they were tested. The anionic nature of this surfactant can enhance the particles segregation in the situation where some natural photoreduction affects TiO_2 nanoparticles, leading to the formation of negatively charged species which are subjected to electrostatic repulsion towards SDS. For this reason, the particles are pushed out of the solution causing segregation. SDS is also usually less soluble in organic solvents with respect to water.

For the aforementioned reasons, SDS-based sol-gels were not further prepared and tested to assess their photocatalytic activity. Further into this work, another SDS-based sol-gel will be discussed since it was formulated prior to the results discussion.

Ecosurf eh-3 based sol-gels

The sol-gels I-T10-E50-N and I-T12-E50-N have been formulated with the two different ratios 1:45:5 and 1.2:45:5 between TTIP, isopropanol and acetic acid. Since the molar weight of Ecosurf eh-3 is unknown, the quantity chosen for the two formulations was fixed at 0.5 g in order to exceed the critical micelle concentration (CMC) with the aim of creating a more homogeneous solution. After 2 weeks the solution showed a strong crystallization at the bottom of the beaker (Figure 3.12).

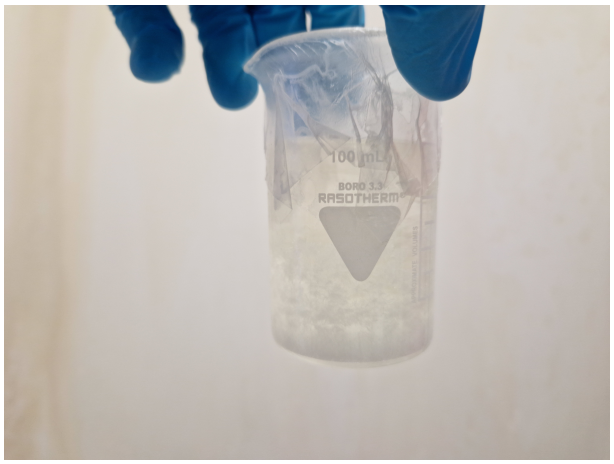

Figure 3.12: Bulk crystallization at the bottom of the beaker containing an isopropanol and Ecosurf eh-3 based sol-gel (I-T12-E50-N) at the 2nd week.

The results regarding photocatalytic activity towards UV-VIS degradation of RhB solution ($5{\cdot}10^{-6}$ M) also revealed a very low reactivity. This can be seen in the plot reported below (Figure 3.13) and from the value of the kinetic constant k (Figure 3.14). In the former, the previously mentioned reference sample has also been reported and indicated as "X".

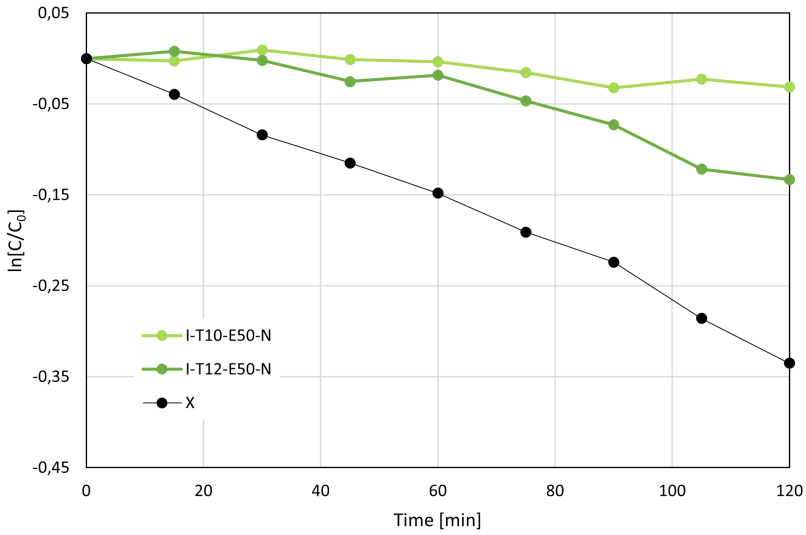

Figure 3.13: ln(C/C$_0$) vs time plot of isopropanol and Ecosurf eh-3 based sol-gels at the 2nd week compared with the known sample "X".

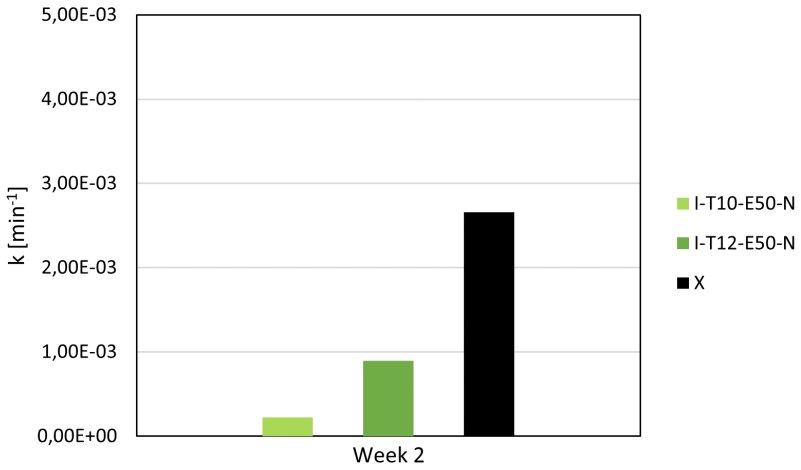

Figure 3.14: Results comparison between the obtained kinetic constants *k* for the isopropanol and Ecosurf eh-3 based sol-gels at 2 weeks and known sol-gel "X".

The crystallization of TiO_2 inside the solution could be identified as the main cause of the low photoactivity of these sol-gels. This phenomenon could be ascribed to the fact that the concentration of Ecosurtf eh-3 was too high, leading to the formation of agglomerates of titanium dioxide within the micelles with a consequent macroscopic crystallization of such aggregates.

For this reason the tests were stopped at week 2 and no other sol-gel was formulated with the previously mentioned amount of Ecosurf eh-3. Further in this work other sol-gels based on this

surfactant are discussed but the solvent used was water, for which the CMC value could be used more reliably.

Lutensol ON70 based sol-gels

The sol-gels I-T10-L20-N and I-T12-L20-N have been prepared with a fixed ratio of 45:5:0.2 between isopropanol, acetic acid and Lutensol ON70 while the molar amount of TTIP is 1 in the first case and 1.2 in the second. These formulations were made following the normal addition method, where the surfactant was firstly added to the solvent, then the acetic acid was put in the solution dropwise and lastly the TTIP was added in the same way. On the other hand, sol-gel I-T12-L20-R was prepared following the reverse addition method, while keeping the same ratio between the reagents as sol-gel I-T12-L20-N. The results concerning photocatalytic activity towards UV-VIS degradation of RhB solution ($5{\cdot}10^{-6}$ M) are reported in Figure 3.15 and the values of the kinetic constants k are shown in Figure 3.16. Again, the previously mentioned sample "X" is present as a reference value.

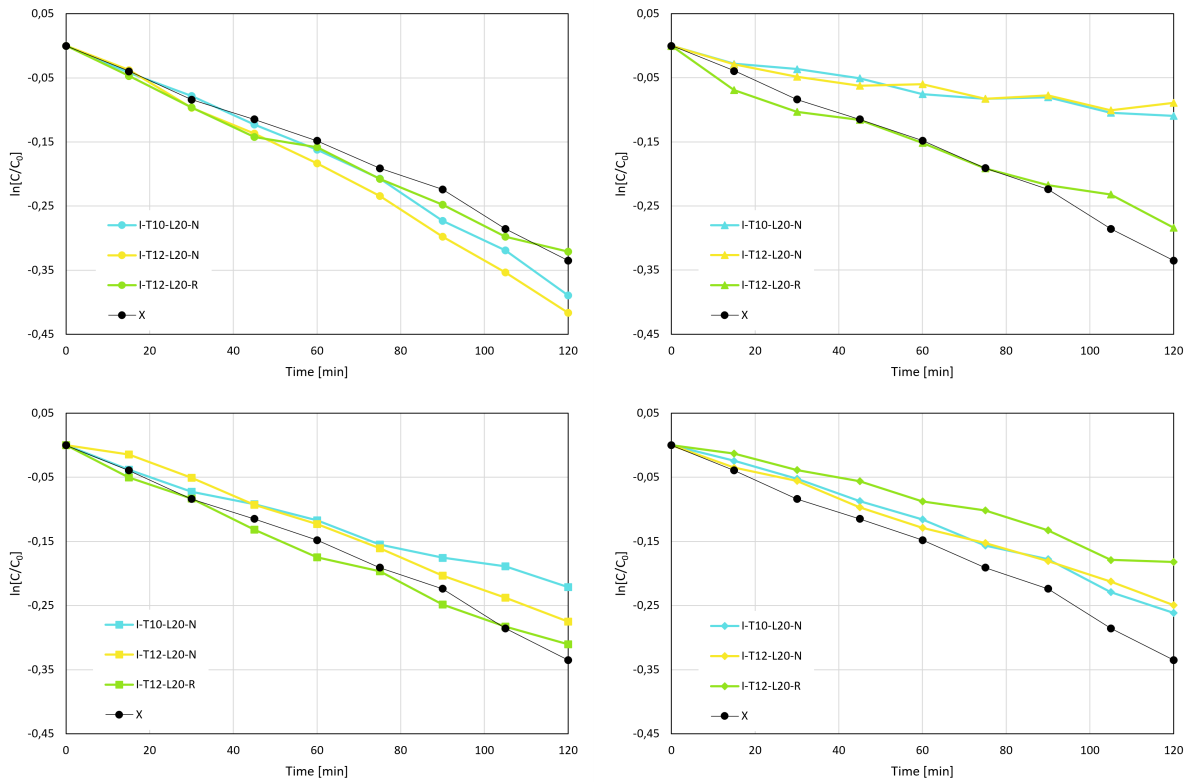

Figure 3.15: Results comparison of UV-VIS photocatalysis for isopropanol and Lutensol ON70 based sol-gels. Each plot compares the results obtained at the same amount of ageing time, namely 2 (top left), 4 (top right), 6 (bottom left), 8 (bottom right) weeks.

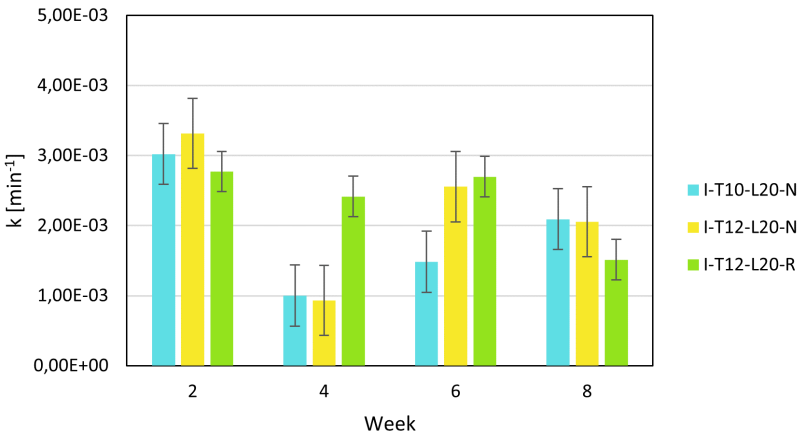

Figure 3.16: Results comparison between the obtained kinetic constants k for the isopropanol and Lutensol ON70 based sol-gels at 2, 4, 6, 8 weeks.

The trend for sol-gels I-T10-L20-N and I-T12-L20-N is similar compared to their SDS-based counterparts (I-T10-L20-N and I-T12-S20-N). The main difference is the higher photoactivity shown after the first two weeks. This could be addressed to the nature of the surfactant, that, in the case of Lutensol ON70, is non-ionic, hence, it formed more uniform micelles inside the solvent, leading to a more homogeneous solution in the first reaction steps. Moreover, alkyl polyethylene glycol ethers are more soluble in polar organic solvents with respect to SDS, indeed, the sol-gels after two weeks did not show any sign of precipitation (Figure 3.17).

Figure 3.17: Appearence of an isopropanol and Lutensol ON70 based sol-gel (I-T12-L20-N) at the 2nd week. No visible precipitation is present.

In week 4 and 6 the same effect reported for SDS sol-gels could be identified. On the 4th week, some precipitation was present due to the ageing of the sol-gel (Figure 3.18), meaning that, on

the long term, isopropanol and the surfactant were not enough to maintain a stable solution. To counteract this precipitation, also in this case, strong mechanical mixing was performed before each dip-coat deposition. Again, on the 6th week, the photoactivity slightly increased due to the progress of the condensation reaction, however it never reached the initial values and after 8 weeks it dropped slightly.

Figure 3.18: Precipitation of TiO_2 particles inside an isopropanol and Lutensol ON70 based sol-gel (I-T12-L20-N) at the 4th week.

I-T12-L20-N follows the same trend as I-T12-S20-N, as it is more active than I-T10-L20-N in weeks 2 and 6 while it shows higher degrees of precipitation, hence, lower photoactivity, during week 4. Also in this case, for what concerns the order of addition of the reagents, I-T12-L20-R, prepared with the reverse addition method, showed overall higher reactivity than the two sol-gels prepared with the normal addition method in weeks 4 and 6. On week 2, however, a bulk precipitation happened (Figure 3.19) and probably caused the photoactivity to be lower than I-T10-L20-N and I-T12-L20-N.

Figure 3.19: Bulk precipitation of TiO_2 particles inside an isopropanol and Lutensol ON70 based sol-gel (I-T12-L20-R) at the 2nd week.

After 8 weeks, the photocatalytic activity of the Lutensol ON70 based sol-gels with higher amounts of TTIP decreased. From this, it could be deduced that if the precursor exceeds a certain quantity, for a fixed amount of solvent and surfactant, the sol-gel system becomes more unstable, the ageing process happens more quickly and the TiO_2 particles tend to precipitate and agglomerate. The stabilizing effect of the surfactant is not enough to sustain the titanium dioxide quantity and overall the photocatalytic activitiy that can be achieved is quite low.

Isopropanol-based sol-gels did not reach high performance and most of them were not stable across the 8 weeks testing time. The solvent amount turned out to be too low to withstand the ageing period. On the other hand, sol-gels based on isopropanol showed good aesthetic appearance once dip-coated onto the glass substrates. In particular, in Figure 3.20, the appearance of samples I-T12-L20-N and I-T12-S20-R at their second week is shown, since, among all isopropanol-based sol-gels, they were the ones showing the highest photoactivity. Good transparency and surface homogeneity characterize the first one, while the second showed a more inhomogeneous frame, despite being transparent.

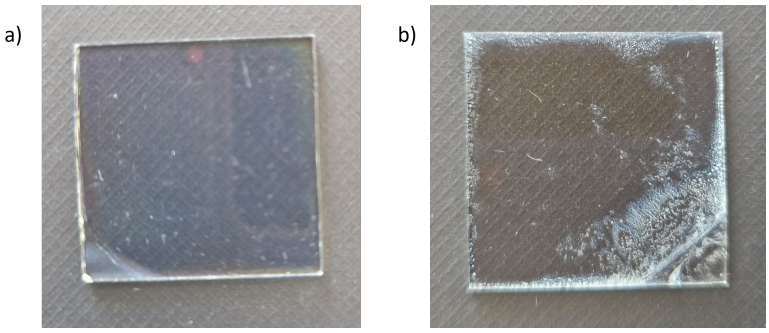

Figure 3.20: Aesthetic appearance of samples I-T12-L20-N (a) and I-T12-S20-R (b).

3.4.2. Ethanol-based sol-gels

All the ethanol-based formulations have been prepared keeping a fixed amount of solvent and acetic acid and varying the type and amount of surfactant while also modifying the quantity of titanium precursor. All the sol-gels have a 1:40:1 molar ratio between TTIP, ethanol and acetic acid, while the amount of added surfactant changes depending on the type or the order of addition of the reagents. This has been done to check the stability of the solution at higher contents of TTIP. Overall, few formulations have been prepared using ethanol, since it was reported in previous works that ethanol-based sol-gels were less photoactive than the water-based ones. For this reason, results will be presented without sorting them based on the used surfactant.

E-T10-S5-R was the only ethanol and SDS based sol-gel, it was prepared soon after the two isopropanol based ones (I-T10-S20-N and I-T12-S20-N). As for the latter, also this one was formulated to test the effect of the surfactant in maintaining the stability of the sol-gel at relatively low amounts of solvent, to ultimately achieve a product highly concentrated in TiO_2. The chosen addition method was the reverse one, following the procedure reported in previous works [87, 95]. E-T10-L7-R was produced with Lutensol ON70 as the surfactant, and it was the Lutensol-equivalent of E-T10-S5-R. Also in this case, it was formulated following the reverse addition method. No Ecosurf eh-3 based sol-gel was produced due to the macroscopic crystallization event, previously described for the other organic solvent used in this work.

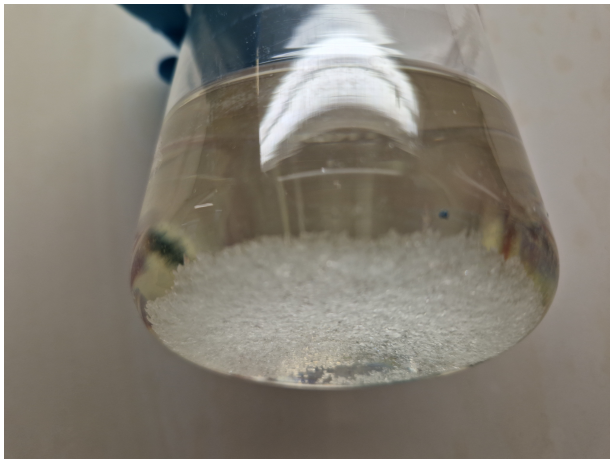

Figure 3.21: Precipitation of TiO_2 crystals inside sol-gel LA12M2.

Sol-gels LA12M2 and LA14M3 were exceptions in terms of formulation technique. They were the reproduction of the sol-gel presented by Antonello et al. [61] to compare their ageing (across the 6/8 weeks time period) with the other sol-gel formulations. Acetic acid was absent while hydrochloric acid was used to modify the pH of the sol and catalyze the reaction. Sol-gel

LA12M2 was quickly subject of an unpredictable crystallization at the bottom of the solution and for this reason was remade into LA14M3. This event could be explained by the presence of hygroscopic impurities or humidity inside the reaction beaker. The presence of water allowed the reaction rate for the gel formation to be faster in those localized regions, ultimately leading to crystallites precipitation at the bottom of the beaker (Figure 3.21).

Below, the results of the UV-VIS tests involving the ethanol based sol-gels are presented (Figure 3.22) alongside the obtained degradation kinetic constants (Figure 3.23). In the former plots, the previously mentioned sample "X" is present as a reference value. Sample LA14M3 was tested for 6 weeks only. This decision was taken for many sol-gels as the highest values of photoactivity were all obtained during the first 6 weeks. This direction was taken also to, overall, allow the testing of more formulations.

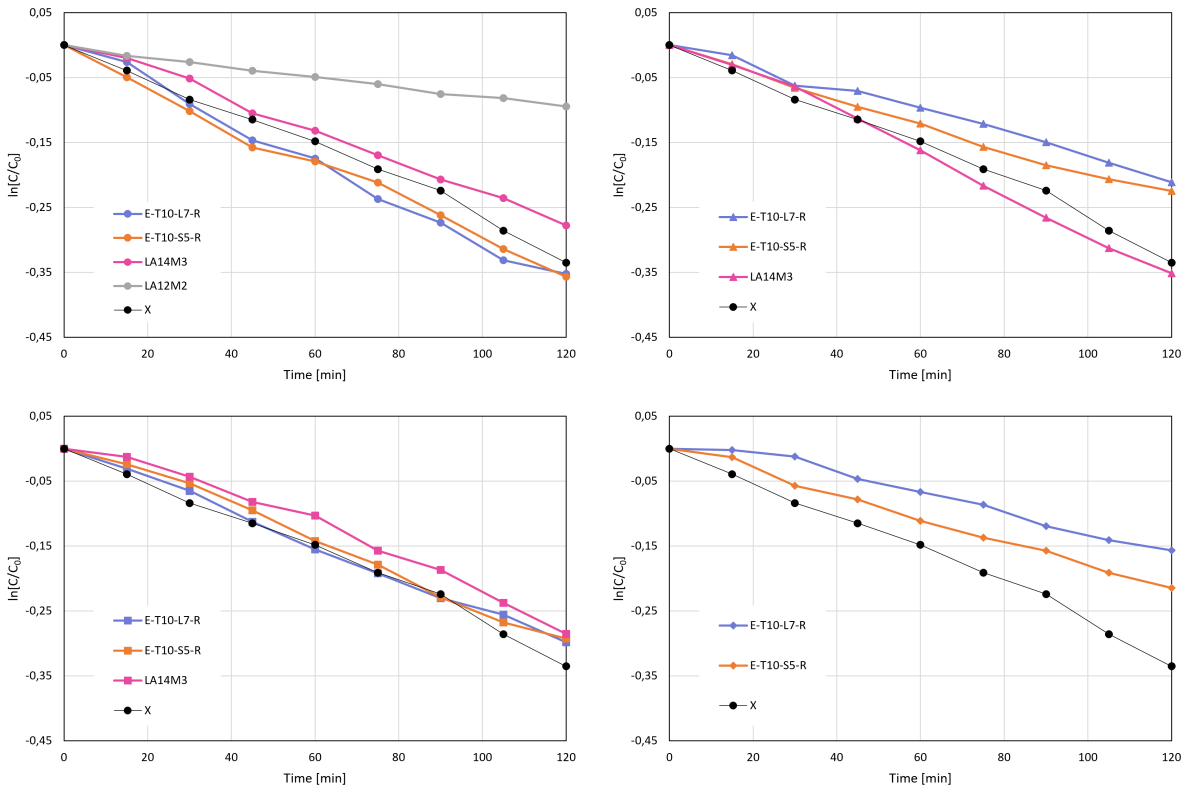

Figure 3.22: Results comparison of UV-VIS photocatalysis for ethanol based sol-gels. Each plot compares the results obtained at the same amount of ageing time, namely 2 (top left), 4 (top right), 6 (bottom left), 8 (bottom right) weeks.

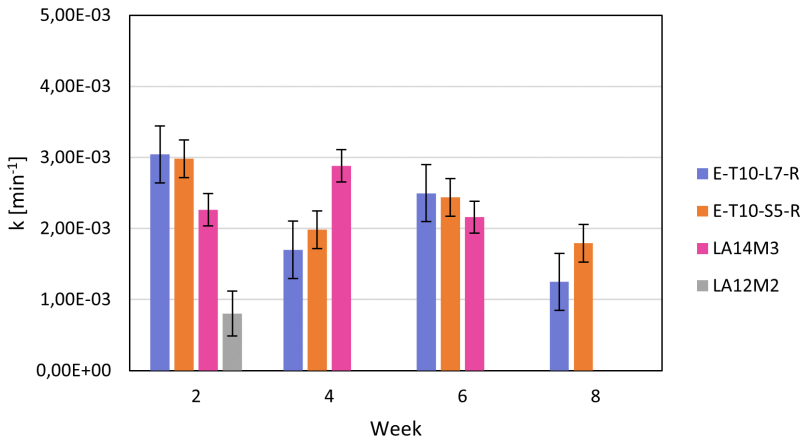

Figure 3.23: Results comparison between the obtained kinetic constants k for the ethanol based sol-gels at 2, 4, 6, 8 weeks.

The obtained kinetic constants showed an overall average level of photoactivity. The highest one was reached by sample E-T10-L7-R after 2 weeks, quickly followed by E-T10-S5-R, again, at its 2nd week. The two mentioned sol-gels maintained good stability and homogeneity across the testing period, this could be seen also from the low drop in photocatalytic activity during the 4th week. The effect of the surfactants could be considered positive as, even if the amount of solvent was lower compared with sol-gels made in previous studies, there was no precipitation or strong gelation during the 8 weeks of testing. On the other hand, the higher sol-gel concentration in titanium dioxide precursor did not result in equivalently high photoactivity. The expected limitation connected to the usage of this solvent were proven true even in the presence of surfactants. The relatively high polarity of ethanol, combined with the efficient particle-spacing induced by the surfactants, made it possible for the sol-gels to keep their stability while the condensation reaction was going on. Moreover, the reduction of surfactant amount with respect to the isopropanol-based formulations, turned out to be a good chioce.

Sol-gel LA12M2 was tested just at the 2nd week due to the precipitation event; indeed, its photocatalytic activity was really low, meaning that the sol-gel was impoverished in TiO_2. The reproduction of this sol-gel, LA14M3, showed a medium level of photoactivity which did not vary considerably across the 6 weeks period. This sol-gel, in accordance to the literature, was readily photoactive and did not show many drops in photoactivity. On the 4th week it even reached its highest peak. This level of photoactivity was also close in value as the completely aged version of this sol-gel, the sample "X". This proved that the solution kept its medium photoactivity for a long period of time alongside its homogeneity and stability.

Even though ethanol-based sol-gels have not excelled in terms of photocatalytic activity, they

showed a positive trend in terms of long term stability under normal environmental conditions. Another positive aspect lied in the aesthetic appearance of the dip coated samples. The final product was, in fact, mirror-like and macroscopically smooth (Figure 3.24).

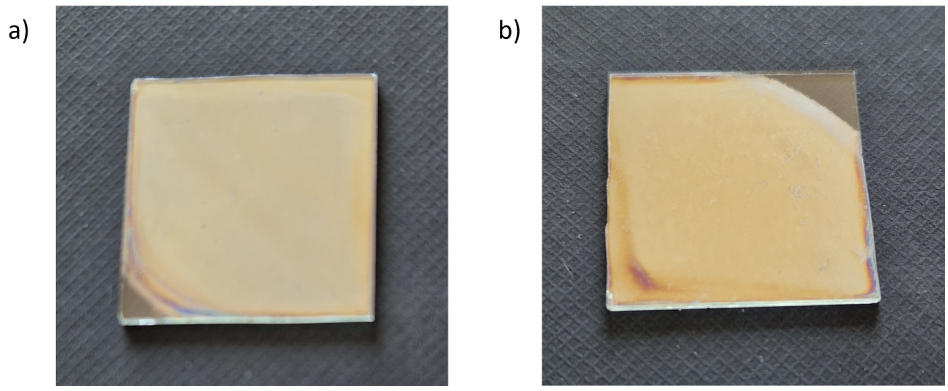

Figure 3.24: Aesthetic appearance of samples LA14M3 (a) and E-T10-L7-R (b).

Further investigation regarding the surface morphology of the deposited samples was performed to better understand the relationship with the final photocatalytic activity and to identify the effects generated by adding surfactant molecules in the formulation.

3.4.3. Ultrasonicated sol-gels

Two organic solvent based sol-gel formulations were remade and subjected to a series of ultrasonication steps. This procedure was used to test the effect of a temperature increase in the reaction batch combined with a constant stirring caused by the ultrasonic waves propagating in the sols. The ultrasonication step lasted 2 hours and the temperature increase was monitored with thermometers inserted both in the sol-gels and in the ultrasonic bath. The temperature was read every 20 minutes and the obtained results are reported in Table 3.3.

Table 3.3: Temperature increase monitored during the 2 hours ultrasonication procedure.

Time [min]	Ultrasonic Bath T [°C]	Sol-gel T [°C]	
		I-T12-L20-N-U	E-T10-L7-R-U
0	19	19	18
20	27	34	33
40	35	40	40
60	41	46	46
80	46	51	51
100	50	54	54
120	51	54	54

The ultrasonication procedure was repeated 4 times across 4 weeks of ageing (1 every week) and the two sol-gels were deposited each time and tested with the UV-VIS photocatalysis. The obtained kinetic constants k are shown in Figure 3.25, compared with the ones of the former, non-ultrasonicated, sol-gels. The results for the ultrasonicated ones are reported every week, while the others, every two weeks.

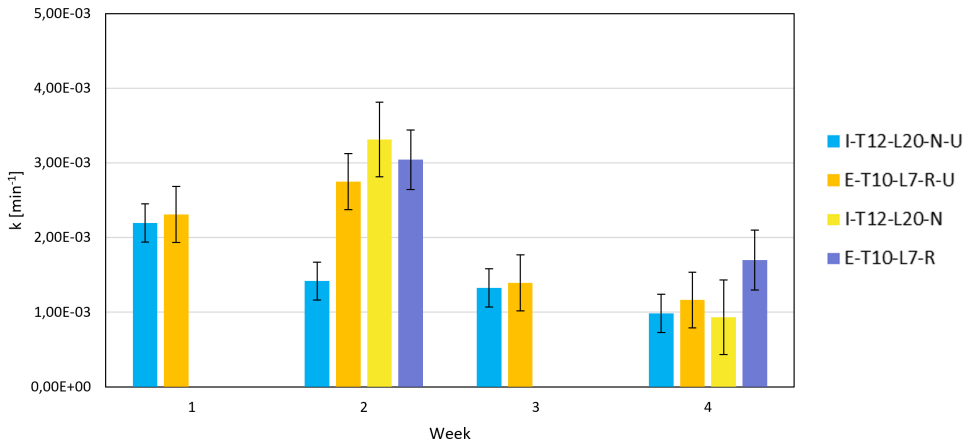

Figure 3.25: Results comparison between the obtained kinetic constants k for the ultrasonicated sol-gels at 1, 2, 3, 4 weeks and the ones obtained for the non-ultrasonicated versions at 2, and 4 weeks, tested with UV-VIS photocatalysis.

These results showed the ineffectiveness of the ultrasonication step. The temperature-enhanced ageing led to lower photoactive products almost everytime, compared to the natural aged samples. The only positive result was obtained by sol-gel E-T10-L7-R-U at the second week of

ultrasonication but afterwards the photocatalytic activity dropped to really low values. The test led to the conclusion that, despite the increased temperature and the homogenization induced by the ultrasonic waves, the accelerated ageing was not beneficial for the final photocatalytic properties, wanted for the aim of this work.

3.4.4. Water-based sol-gels

Water-based sol-gels were the most studied across this work for two main reasons:

- in previous works it has been demonstrated that water-based sol-gels were the ones producing the best results in terms of photoactivity. The starting point formulation was capable of reducing almost completely the RhB (10^{-5} M) solution during the six hours photocatalysis. The biggest drawbacks linked to the usage of water were the premature gelation of the sol and the poor homogeneity of the deposited film, even for the best performing samples. The introduction of surfactants and templating agents was identified to be a possible solution for these issues;
- water is a completely green solvent, cheap and readily available to be used. Moreover, the available and tested surfactants have higher solubility in water with respect to the previously discussed organic solvents. Also nanocellulose, despite its insolubility, shows high affinity with water and it is easy to disperse in it.

Almost all the water-based sol-gels were prepared using the established molar ratio of 1:100:5 between TTIP, distilled water, and acetic acid or increasing the amount of TTIP by 20%, having a ratio of 1.2:100:5. There were few cases in which the solvent relative molar amount was reduced to 75 or the relative molar amount of TTIP was pushed up to 1.5. The type of surfactant or nanocellulose was varied between different formulations as well as their amount inside the formulation. All the results concerning the prepared formulations will be reported in the following sections. The discussion will be divided in three parts: surfactant-based sol-gels, cellulose nanofibers based sol-gels, and cellulose nanocrystals based sol-gels.

Prior to this discussion, it is important to report the results of sol-gel W-T10-R-I. This sample was the reproduction of the formulation found to be highly photoactive in previous thesis works [87, 95]. This sol-gel was prepared through the reverse addition method and using the basic molar ratio of 1:100:5 between TTIP, distilled water, and acetic acid. This sol-gel was reported to reach a high level of photocatalytic activity after 6-7 weeks; in this work, it was tested, as every other sample, every two weeks for six weeks total, in order to compare its evolution with the one of other water-based sol-gels and highlight the main advantages or disadvantages of adding surfactants or nanocellulose to the formulation. Below, the results obtained for sample W-T10-

R-I concerning the UV-VIS photocatalytic test (Figure 3.26) and the correspondent values of the kinetic constant for the RhB ($5 \cdot 10^{-6}$ M) degradation reaction (Figure 3.27) are reported.

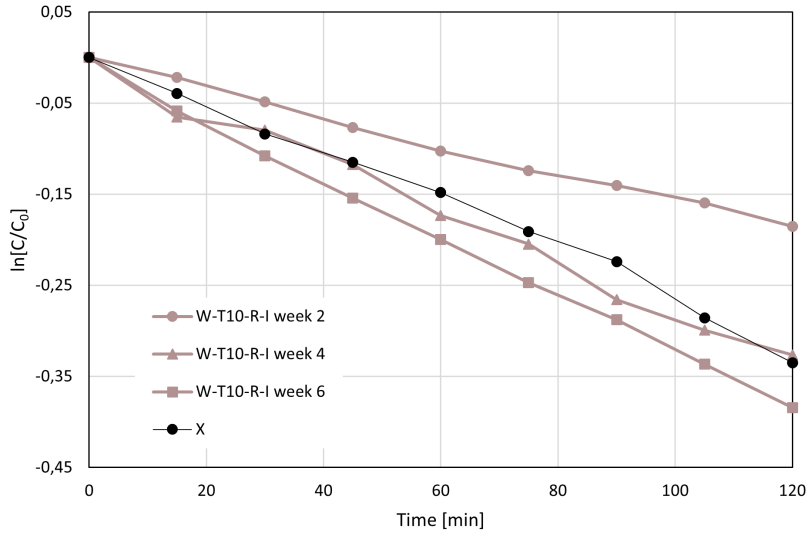

Figure 3.26: Results of UV-VIS photocatalytic test of sol-gel W-T10-R-I at 2, 4, 6 weeks.

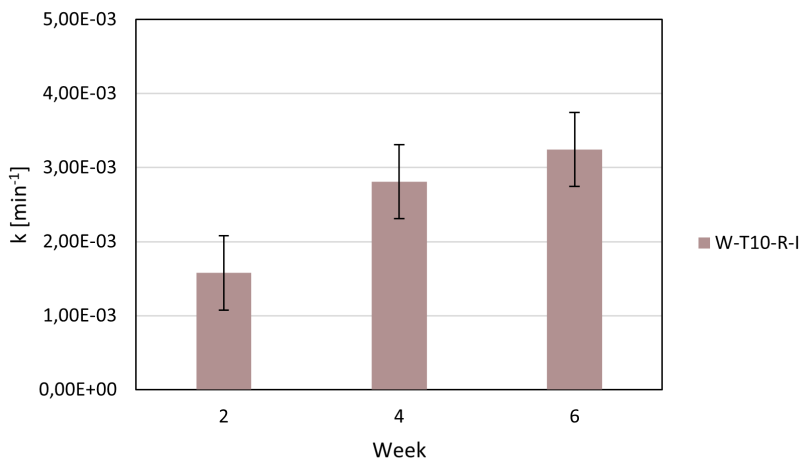

Figure 3.27: UV-VIS obtained kinetic constants k for sol-gel W-T10-R-I at 2, 4, 6 weeks.

Surfactant-based sol-gels

As previously mentioned, water-based sol-gels suffer from poor surface homogeneity, hence aesthetic appearance, when deposited onto the glass substrates alongside with possible premature gelation. Lutensol ON70 and Ecosurf eh-3 were chosen as surfactants in the formulation of water-based sol-gels because they were the more soluble ones. SDS was not included in the experiments as it is the more harmful in terms of environmental danger. Moreover, based on

preliminary formulations tests, SDS and water based sol-gels, made using the same amount of surfactant as the isopropanol-based ones mentioned in the previous section, had the tendency to solidify rather quickly, becoming unusable for dip-coating deposition.

Two main water and surfactant based formulations have been prepared: W-T12-L20-N, using Lutensol ON70 and W-T12-E5-N, using Ecosurf eh-3. In both cases, TTIP was added last, following the normal addition method. The relative molar amount of TTIP was also 20% higher than the base formulation; this was done to test right away if there were any improvements in sol stability at higher precursor content by the addition of surfactants. This increase in the precursor was immediately reflected in the aesthetic appearance of the sol-gels, indeed, they were white in colour with a milky appearance. These sols were initially stable and did not show signs of gelation. As ageing progressed, little gelation could be noted at the bottom of the beaker containing sol-gel W-T12-E5-N. This was, however, easy to re-disperse via sonication prior to dip-coating deposition, granting a good homogeneity of the sol. After a single sonication step, the sol-gel was again homogeneous and stayed stable across the 6 weeks testing time.

The UV-VIS photocatalytic degradation test results concerning these first two sol-gels are reported below in Figure 3.28, while the kinetic constants k are shown in Figure 3.29. Also in this case, sample "X" is shown for comparison purposes.

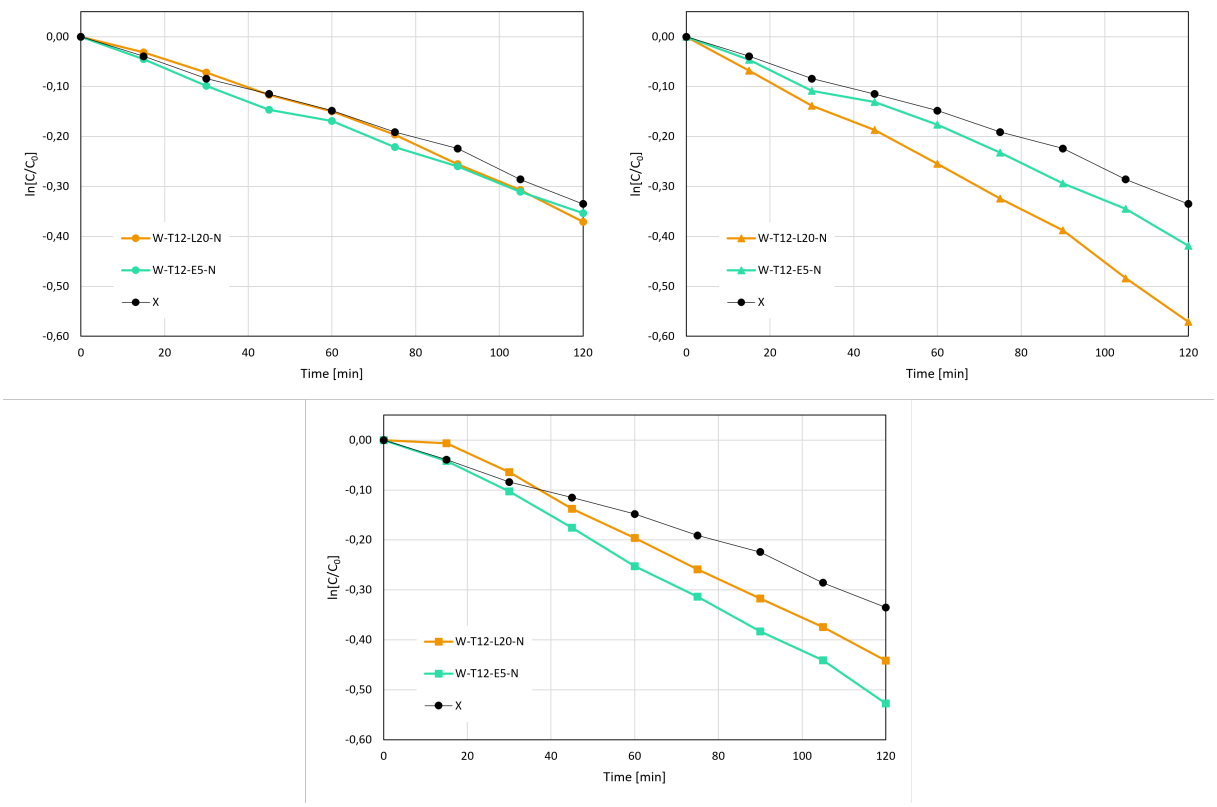

Figure 3.28: Results comparison of UV-VIS photocatalysis for the first water and surfactant based sol-gels. Each plot compares the results obtained at the same amount of ageing time, namely 2 (top left), 4 (top right), 6 (bottom) weeks.

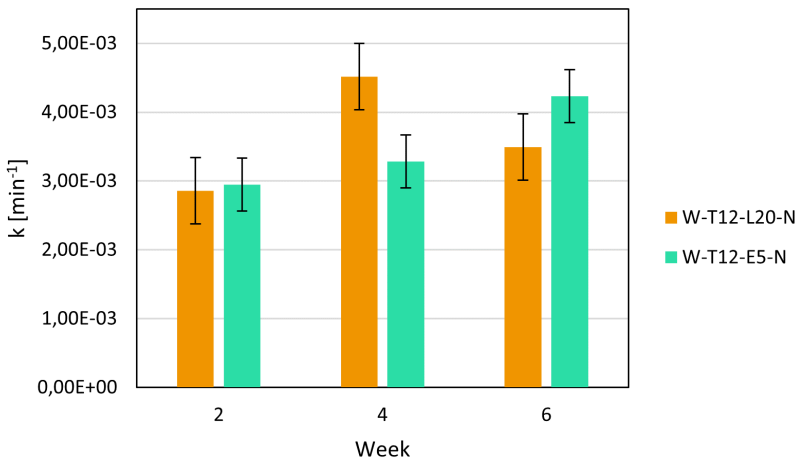

Figure 3.29: Results comparison between the obtained kinetic constants k for the first water and surfactant based sol-gels at 2, 4, 6 weeks, tested with UV-VIS photocatalysis.

These two sol-gels showed the highest photocatalytic activity among all the tested samples so

far. In particular, sol-gel W-T12-L20-N reached its peak performance at 4 weeks while W-T12-E5-N at 6 weeks. From the first screening step, these samples looked very promising and were then tested with the UV-LED photocatalytic degradation test to have results directly comparable with the ones obtained in previous works. These results are reported below in Figure 3.30, and are present here to contextualize the following experimental steps.

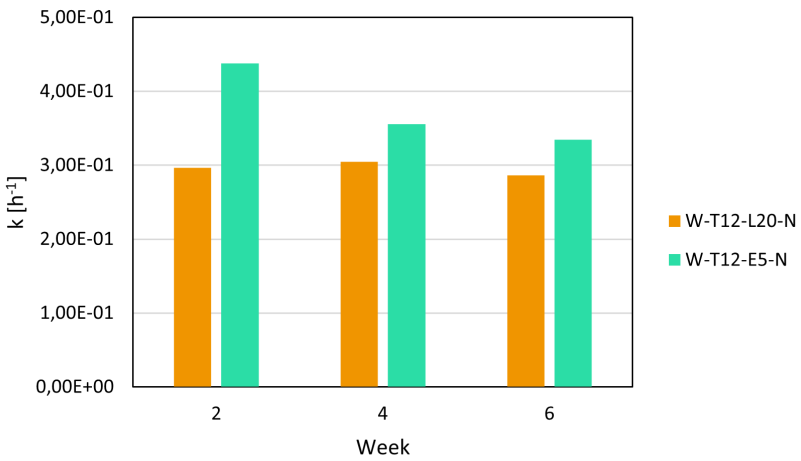

Figure 3.30: Results comparison between the obtained kinetic constants k for sol-gels W-T12-L20-N and W-T12-E5-N at 2, 4, 6 weeks, tested with UV-LED photocatalysis.

From these results it was possible to observe that samples W-T12-L20-N and W-T12-E5-N were in fact highly photoactive, in particular, sol-gel W-T12-E5-N showed a really high peak of photoactivity after just 2 weeks. This behaviour showed that the UV-VIS screening procedure was great for spotting high performance samples but it showed also that different samples obtained from the same aged sol-gel may show slightly diverse photocatalytic activity levels in different tests. This last point is strongly connected to the surface morphology and composition of the final deposited sample, as the starting solution is the same. For these reasons, it was important to perform further analyses on the final samples and they will be presented later in this work to conclude the discussion.

From the UV-LED test, W-T12-E5-N was identified as one of the best obtained sol-gels since it not only reached a very high k value but also it took just 2 weeks to show its peak performance. This formulation was a promising improvement from the base one, which reached such photoactivity in longer times.

To check the repeatability of this formulation, two identical sol-gels, namely W-T12-E5-N-V1 and W-T12-E5-N-V2, were prepared following the same procedure as W-T12-E5-N. This time also the temperature and relative humidity were tracked in order to characterize the sol-

gel in the most complete way possible. In addition to these new formulations, also sol-gel W-T15-E5-N was prepared, in this case increasing the amount of TTIP by 50% with respect to the base formulation. This was done to check the stability of the sol with a high amount of precursor. These sol-gels had a different aesthetic appearance as they were semi-transparent and not completely white. The same gelation effect at the bottom of the reaction beaker was present after the first week. Again, after a single sonication step, performed before the first deposition, it was possible to obtain a long-term stability and homogeneity of the sol-gel. The results of the UV-VIS photocatalysis for these new sol-gels are reported below, where they are put in comparison with the former formulation W-T12-E5-N (Figure 3.31 and Figure 3.32).

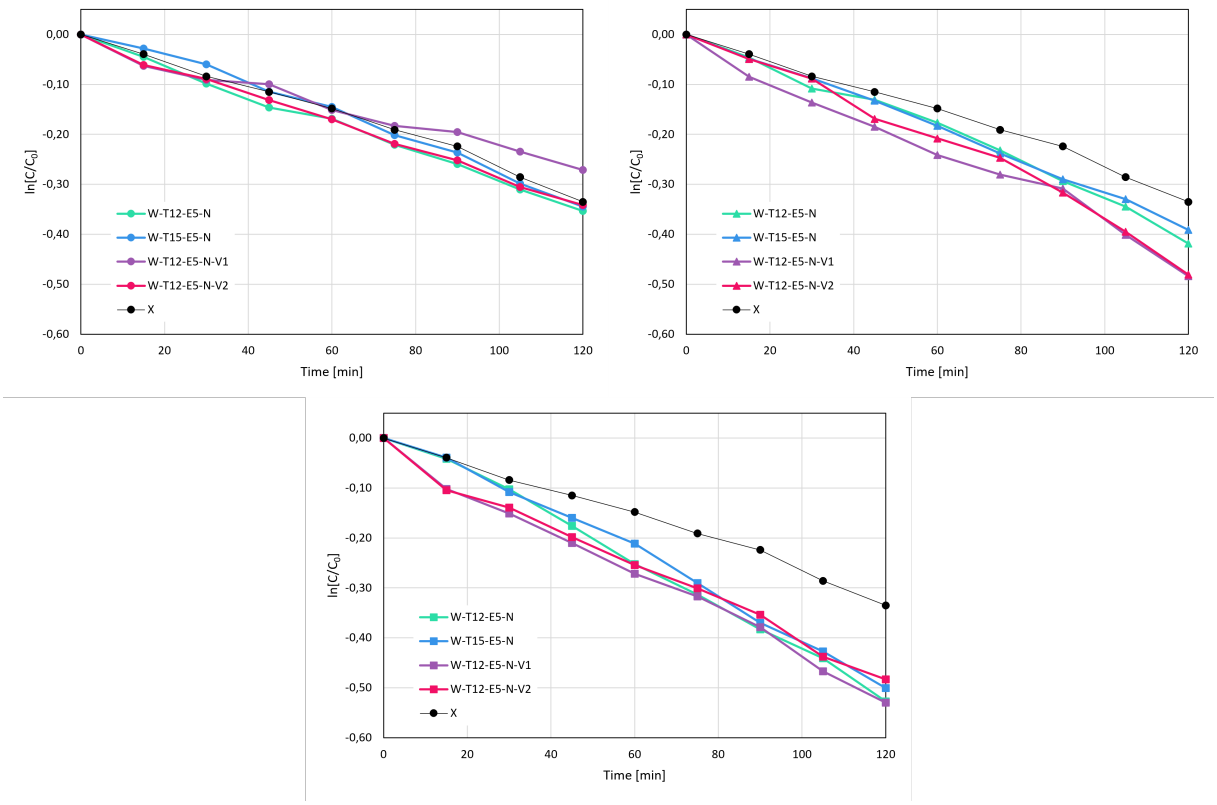

Figure 3.31: Results comparison of UV-VIS photocatalysis for the new and repeated water and Ecosurf eh-3 based sol-gels. Each plot compares the results obtained at the same amount of ageing time, namely 2 (top left), 4 (top right), 6 (bottom) weeks.

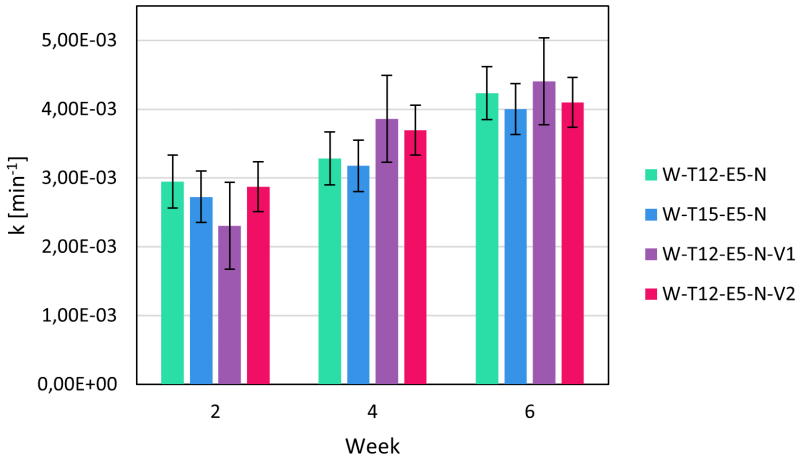

Figure 3.32: Results comparison between the obtained kinetic constants k for the new and repeated water and Ecosurf eh-3 based sol-gels at 2, 4, 6 weeks, tested with UV-VIS photocatalysis.

From these results, it could be seen that all the prepared sol-gels showed a high and increasing level of photoactivity across the 6 weeks period. The trend was similar to the former formulation, W-T12-E5-N, except for sample W-T12-E5-N-V1 that during the first 2 weeks showed a quite lower k value. This was probably due to the sol-gel reaction involving the intermediate metal alkoxide oligomers not being fully completed. During the calcination step, in fact, the dip-coated samples presented some burned spots on the surface, indicating either an entrapment of a contaminant organic species or, more probably, the burning of the non fully reacted titanium alkoxide oligomers accumulated in specific spots of the coated glass surface. After ageing, however, the sol-gel developed its properties correctly, reaching even the highest obtained k value after 6 weeks. Sol-gel W-T15-E5-N, despite the increased precursor amount, did not show significantly higher photoactivity. This could be ascribed to lower homogeneity inside the sol which may lead to non-optimal final morphologies in the coated samples. This aspect was in need of better clarification and will be addressed in the section dedicated to the samples characterization.

Overall, the water and surfactant based sol-gels showed really high and promising levels of photocatalytic activity, both during the UV-VIS tests and the UV-LED ones. The latter will be discussed more specifically further in this work. The introduction of surfactants such as Lutensol ON70 and Ecosurf eh-3 granted the sol-gels a good long term stability even at higher contents of precursor. In particular, the ones using Ecosurf eh-3 looked the most promising from point of view of reaching very high levels of photocatalytic activity in short periods of time and for the fact that this surfactant is among the cleanest and "greenest" products to be

used in sol-gel technology.

Ecosurf eh-3 based samples, however, did not solve the issue connected to the aesthetic appearance of water-based sol-gels. Indeed, all the coated samples showed uneven patterns on the surface and they were also opaque in the spots where the coating contained more TiO_2. On the other hand, sol-gel W-T12-L20-N combined good photoactivity with a perfect aesthetic appearance. The produced samples were, in fact, almost completely transparent. The appearance comparison between the aforementioned samples is shown in Figure 3.33.

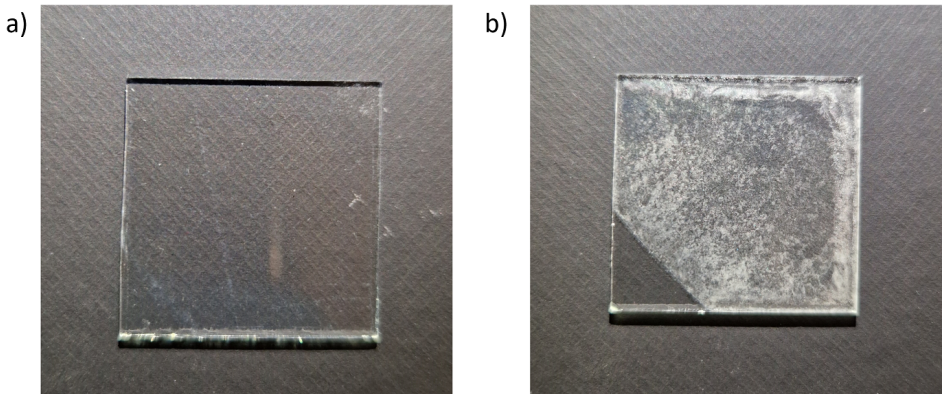

Figure 3.33: Aesthetic appearance of samples W-T12-L20-N (a) and W-T12-E5-N (b).

Cellulose nanofibers based sol-gels

Water and CNF based sol-gels had all been prepared using the 3% slurry purchased from Maine University. Prior to the formulation of these sol-gels, different dilutions were tested to check the dispersibility of such nanofibers in distilled water. The one that showed a good compromise between CNF content and suspension homogeneity was identified to be the 1:200 wt. dilution, where 1 was the relative amount of slurry and 200 the relative amount of distilled water. This was the starting point and then other dilution were prepared to test the effect of increasing amounts of CNF on the stability and photoactivity of the prepared sol-gels.

CNF-based sol-gels were all prepared following the reverse addition method in order to focus on the effect of the nanocellulose itself by fixing this parameter. The initial prepared formulations were sol-gels W-T10-F200-R and W-T12-F200-R, for which the 1:200 wt. dilution was used. Sample W-T12-F200-R had also 20% more TTIP than W-T10-F200-R. After these first ones, six new formulations were prepared by, first, changing the dilution level to 1:50, 1:100, and 1:300 wt. and then also reducing the quantity of solvent to a relative molar amount of 75 instead of 100. The amount of TTIP was kept fixed to not introduce many variables in the experiments. The results of the UV-VIS photocatalytic degradation tests concerning the first five samples are reported in Figure 3.34, and their correspondent k values in Figure 3.35.

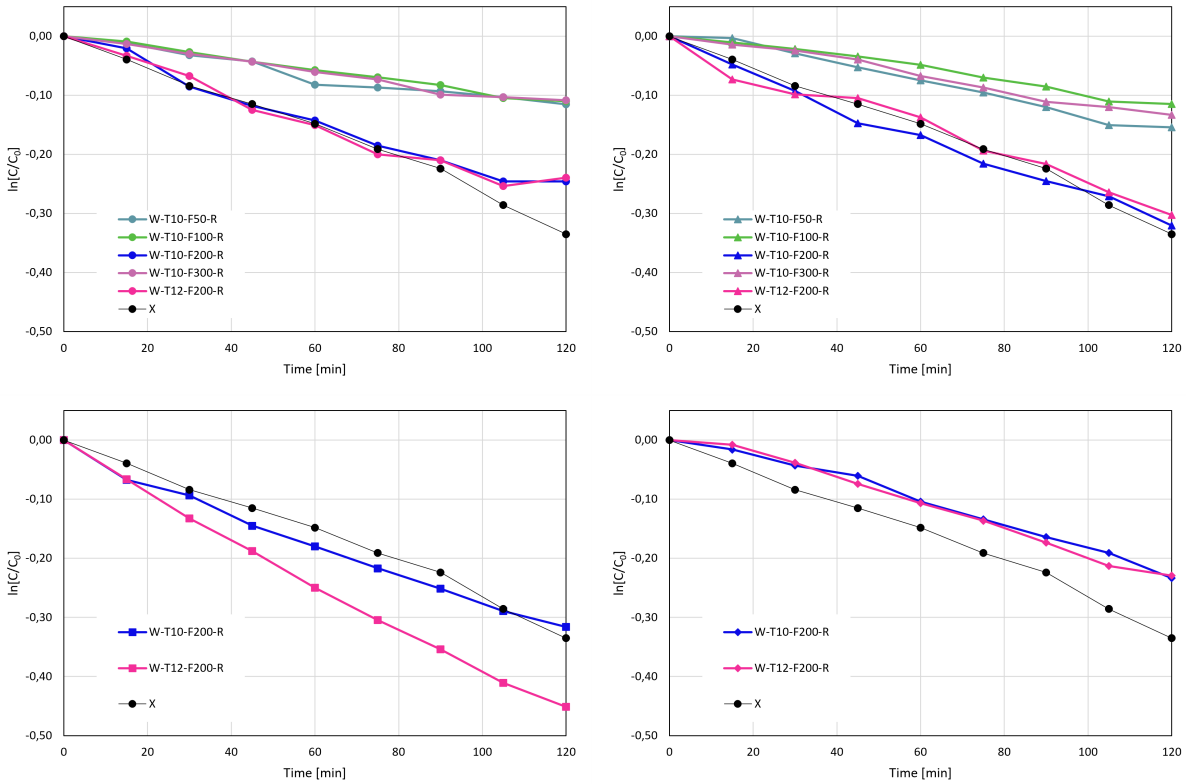

Figure 3.34: Results comparison of UV-VIS photocatalysis for water and CNF based sol-gels. Each plot compares the results obtained at the same amount of ageing time, namely 2 (top left), 4 (top right), 6 (bottom left), 8 (bottom right) weeks.

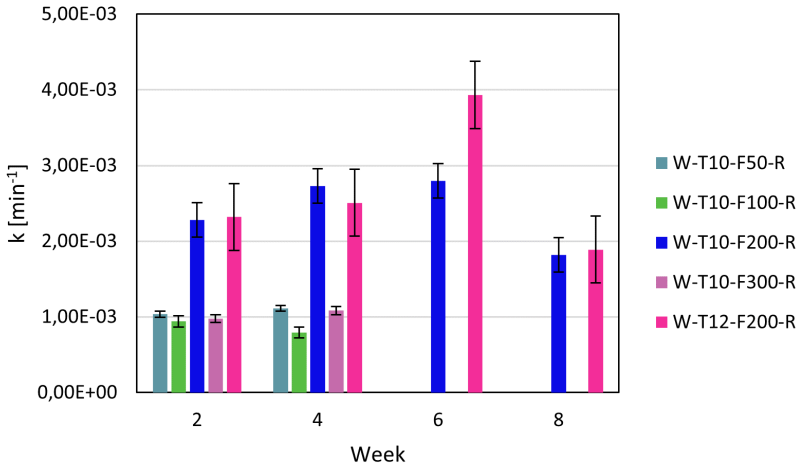

Figure 3.35: Results comparison between the obtained kinetic constants *k* for the water and CNF based sol-gels at 2, 4, 6, 8 weeks.

It can be seen from the plots that the data at 6 and 8 weeks for samples W-T10-F50-R, W-T10-

F100-R, and W-T10-F300-R is missing. Their results during the first 4 weeks were much worse than sol-gels W-T10-F200-R and W-T12-F200-R. This could be ascribed to the macroscopic behaviour of the sol-gel, in fact, some agglomeration could be seen in the bulk of the solution; this probably led to the segregation of the TiO_2 network, overall depleting the sol from the photocatalyst. Upon deposition, this could be reflected in a titanium dioxide-poor final product, which, ultimately, showed really low photoactivity. The segregation inside the sol-gels, in particular the more CNF-concentrated ones, emerged after the sonication step performed prior to dip-coating deposition. Another issue related to these samples was the appearance of burned spots after the calcination step for samples W-T10-F50-R and W-T10-F100-R during week 4. A less harsh calcination step was tried, to find a possible solution to the problem. The heat treatment was performed at 100°C, but, even if the samples were not burned, the photocatalysis results did not show any notable improvement, indeed, a problem of surface detachment was encountered. All these issues led to the discontinuation of the photocatalytic tests for such sol-gels. To precisely explain the reasons behind the failure of the aforementioned samples, specific analysis on the sol-gel would be needed, and this was out of the scope of this work. The same issues were encountered with the more concentrated formulations W75-T10-F50-R, W75-T10-F100-R, and W75-T10-F300-R, where the amount of solvent was reduced instead of increasing the precursor amount. The results after 2 weeks, combined with the burning of the samples after the thermal treatment led to the discontinuation of the tests also in this case. This results are reported in Figure 3.36, where the k values are compared to sample W-T10-F50-R during week 2.

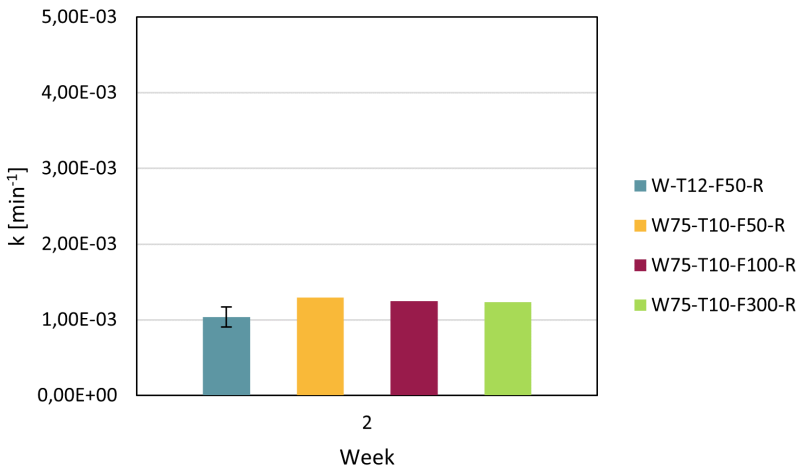

Figure 3.36: Results comparison between the obtained kinetic constants k for the CNF based sol-gels formulated with a lower amount of solvent and sol-gel W-T10-F50-R at 2 weeks.

Going back to the previous discussion, sol-gels W-T10-F200-R and W-T12-F200-R showed

overall an average level of photoactivity, except during week 6, when the latter reached higher photocatalytic activity. This could be connected to the increased amount of TTIP used for its formulation. Overall, sol-gels W-T10-F200-R and W-T12-F200-R performed well during the 8 weeks ageing as no agglomeration or instability was present in these solutions. For the aforementioned reasons, the optimal CNF dilution was identified to be 1:200 wt.

Due to the promising nature of the nanocellulose-mediated synthesis of TiO_2 sol-gels, four formulations were prepared again in another batch. These new sol-gels were W-T10-F100-R-V1, W-T10-F300-R-V1, W-T10-F200-R-V1, and W-T12-F200-R-V1, the last one being the more promising one, given the good results obtained during week 6 of UV-VIS photocatalysis of sample W-T12-F200-R. These new sol-gels were prepared using a more precise instrument to weight the slurry used for the dilution preparation. Moreover, the sonication step, that usually concluded the synthesis procedure, was not performed, in order to avoid the formation of agglomerates in the bulk of the sol. These precautions led to more stable and homogeneous sol-gels across the 6 weeks of testing. The UV-VIS photocatalysis results concerning these samples are reported below in Figure 3.37, and the kinetic constants for the RhB degradation reaction are shown in Figure 3.38.

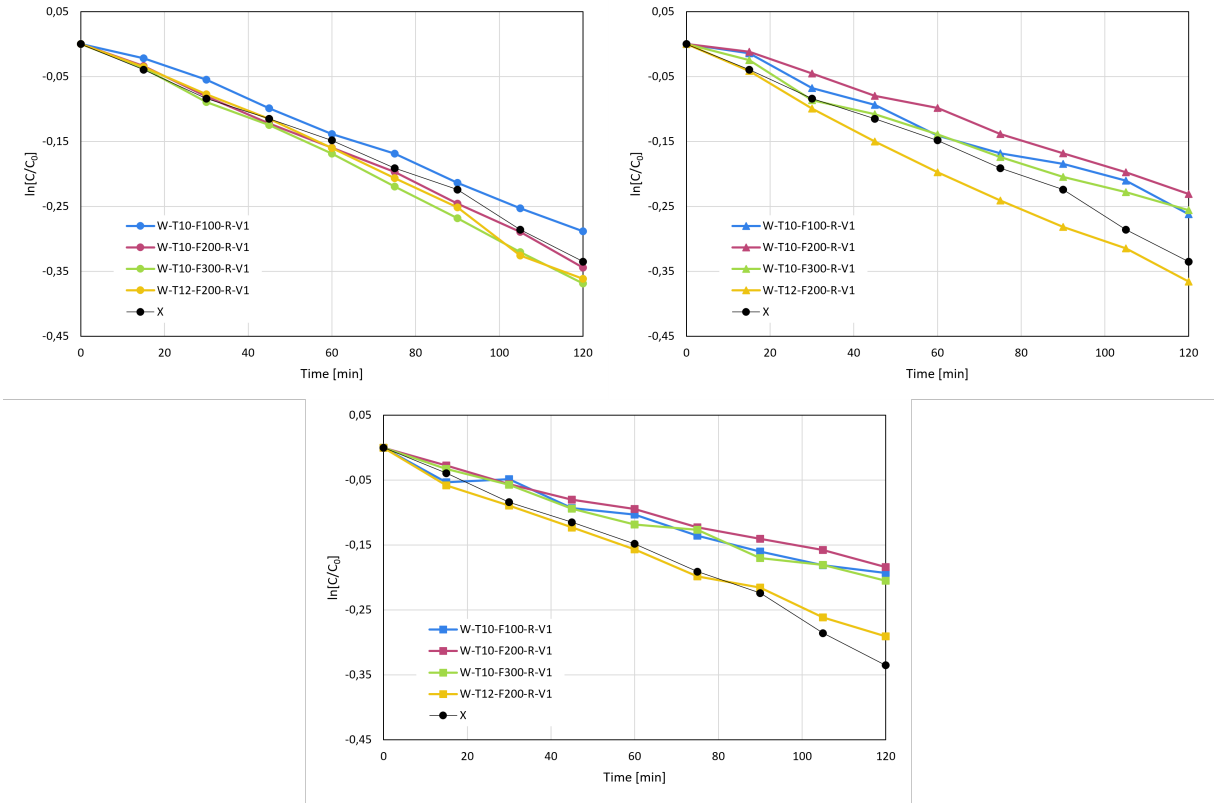

Figure 3.37: Results comparison of UV-VIS photocatalysis for water and CNF based sol-gels. Each plot compares the results obtained at the same amount of ageing time, namely 2 (top left), 4 (top right), 6 (bottom) weeks.

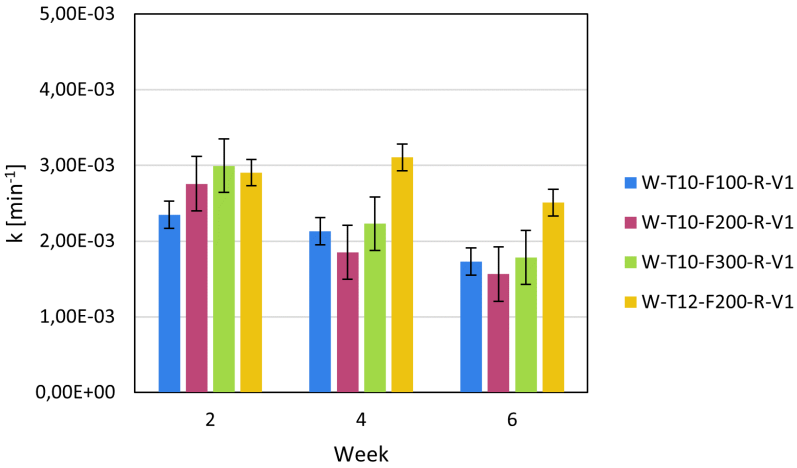

Figure 3.38: Results comparison between the obtained kinetic constants *k* for the water and CNF based sol-gels at 2, 4, 6 weeks.

These results showed an improvement for what concerns sol-gels W-T10-F100-R-V1 and W-

T10-F300-R-V1, reproductions of the more problematic samples, while sol-gels W-T10-F200-R-V1 and W-T12-F200-R-V1 gave slightly different results than before. A notable differences was the missing high peak of photoactivity at week 6 for sample W-T12-F200-R-V1. This could be ascribed to the fact that week 6 W-T12-F200-R may have been subject to an anomaly in the previous deposition, since the behaviour of the two similar samples was quite homogeneous. Another difference was in sample W-T10-F200-R-V1, which was less stable and started dropping its photocatalytic activity just after 4 weeks.

From the first screening step, CNF-based sol-gels did not show any significant improvement with respect to the former formulation W-T10-R-I. Only sample W-T12-F200-R reached a good level of photoactivity and was then subjected to further investigation. The results of the latter will be presented further in this work, where the UV-LED analysis and the samples characterization will be addressed.

As a final note, these sol-gels did not show perfect homogeneous surface appearance, keeping the same flaw of most water-based coatings. Examples of water and CNF based thin films are illustrated in Figure 3.39, including sample W-T12-F200-R when it achieved its best results.

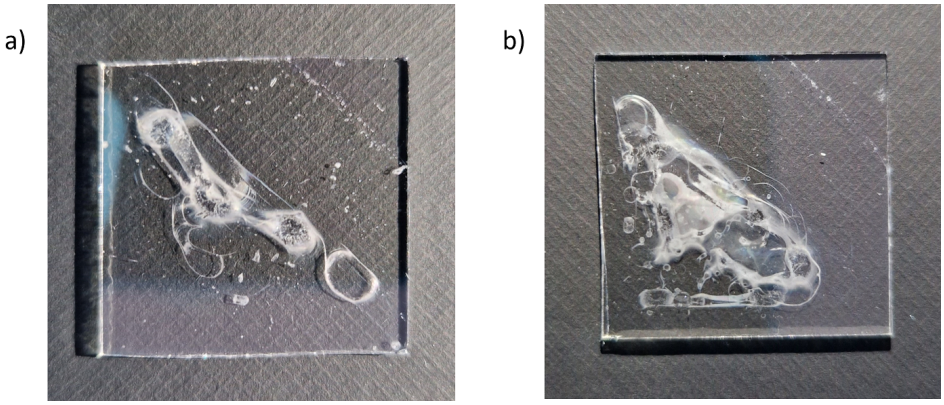

Figure 3.39: Aesthetic appearance of samples W-T10-F200-R (a) and W-T12-F200-R (b).

Cellulose nanocrystals based sol-gels

The last tested material for the formulation of novel titanium dioxide sol-gels was the CNC synthesized via acid hydrolysis. All the characteristics of this reagent were presented in section 3.1. The CNC-based sol-gels were prepared in two different batches. The first one included samples W-T10-C200-R, W-T10-C150-R, W-T10-C150-R-I, and W-T12-C150-R-I. These sol-gels were wrongly formulated with a high amount of solid inside the water suspension. This quickly led to a strong gelation effect that did not allow any deposition step to be performed.

A second batch of samples was then prepared, including sol-gels W-T10-C6-R, W-T10-C3-R, W-T10-C3-R-I, and W-T12-C3-R-I. These sol-gels were formulated analogously to the CNF-

based ones, as now the amount of solid present in the water suspension was comparable to the solid amount present in CNF dilutions. This was done to directly compare the two types of nanocellulose materials. It must be noted, however, that the solid present in the CNC suspension was composed by an unknown amount of cellulose nanocrystals and $NaSO_4$. These formulations were prepared to check if the latter could have any beneficial effect on the properties of the sol-gel. In literature it is in fact reported that sulfate ions can enhance the photocatalytic activity of TiO_2, in particular, they could improve the light harvesting capabilities of titanium dioxide [96]. On the other hand, TiO_2 with incorporated sulfate ions could show limited levels of photoactivity while being more stable in terms of adhesion with the coated substrate as stated in other articles [97]. Since the effect of sulfates in the formulation of titanium dioxide sol-gels was unknown, to test it, the previously mentioned samples were prepared without performing a purification step on the CNC suspension. A repetition of the last four formulations was then performed. Sol-gels W-T10-C6-R-V1, W-T10-C3-R-V1, W-T10-C3-R-I-V1, and W-T12-C3-R-I-V1 were so created. These sol-gels were all prepared following the reverse addition method and varying the dilution level of the solvent suspension. Another difference in the preparation of such sol-gels was the last step of homogenization of the solution, performed either via the usual 1 hour stirring or with a shorter 15 minutes stirring followed by a 1 hour sonication using ice to control the temperature of the reaction. Samples prepared with the latter technique were indicated with the letter "I".

The photocatalysis tests results concerning CNC-based sol-gel are reported in Figure 3.40, while the kinetic constants values are shown in Figure 3.41.

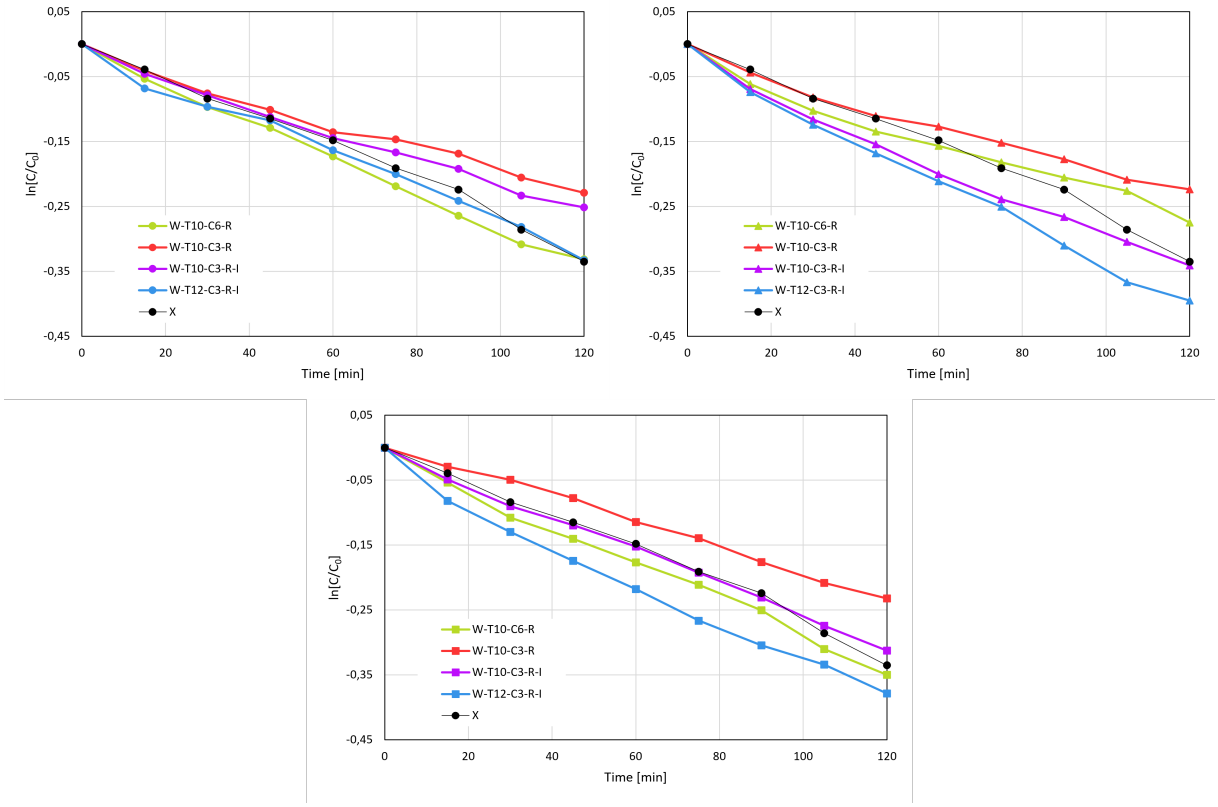

(a) First batch of tested CNC-based sol-gels results.

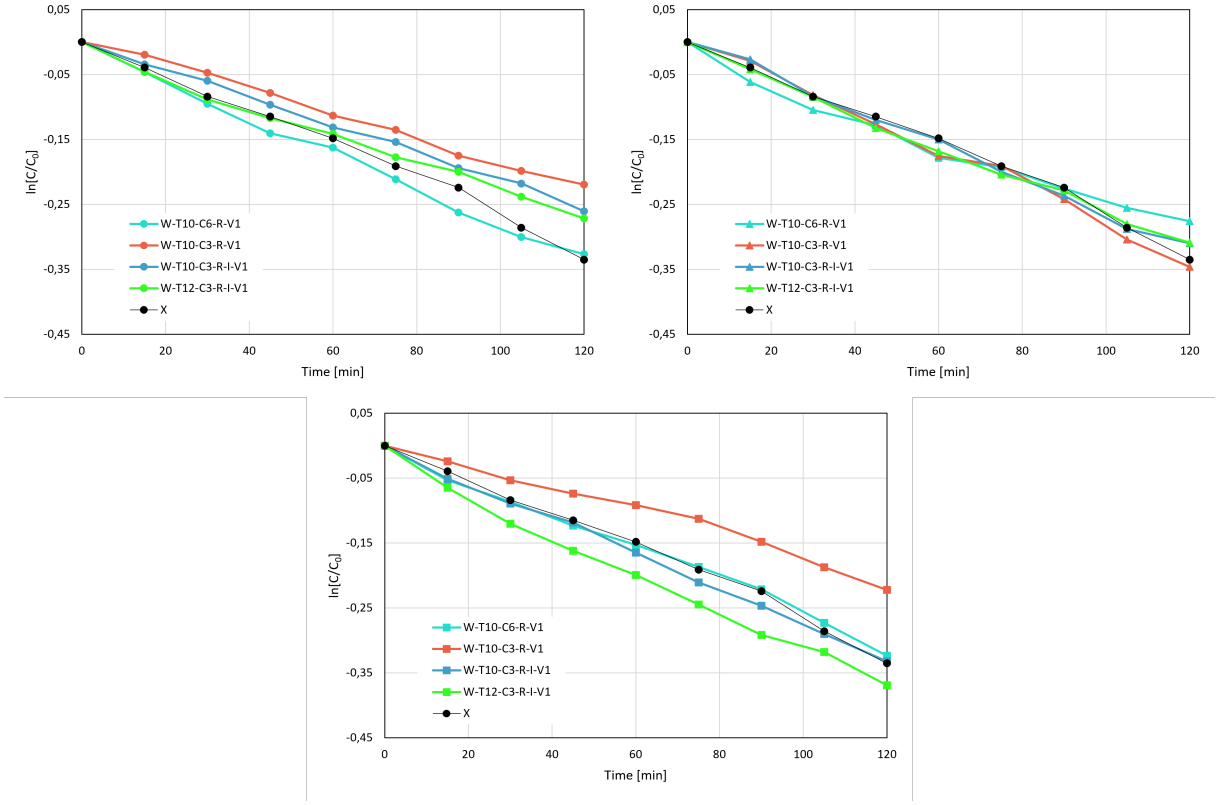

(b) Second batch of repeated CNC-based sol-gel formulations results.

Figure 3.40: Results comparison of UV-VIS photocatalysis for water and CNC based sol-gels. Each plot compares the results obtained at the same amount of ageing time, namely 2 (top left), 4 (top right), 6 (bottom) weeks.

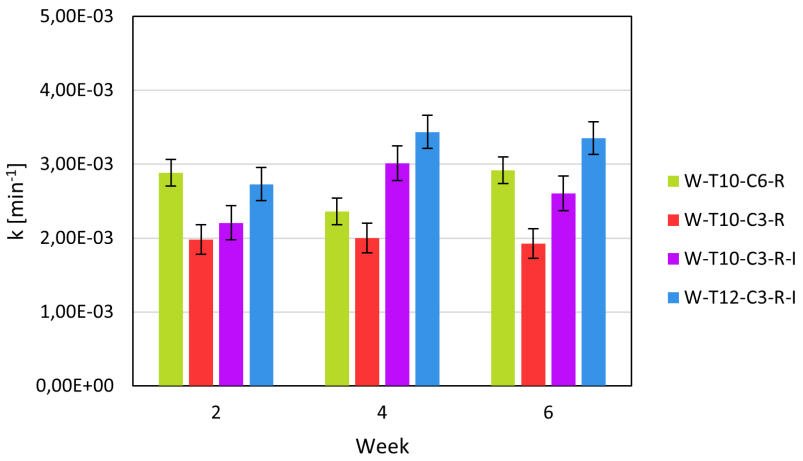

(a) First batch of tested CNC-based sol-gels results.

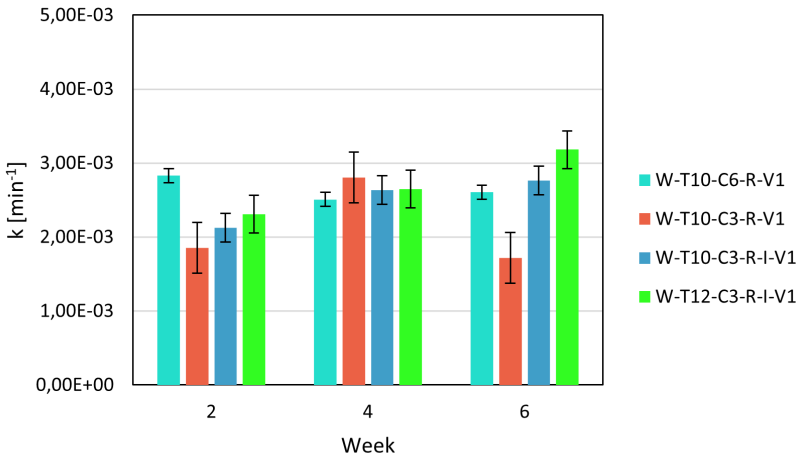

(b) Second batch of repeated CNC-based sol-gel formulations results.

Figure 3.41: Results comparison between the obtained kinetic constants k for the water and CNC based sol-gels at 2, 4, 6 weeks.

From these results, it was possibile to see that the CNC-based sol-gels showed a medium level of photocatalytic activity. Only sample W-T12-C3-R-I and its repetition W-T12-C3-R-I-V1 reached a k value higher than $3{\cdot}10^{-3}$ min^{-1}, in particular during week 4 and 6 for the former, and week 6 for the latter. These results were promising since CNC-based sol-gels showed also a very high stability during the testing time. Opposite to the first unsuccessful batch, these last 8 formulations never had impurities or inhomogeneities and the appearance of the sols during ageing was comparable with the one of the former solution W-T10-R-I. Samples W-T12-C3-R-I and W-T12-C3-R-I-V1 had the peculiarity of containing an higher amount of TTIP, which was probably the reason for the higher photoactivity. Overall, the presence of CNCs in the formulation allowed for a homogeneous formation of TiO_2 particles even in case of increased

precursor quantity. These aspects will be treated more in detail in the section dedicated to the sol characterization.

As a final note, also these water-based sol-gels had the same issues of poor aesthetic appearance as most of the other ones. W-T12-C3-R-I and its repetition W-T12-C3-R-I-V1, in particular were more opaque than the others. A brief aesthetic comparison between CNC-based coatings is pictured in Figure 3.42.

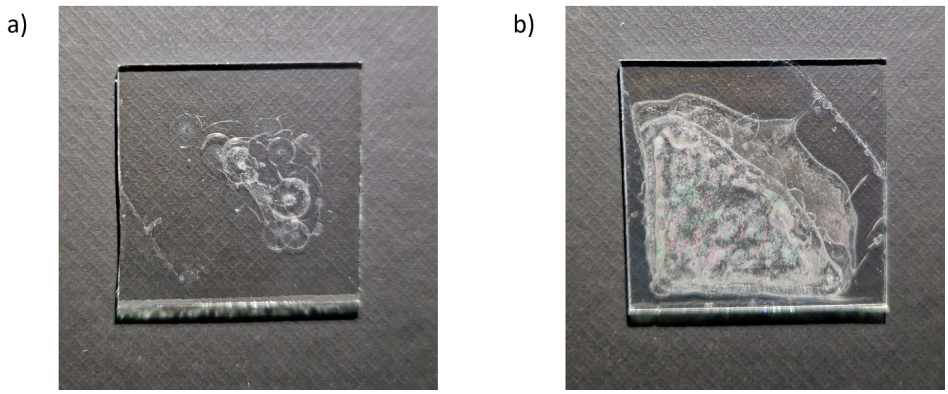

Figure 3.42: Aesthetic appearance of samples W-T10-C3-R-I (a) and W-T12-C3-R-I (b).

3.5. UV-LED photocatalysis results and comparison

After having discussed the screening UV-VIS tests, in this section the results concerning the UV-LED tests are presented. Not all the samples were tested using this method, as only the more photoactive of promising ones were chosen. Some sol-gels, including W-T12-L20-N and W-T12-E5-N, were already presented in the previous section but, for comparison purposes, will be present also in the following discussion.

Prior to that, a brief recap on the k values obtained with the UV-VIS test is presented in Figure 3.43. All the reported samples were the ones further tested with the UV-LED photocatalysis at the same week of ageing.

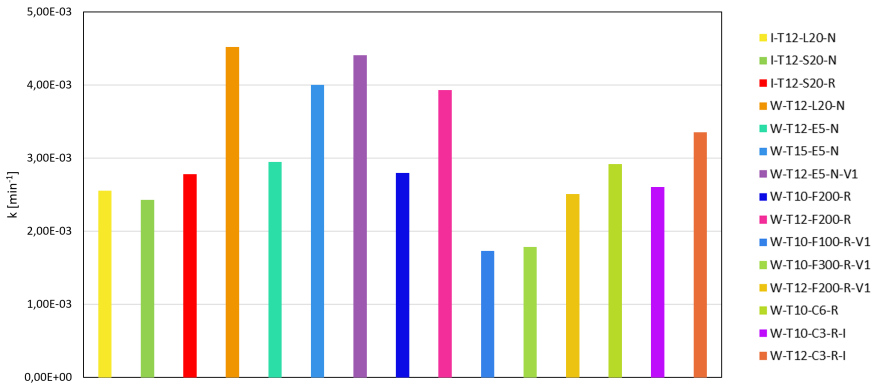

Figure 3.43: Results comparison between the obtained kinetic constants k for some of the UV-VIS tested samples.

The UV-LED test was intended to be a more precise but slow technique to characterize the best samples, as the experimental error connected to this test was lower than the UV-VIS one. It must be noted that the UV-LED photocatalysis utilized a different light source than the UV-VIS, hence, the results were not numerically comparable between the two tests. However, the samples showing good photoactivity during the screening test were expected to maintain a similar behaviour during the UV-LED one.

Among the first prepared sol-gels, the ones formulated with surfactants, only few formulations were tested, mainly water-based ones, as, in general alcohol-based sol-gels did not perform exceptionally well, except few cases. The selected samples were: week 6 I-T12-L20-N, week 6 I-T12-S20-N, week 8 I-T12-S20-R, week 8 W-T12-F200-R, and samples W-T12-L20-N and W-T12-E5-N, given their exceptional results during the UV-VIS tests. The last two were tested for the whole ageing duration, till week 6. Also the variation and reproduction of sol-gel W-T12-E5-N, namely, sol-gels W-T15-E5-N and W-T12-E5-N-V1, were tested at least once to check the reproducibility of the formulation. To facilitate the comparison, just the best kinetic constants k, obtained from the UV-LED photodegradation of the 10^{-5} M solution of RhB, are reported in Figure 3.44. Also, in Figure 3.45, the evolution of k during ageing, for the water and Ecosurf eh-3 based sol-gels is reported.

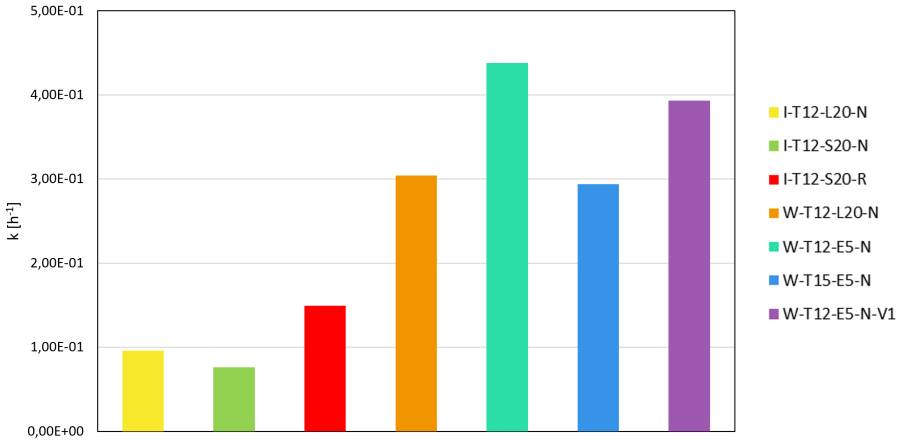

Figure 3.44: Results comparison between the best obtained kinetic constants *k* for the UV-LED tested surfactant-based samples.

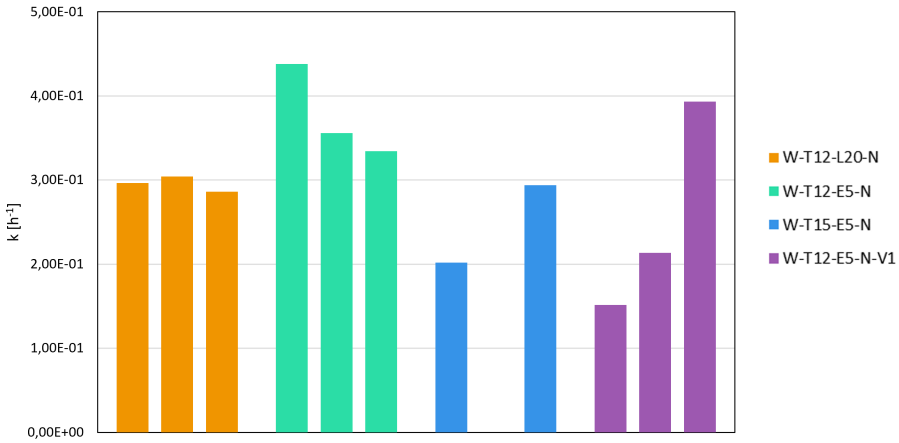

Figure 3.45: Time evolution of UV-LED measured *k* for the water and Ecosurf eh-3 based sol-gels. (Adjacent columns refer to the same sample but at a different ageing week, namely week 2 (left column), week 4 (central column), and week 6 (right column)).

Sol-gels W-T12-E5-N and its repetition, W-T12-E5-N-V1, were the ones showing the highest levels of photocatalytic activity. The former reached its peak performance just after two weeks, while the latter had an increasing photocatalytic activity that reached its maximum after 6 weeks. This difference in the behaviour of the two similar sol-gels could be ascribed to several factors. The synthesis conditions have indeed a strong impact on the photocatalytic properties of the synthesized materials. Since the two formulations were prepared in different periods, diverse environmental conditions, such as temperature and relative humidity, could have led to variations during the reaction steps that were ultimately reflected in the photocatalytic behaviour

differences. Overall, these water and Ecosurf eh-3 based sol-gels constituted great results for the aim of the work, as they were highly photoactive towards the degradation of a dye-polluted solution while also being environmentally friendly from the point of view of the reagents, as Ecosurf eh-3 was the greenest option among the ones available. For these reasons, water-based sol-gel W-T12-E5-N was identified as the best formulation among the surfactant-based ones.

The other formulations tested with the UV-LED photocatalysis did not perform quite as well, except W-T12-L20-N, that, overall, showed an above-average level of photoactivity.

Another batch of sol-gels were tested with the UV-LED photocatalysis, in particular, the nanocellulose based ones that showed good performances during the UV-VIS tests. Both CNF and CNC based samples were chosen since another important step for this research was to identify all the possible beneficial effects that nanocellulose could have brought to the formulation of green sol-gels. The chosen samples were, W-T10-F200-R, W-T12-F200-R, W-T10-F100-R-V1, W-T10-F300-R-V1, W-T12-F200-R-V1, W-T10-C6-R, W-T10-C3-R-I and W-T12-C3-R-I. They were all tested after 6 weeks of ageing. The results, in terms of k values obtained for these samples are reported in Figure 3.46.

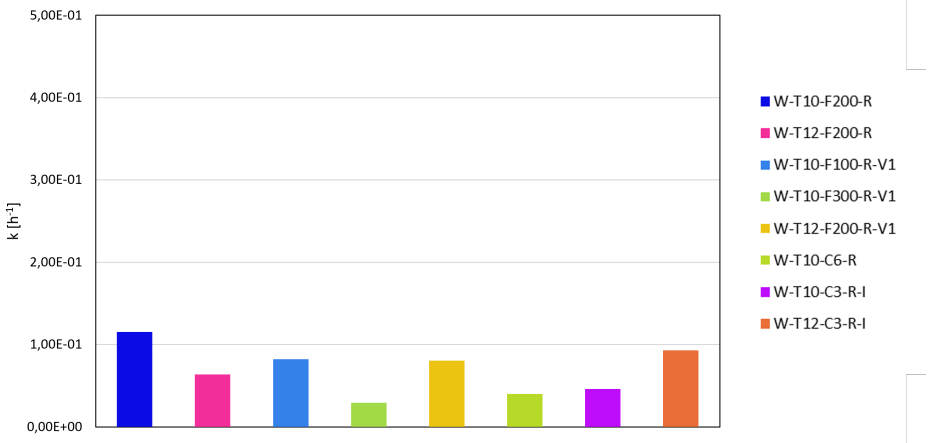

Figure 3.46: Results comparison between the obtained kinetic constants k for the UV-LED tested nanocellulose-based samples.

Overall, no outstanding result was obtained from these tested samples. None of them reached the same level of photoactivity reached by the best surfactant-based sol-gels. Either the ageing time was not sufficient for these samples to produce highly photoactive TiO_2 films or the presence of cellulose did not have significant impact of the photocatalytic properties of the final products. To understand this last point, further investigation was needed in order to identify the surface morphology of the nanocellulose-based coatings. Moreover, in literature, nanocellulose was reported to possibly impact the photocatalytic properties of the synthesized TiO_2 nanopar-

ticles in the visible range, so, it was possible to obtain relatively good levels of photoactivity in the UV-VIS test but no significant improvement was found in the UV-LED one.

This discussion concluded the main characterization procedure, done to find well-performing sol-gels from the point of view of the photocatalytic activity. The UV-VIS and UV-LED tests allowed for the identification of the best formulation, which was then, alongside other ones, further analyzed to find a possible correlation between the measurable characteristics (particles size, surface morphology and thickness of the deposited films) and the photocatalytic activity shown in the RhB degradation tests.

3.6. Sol-gels characterization

In this section, the results concerning the characterization of the sol-gels and the corresponding dip-coated thin films are presented. The discussion will be divided into two main sections, the characterization of nanoparticles size performed with DLS analysis, and the characterization of the morphology of coated samples performed with SEM.

3.6.1. Dynamic Light Scattering

The DLS technique was used to determine the average diameter of the particles present in the prepared sol-gels. This information was important in the determination of the quality of the synthesized material and to identify the formation of clusters or agglomeration in the bulk of the sol.

For the DLS analysis, each sol-gel that was chosen, was firstly diluted in a ratio of 1:10 (in volume) with respect to its proper solvent. The sol-gels to be tested were chosen either based on the results obtained in the UV-VIS or UV-LED photocatalysis or on the nature of the sol-gel. In particular, nanocellulose-based ones, specifically the ones formulated with CNC, were all analyzed to enrich the characterization of these novel formulations.

All the tested samples with their respective results are listed in Table 3.4. It could be noted that all the alcohol-based sol-gels had quite large particles detected by the instrument. This confirmed the formation of clusters or agglomeration of particles due to instabilities in the volume of the sol. In fact, almost all the isopropanol-based formulations, sooner or later, encountered the issue of precipitate formation. The presence of clustered structures could be verified also by the broadness of the diameters distribution which suggests the presence of inhomogeneous agglomerates of nanoparticles. This could be seen, for example, from the spectra of sol-gels I-T12-L20-N (Figure 3.47) and I-T12-S20-N (Figure 3.48).

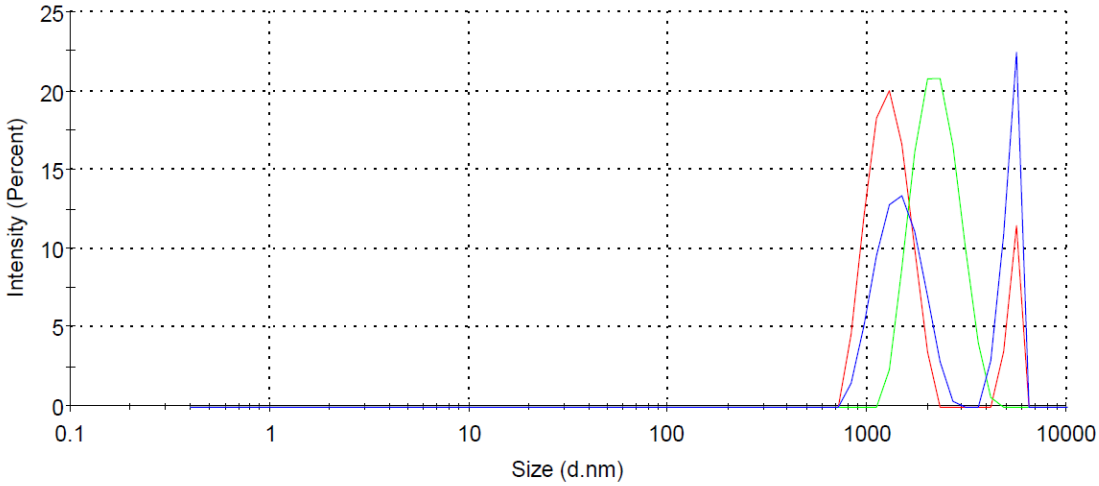

Figure 3.47: Size distribution by intensity plot of sol-gel I-T12-L20-N, output of the DLS analysis.

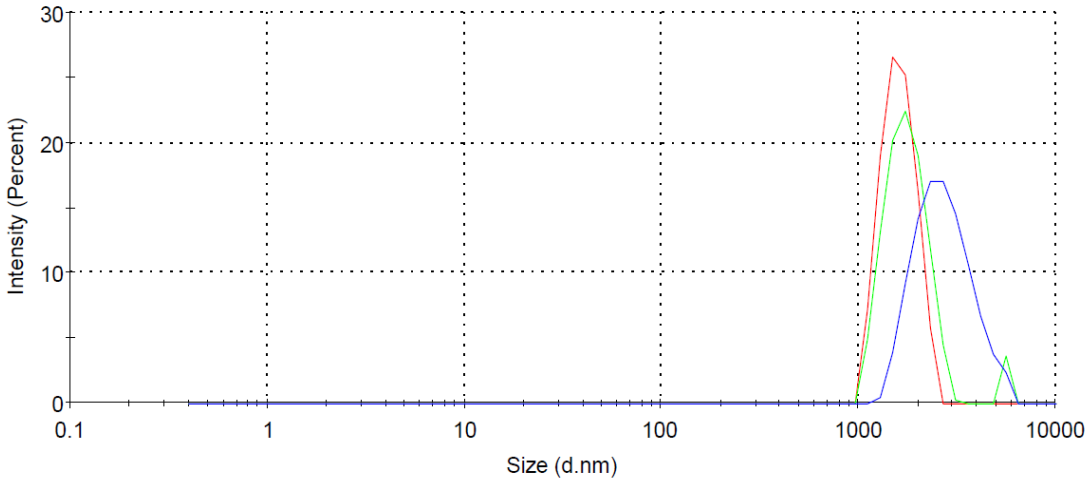

Figure 3.48: Size distribution by intensity plot of sol-gel I-T12-S20-N, output of the DLS analysis.

Table 3.4: Results of DLS analysis.

Solvent	Surf./NC	Sol-gel	Avg. particles ø [nm]	PdI
Isopropanol	L	I-T10-L20-N	1813	0.483
		I-T12-L20-N	2317	0.507
		I-T12-L20-N-U	2638	0.459
	S	I-T10-S20-N	1831	0.357
		I-T12-S20-N	1809	0.261
		I-T12-S20-R	1481	0.126
Water	-	W-T10-R-I	42	0.219
	L	W-T12-L20-N	38	0.156
	E	W-T12-E5-N	39	0.261
		W-T15-E5-N	43	0.179
		W-T12-E5-N-V1	35	0.149
		W-T12-E5-N-V2	36	0.171
	CNF	W-T12-F200-R	40	0.203
		W-T10-F100-R-V1	46	0.306
		W-T10-F200-R-V1	46	0.246
		W-T10-F300-R-V1	45	0.229
		W-T12-F200-R-V1	53	0.253
	CNC	W-T10-C6-R	51	0.271
		W-T10-C3-R	58	0.273
		W-T10-C3-R-I	61	0.289
		W-T12-C3-R-I	72	0.365
		W-T10-C6-R-V1	43	0.235
		W-T10-C3-R-V1	50	0.272
		W-T10-C3-R-I-V1	46	0.247
		W-T12-C3-R-I-V1	52	0.269

On the other hand, all the water-based formulations contained very fine nanoparticles. The smallest ones, with a diameter lower than 40 nm were, as expected, inside the best performing

water and surfactant based sol-gels. The DLS spectra of sol-gels W-T12-L20-N and W-T12-E5-N are pictured in Figure 3.49 and Figure 3.50, respectively.

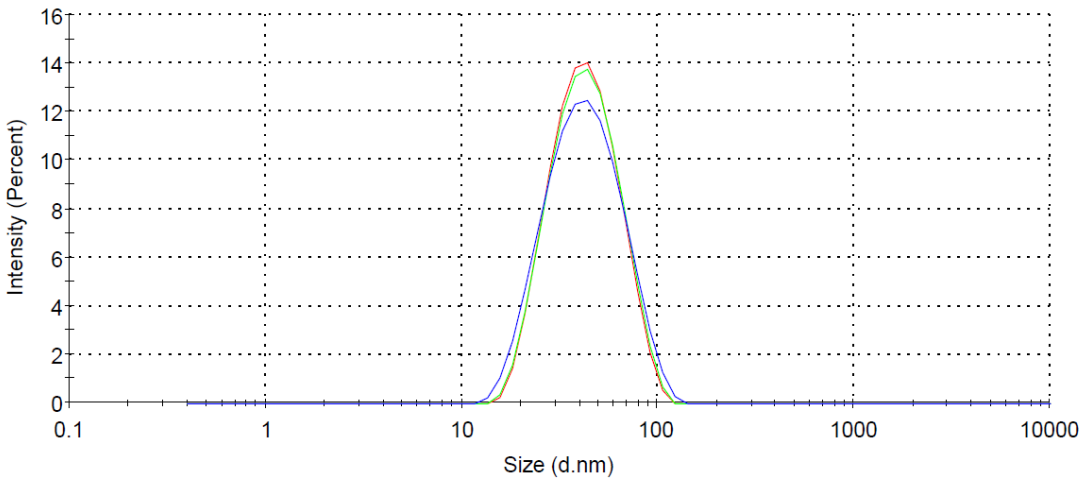

Figure 3.49: Size distribution by intensity plot of sol-gel W-T12-L20-N, output of the DLS analysis.

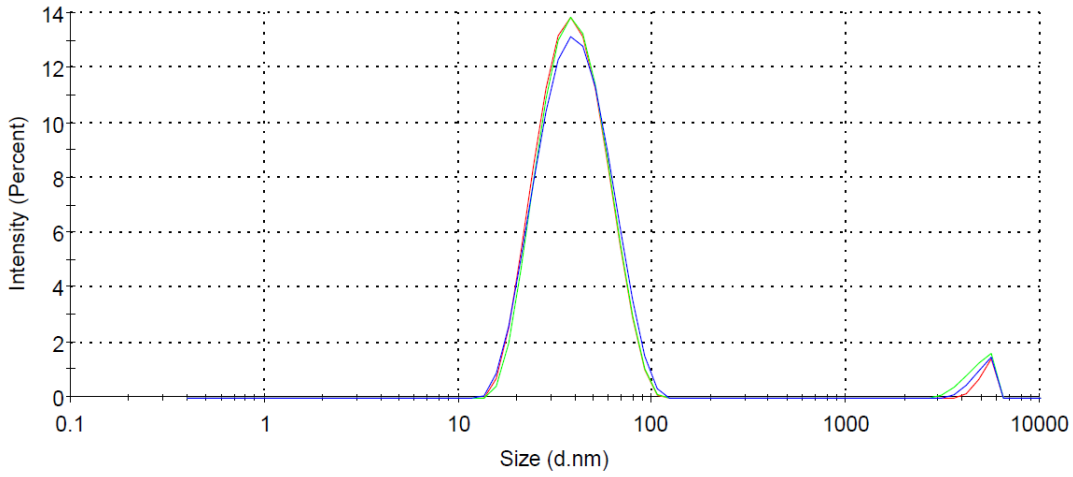

Figure 3.50: Size distribution by intensity plot of sol-gel W-T12-E5-N, output of the DLS analysis.

From the results obtained for nanocellulose based sol-gels it was possible to make a few hypotheses. Average particles diameter was lower than the one measured to check the success of the hydrolysis reaction: this could be interpreted as nanocellulose suspension forming bigger structures that then disgregated upon further dilution, which was performed before producing the sol. Another hypothesis could be that the amount of nanocellulose inside the sol-gel was too

low that the analyzed portion did not contain relevant traces of it, below the instrument sensitivity. This last hypothesis is the least likely, since the diluted suspensions used for the preparation of CNC and CNF based sol-gels were clearly distinguishable from water as they had a homogeneous white semi-transparent look, meaning that the refractive index of the suspension was different due to the homogeneous dispersion of CNfs or CNCs inside it. The spectra of two sol-gels, one CNF-based (W-T12-F200-R) and the other CNC-based (W-T12-C3-R-I), are reported in Figure 3.51 and Figure 3.52 respectively.

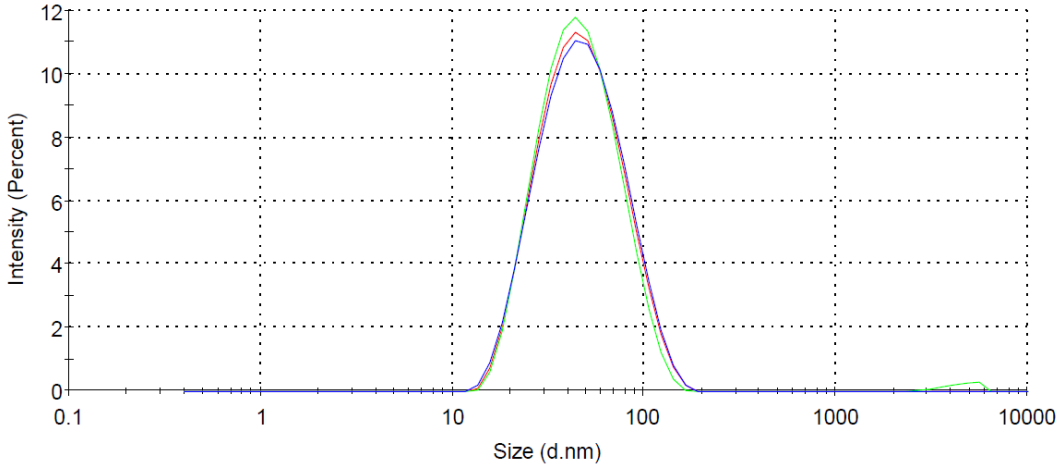

Figure 3.51: Size distribution by intensity plot of sol-gel W-T12-F200-R, output of the DLS analysis.

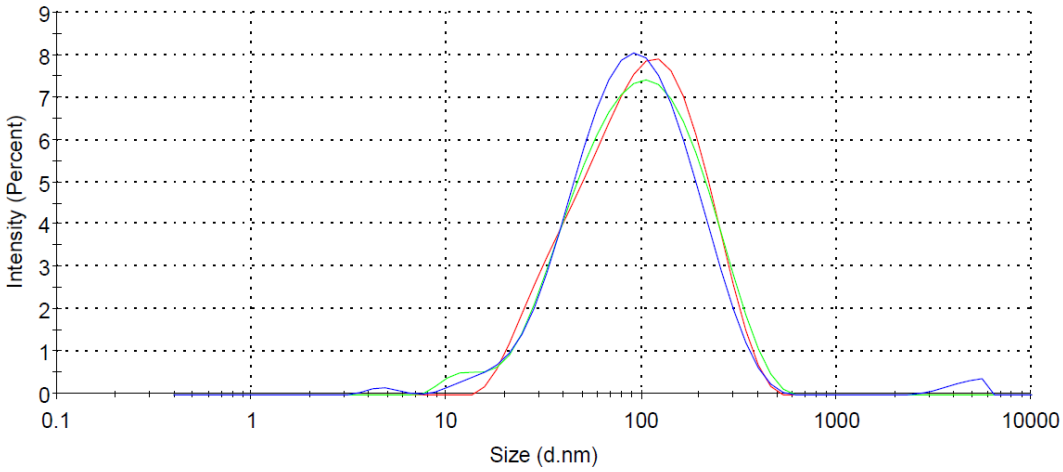

Figure 3.52: Size distribution by intensity plot of sol-gel W-T12-C3-R-I, output of the DLS analysis.

Another aspect that could be identified from the data analysis of the DLS experiments was the particles dimension change during ageing. Since repetitions sol-gel were tested at different ageing times with respect to the original one, it was possible to track the evolution of the average nanoparticles diameter across this time period. From the results, it was possible to see that the average particles diameter was increasing with ageing time.

The DLS analysis showed that the isopropanol-based sol-gels had bulk microscopic clustered structures inside the solution and this could explain both the precipitate formation and the low photocatalytic activity, especially on the long term. On the other hand, the sol-gels that were identified as best performing showed the finest particles size among all the samples: this could explain the really high photoactivity, as finer particles size is reflected in higher surface area in the final dip-coated sample. This analysis also showed that nanocellulose-based sol-gels produced slightly bigger particles. This could be due to two different reasons, the first one being that the spacing effect caused by nanocellulose was slightly worse than the one caused by non-ionic surfactants, hence, the particles grew to a slightly bigger size. The second, in particular for CNC-based sol-gels, was the fact that TiO_2 particles could grow and incorporate sulfate ions present in the sol; the presence of such ions could have led to slightly higher average particle diameter.

Overall, the DLS analysis was important to prove the relationship between the average particles size of a sol-gel formulation and its photocatalytic or bulk propertis.

3.6.2. Scanning Electron Microscopy

In this section the results obtained from the SEM analysis of the deposited thin films are presented. Due to the large amount of produced samples, only the more relevant ones were chosen for SEM analyses. In a couple of cases, SEM results were coupled with the spot EDX analysis to determine the chemical composition of specific parts in the surface of the material.

In Figure 3.53, the surface morphology of samples I-T12-L20-N and I-T10-L7-R-U is shown. These were the two alcohol and Lutensol ON70 based sol-gels representatives. The former was deposited after 6 weeks of ageing, while the latter was dip-coated after 2 weeks of ultrasonication.

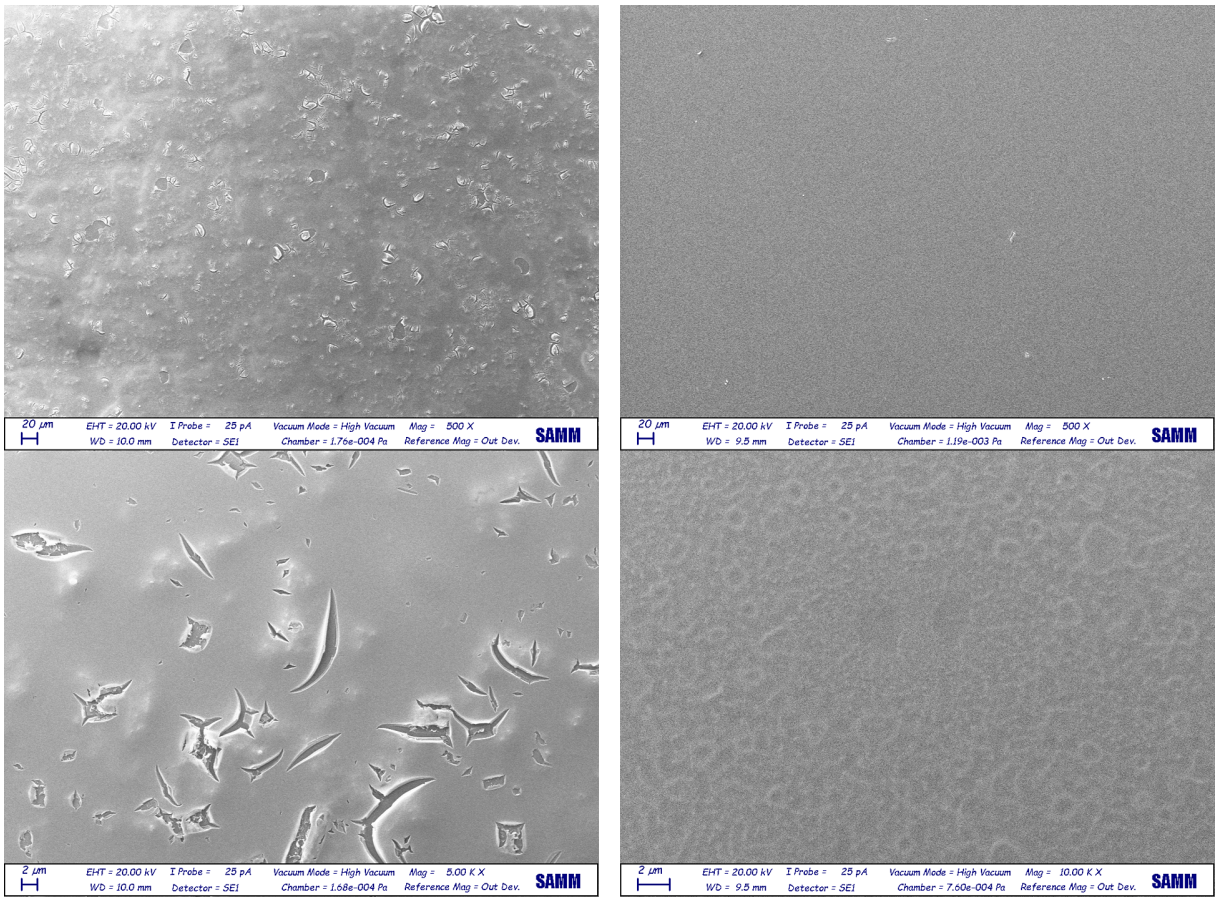

Figure 3.53: SEM images at different magnification levels of samples I-T12-L20-N (left) and E-T10-L7-R-U (right).

Sample I-T12-L20-N presented a microcracked surface with visible inhomogeneities. These could be seen from the uneven thickness of the coating and the presence of tiny debris all over the area of the sample. This morphology may have influenced the photocatalytic activity of the sample, which was relatively low at the 6th week. On the other hand, sample E-T10-L7-R-U showed a very smooth surface with some homogeneous micrometric patterning visible only at high magnification. This effect was probably induced by the presence of the surfactant, that, combined with the organic solvent, allowed for a even coating of the surface with a patterning effect that may have enhanced the active area for photocatalysis. This week was in fact the one where it reached its maximum level of photoactivity. This value was however average since, overall, the thickness of the coating was very low, measured at around 250 nm per layer (Figure 3.54). This value was measured at the edge of a small isolated crack visible at extremely high magnification (75000x).

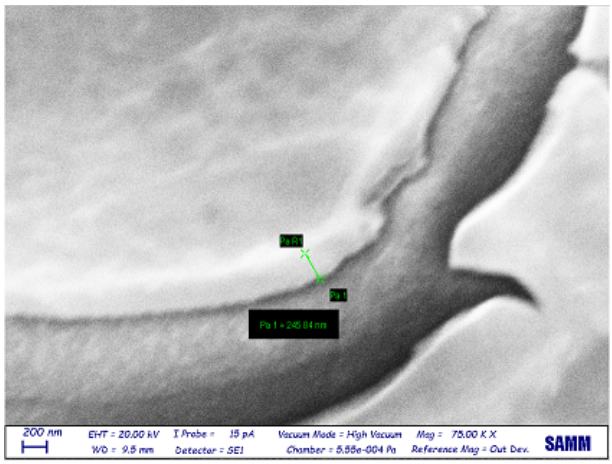

Figure 3.54: Thickness measurement using SEM for sample E-T10-L7-R-U.

For what concerns SDS-based formulations, two samples were tested, in particular E-T10-S5-R and I-T12-S20-R. The morphology of these samples is shown in Figure 3.55. Both samples were coated when the sol-gel was 6 weeks old.

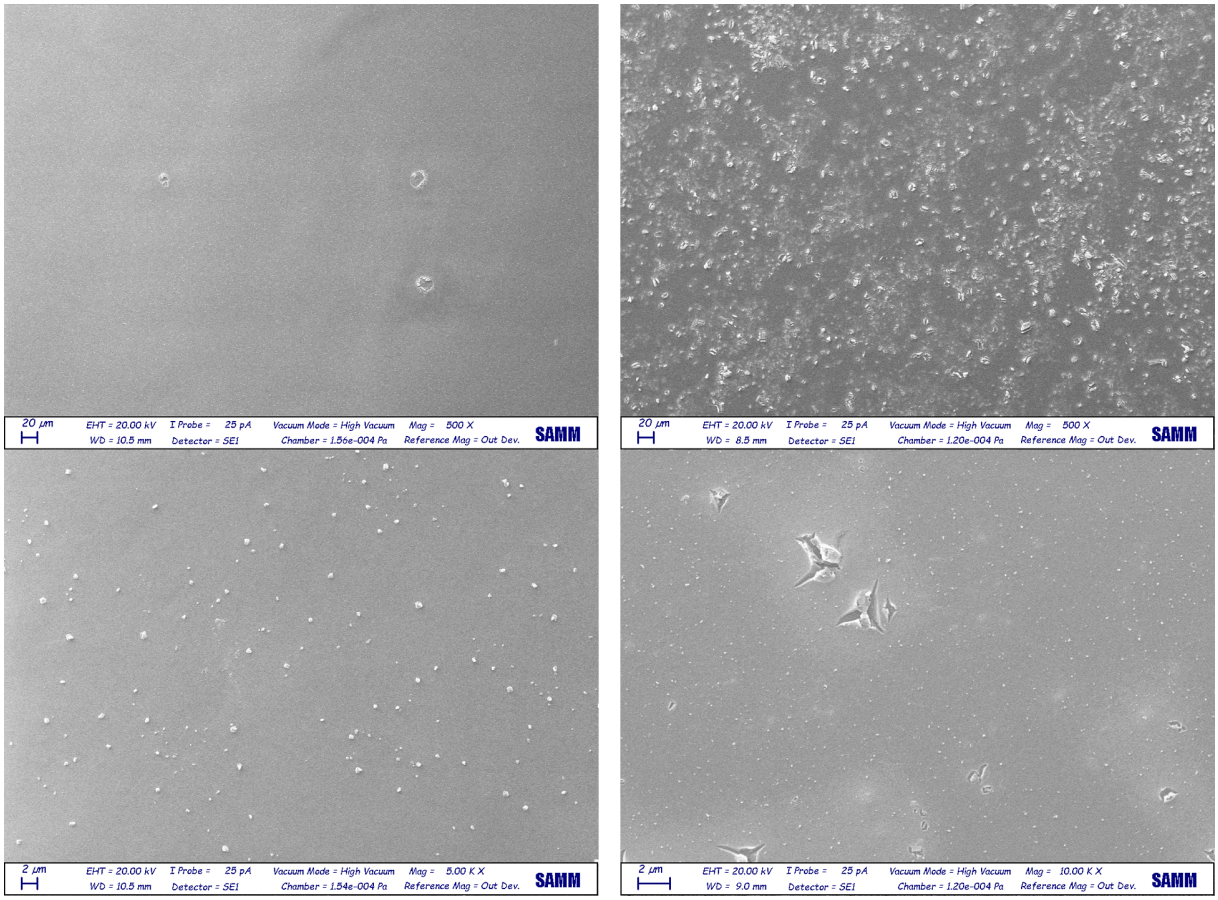

Figure 3.55: SEM images at different magnification levels of samples E-T10-S5-R (left) and I-T20-S20-R (right).

This image showed that, also in this case, the ethanol-based formulation produced a very smooth coating with only few surface defects. On the other hand, the isopropanol-based sol-gel produced a more uneven surface with a strong presence of microcracks. SDS-based formulations showed also an interesting detail. On the surface of both coatings, some white particles could be seen at high magnification. The dimension of those particles was different between the two tested samples; for sample E-T10-S5-R the particles were already visible at the 5000x magnification, while for sample I-T12-S20-R, they were much smaller and only visible starting from a 10000x magnification. To better identify the nature of such particles, a spot EDX analysis was performed on the ethanol-based sample in the exact position of one of the bigger particles. The results, reported in Figure 3.56, showed that the composition of these particles was different from the adjacent smooth region. In particular, the peak of sulfur was present in the particle spot, suggesting that the particles were residues of the surfactant itself. The same test was not repeatable on sample I-T12-S20-R as the dimension of such particles was much smaller and the thin gold layer was not sufficiently conductive to form a better image.

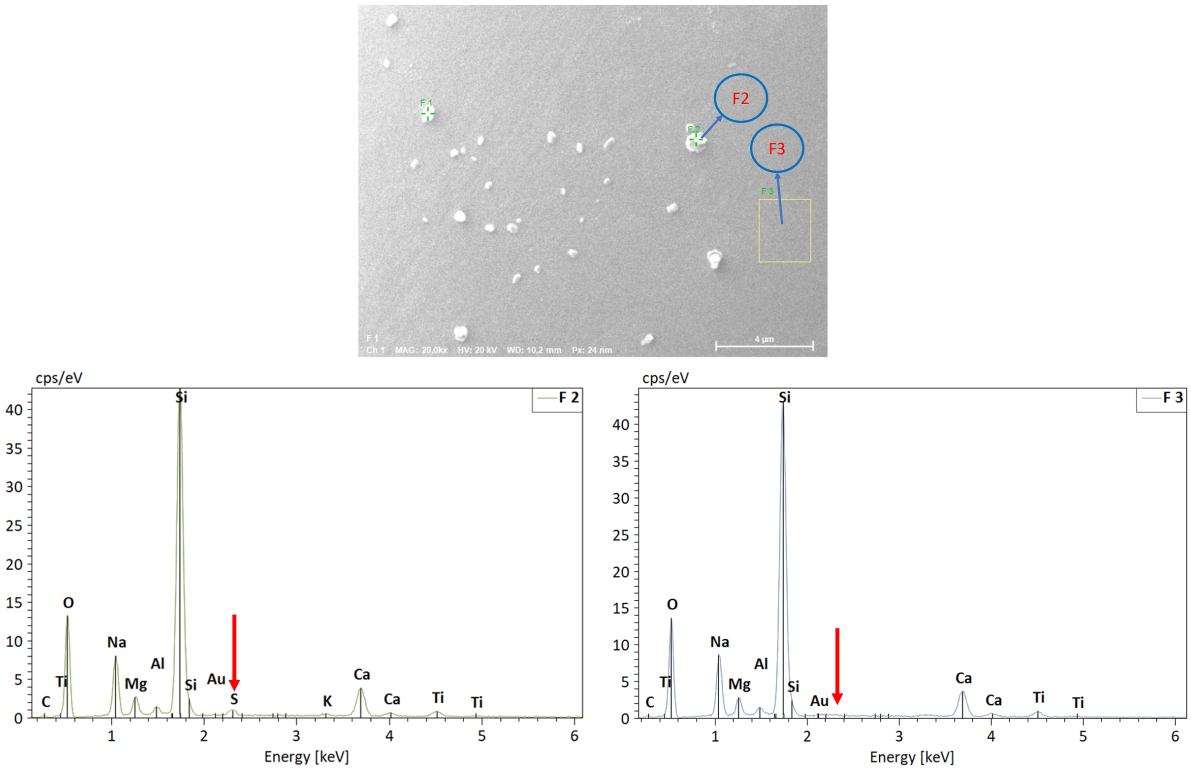

Figure 3.56: EDX analysis of the particles present on the surface of sample E-T10-S5-R. On the left, the spectrum obtained from the particle analysis (F2); on the right, the spectrum obtained from the smoothly coated area (F3). Highlighted in red: sulfur peak position.

The presence of SDS particles could have influenced the photocatalytic behaviour of the aforementioned sol-gels, in particular, decreasing the active area available for the photocatalytic re-

action to take place. For this reason, even though the surface of E-T10-S5-R was really smooth and compact, the photoactivity was not so great. On the contrary, sample I-T12-S20-R showed a slightly higher level of photoactivity since the sulfate inclusions were much smaller, but the overall photocatalytic level was average at best due to the inhomogeneous microcracks present on the surface and due to the large particle size, as measured by DLS.

Sol-gels W-T12-L20-N and W-T12-E5-N were classified as the best performing samples due to their high photocatalytic activity. The morphology of these two samples is shown in Figure 3.57. The first one was tested at week 4 since it was the time when it reached its peak photoactivity in the UV-VIS test, while the other was tested at week 2, when it reached the highest value of photocatalytic activity in the UV-LED test.

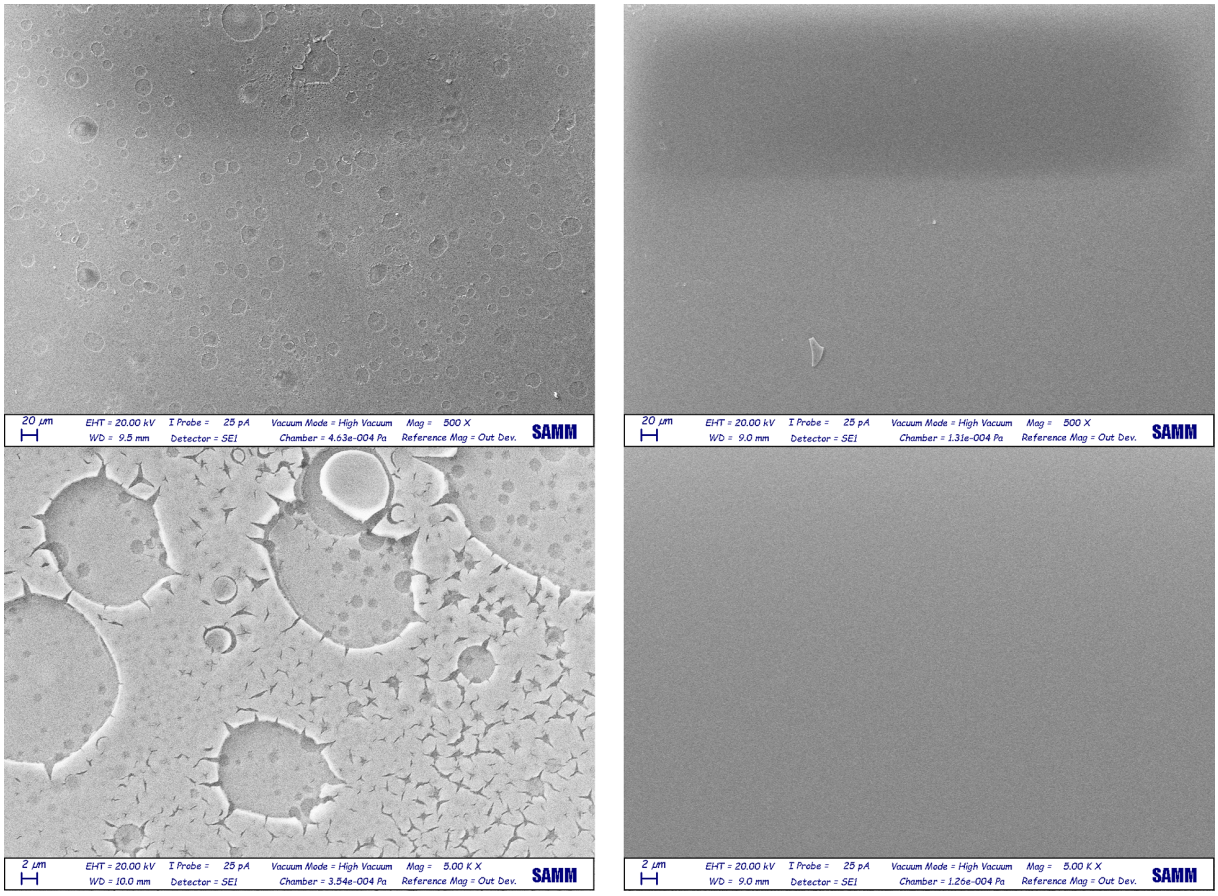

Figure 3.57: SEM images at different magnification levels of samples W-T12-E5-N (left) and W-T12-L20-N (right).

Sample W-T12-E5-N showed a strongly cratered structure. This was possible thanks to the effect of the surfactant Ecosurf eh-3 that created a controlled porosity in the final film. The craters were analyzed with EDX in order to understand the local composition and the results are reported in Figure 3.58.

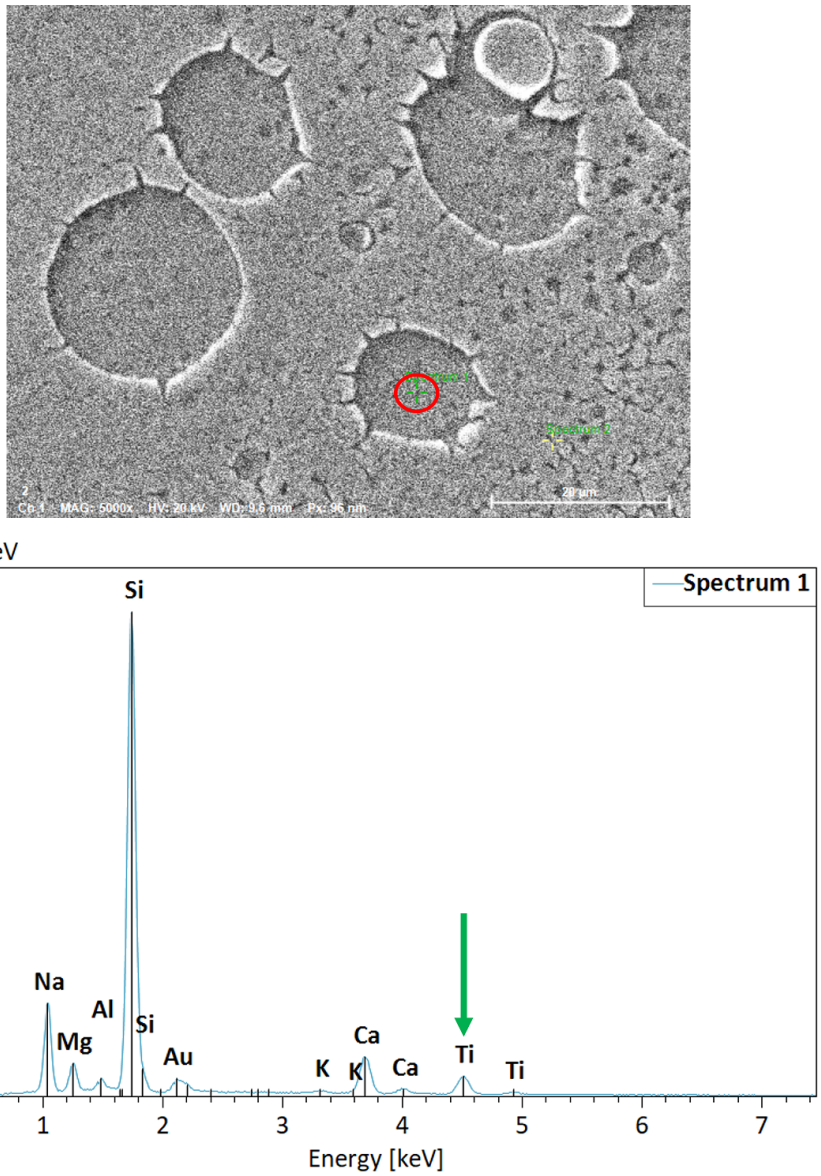

Figure 3.58: EDX analysis of the craters present on the surface of sample W-T12-E5-N. Highlighted in red: the analyzed crater zone. Highlighted in green: the peak of titanium.

This analysis showed that the region inside the craters was the lower dip-coated layer, as the Ti peak was present in the EDX spectrum. From the morphological point of view, the patterned surface showed a high surface area which was ultimately beneficial for the photocatalytic activity of the sample. Having more area available for the reaction, combined with the presence of homogeneously distributed cavities, and small particle size, led to a very strong photocatalytic degradation of the dye-polluted solution under the irradiation of UV light.

On the other hand, sample W-T12-L20-N was completely smooth without any crack. This coating was strongly adherent and compact. The lower surface area could be the reason of

the lower photoactivity showed in the UV-LED test. Nevertheless, the extremely high film homogeneity was reflected in an almost perfect aesthetic appearance, as already mentioned in section 3.4.4.

To fully characterize the best performing formulation, also sol-gels W-T15-E5-N and W-T12-E5-N-V1 were analyzed with the SEM. Both were analyzed at week 6 to understand the evolution in the morphology at the end of the ageing period. The results concerning these two samples are pictured in Figure 3.59.

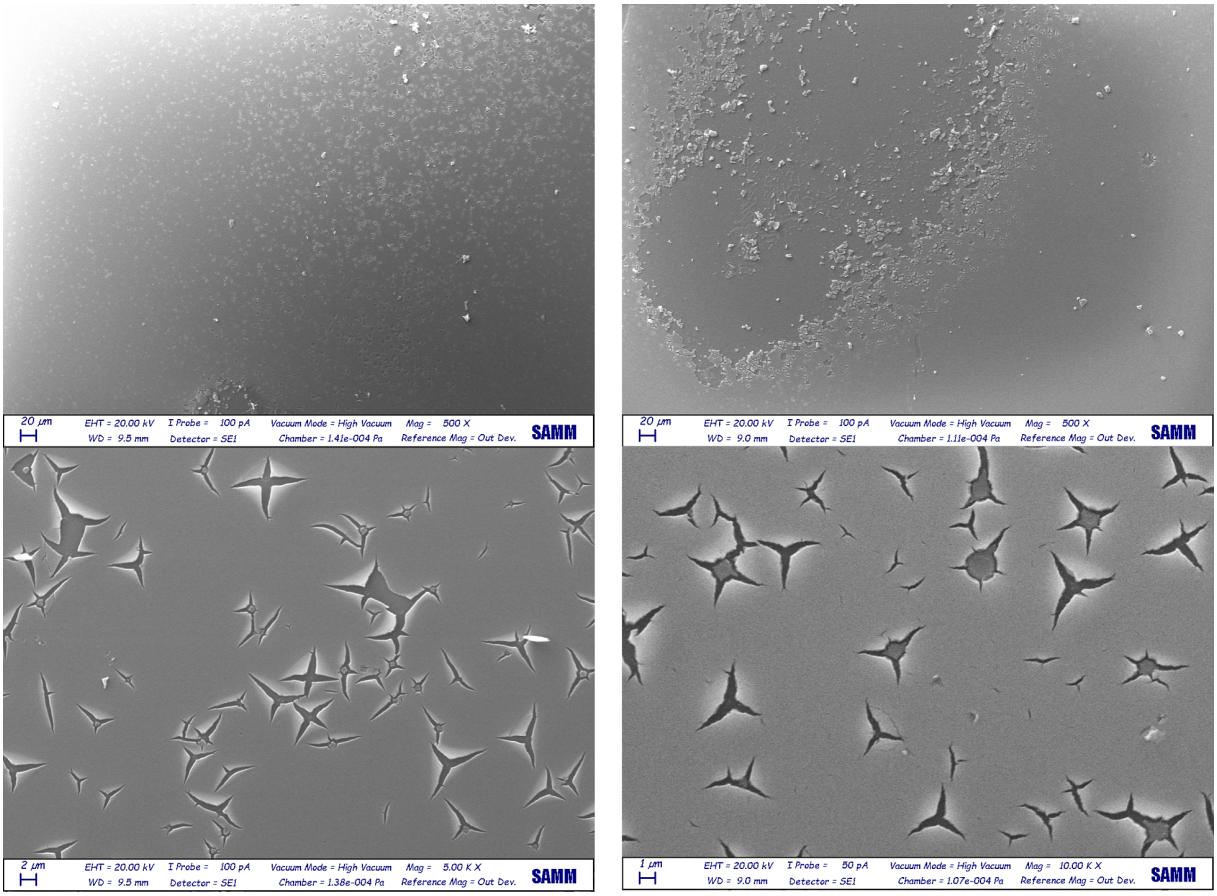

Figure 3.59: SEM images at different magnification levels of samples W-T15-E5-N (left) and W-T12-E5-N-V1 (right).

The structure of the two samples was pretty similar, as there were many microcracks and the surface was, overall, not very homogeneous. In this case no crater was present. The main difference that was reported from the SEM analysis was in the thickness of the two films. The upper layer of sample W-T15-E5-N was measured to be around 150 nm at the edges of the microcracks. For the other one, the measured thickness was almost 800 nm. This could be the main reason that explained the difference in photocatalytic activity between these two sol-gels, being the thicker coating also more photoactive.

The last samples tested with the SEM were W-T12-F200-R and W-T12-C3-R-I-V1, being them the more photoactive ones among all the nanocellulose based formulations. The surface morphology of these samples is shown in Figure 3.60. All of them were analyzed at the 6th week of ageing of the sol-gel.

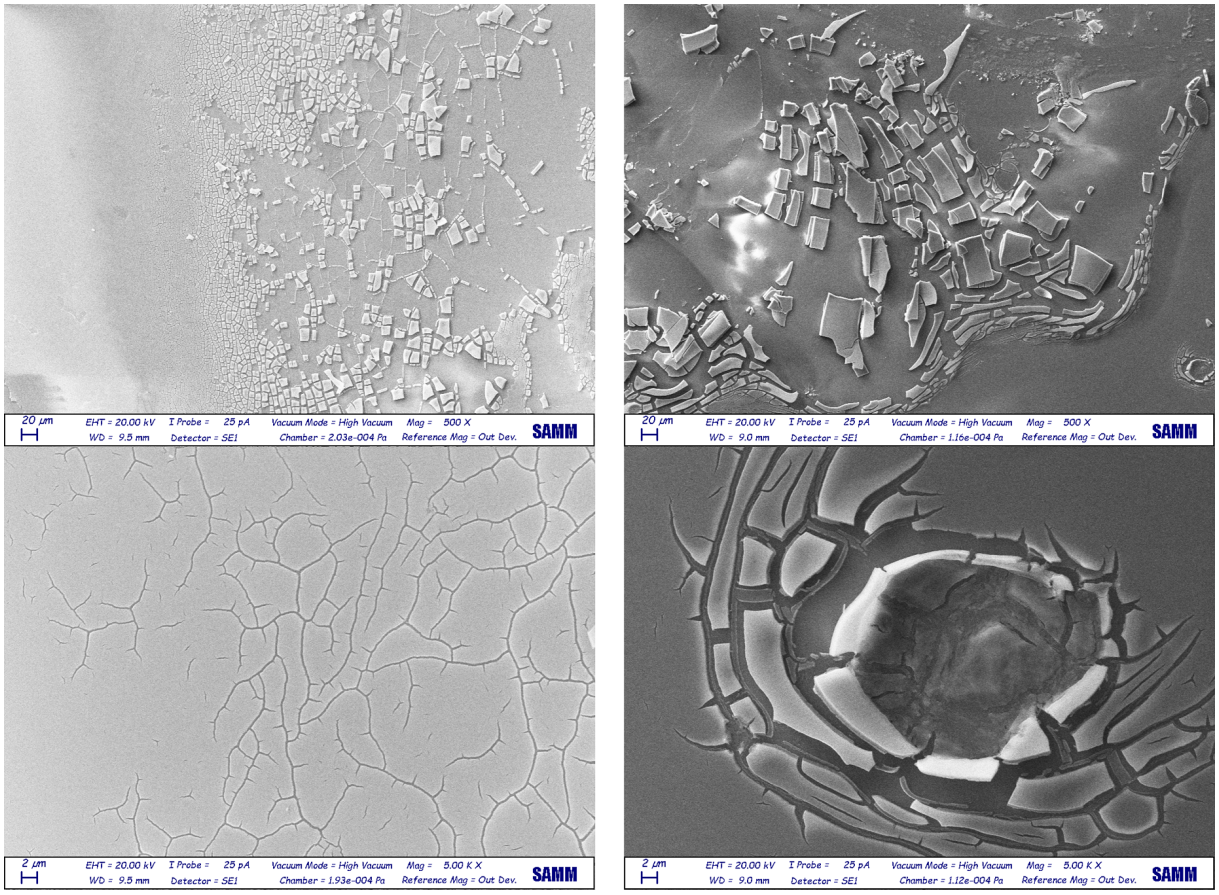

Figure 3.60: SEM images at different magnification levels of samples W-T12-F200-R (left) and W-T12-C3-R-I-V1 (right).

The CNF-based sol-gel produced a widely cracked surface with a dendritic structure of the cracks. Outside the cracked and disbonded area, the surface of this sample was quite homogeneous in terms of thickness. On the other hand, the CNC-based sample showed a strongly inhomogenenous cracked morphology that presented also a few cratered spots. In the case of sample W-T12-C3-R-I-V1, an EDX spot analysis was performed to check the presence of sulfates in the composition of the coating; however, no signal of element S was visible from the spectrum. Overall, the effect of nanocellulose on the morphology was not homogeneous and probably this caused the photocatalytic activity to be fairly low.

The SEM and SEM-EDX analyses were useful for finding the correlation between the surface morphology and composition of the samples with their photocatalytic performance.

3.7. Samples photoactivity trend

In this brief section, the main trend found for the photocatalytic activity of the water-based samples is reported. This discussion did not involve the alcohol-based formulations as they were, overall, inferior in terms of photoactivity. In Figure 3.61, the *k* trend found for different amounts of TTIP and surfactant or nanocellulose type is pictured. The represented points were obtained using the average of best values of the UV-LED obtained kinetic constants for each type of sol-gel.

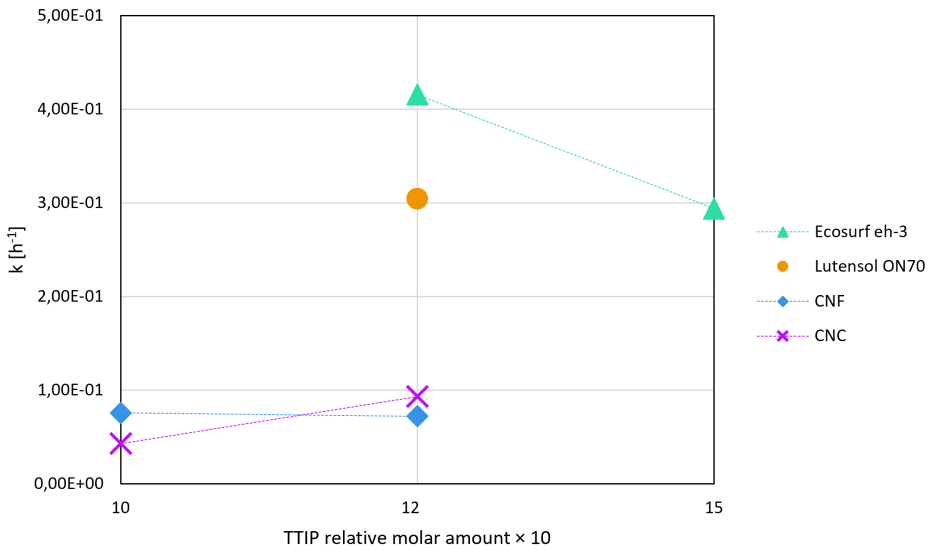

Figure 3.61: UV-LED kinetic constant *k* at different amounts of TTIP for the different types of water-based formulations.

On average, it could be noted that the intermediate amount of TTIP (1.2 molar) was the one leading to the best results among different types of templating agents. In the plot it was difficult to identify a proper trend since the data available was heterogeneous. However, it could be stated that the amount of TTIP was one of the main determining factors for the photoactivity of the final samples; lower amounts of precursor could lead to average or good levels of photocatalytic activity in longer periods of time without causing a loss of stability inside the sol-gel; slightly higher amounts of TTIP could produce higher levels of photoactivity if the amount of spacing agent was enough to maintain the homogeneity of the sol; High amounts of TTIP should require more solvent to be able to match the same properties of less concentrated sols, even if the formulation was not unstable.

The simultaneous effect of different parameters was also crucial as, for example, the nanocellulose dilution level led to different results with respect to what was previously reported for the

TTIP amount. In Figure 3.61 it could be seen that, for the CNF-based formulations, the increase in TTIP amount led to a very slightly decrease in photoactivity, contrary to the CNC-based sol-gels. In Figure 3.62, the trend of k for different levels of dilution of the nanocellulose-based samples is reported. These values were identified following the same rule as the previous plot.

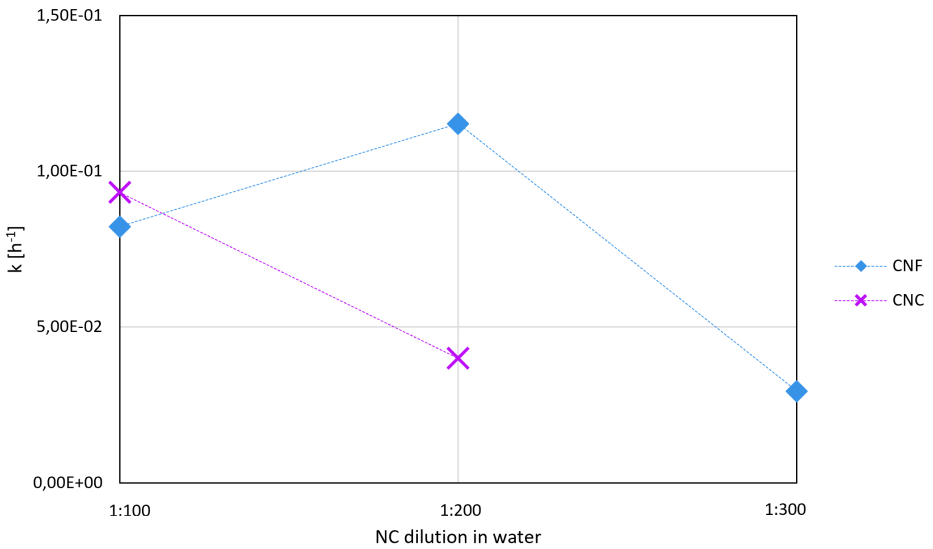

Figure 3.62: UV-LED kinetic constant k at different nanocellulose suspension dilution.

It should be noted that the dilution 1:100 in the case of CNF corresponds to the 1:3364 dilution for CNC, as they have the same amount of solid dispersed in water. Similarly, CNF 1:200 dilution corresponds to CNC 1:6699 dilution. It could be noted that 1:200 dilution was optimal for CNF-based sol-gels, while 1:100 (1:3364) was better for CNC-based formulations. This could be explained by the presence of residual sulfate in the CNC suspension, hence, the actual amount of nanocellulose present in suspension was lower with respect to the correspondent CNF dilution level.

4 | Conclusions and future perspectives

The aim of this work was to test several templated titanium dioxide sol-gel formulations to find the ones that showed the best results in terms of photocatalytic activity. Different types of surfactants and nanocellulosic materials were employed in the TiO_2 synthesis to test whether their effect was beneficial to the photoactivity of the final dip-coated samples. Several synthesis parameters were also varied, in order to document their effect. The formulation of the sol-gels was also kept as environmentally clean as possible, limiting the usage of harmful reagents.

The best performing sol-gels were identified through the UV-VIS and further UV-LED photocatalytic tests. The ones reaching the highest photoactivity were the water and Ecosurf eh-3 based sol-gels, produced following the normal addition method and with a sightly higher amount of precursor with respect to previous works formulations. The role of the non-ionic surfactant molecule was fundamental in ensuring the sol-gel stability during the ageing period, contributing also to the low environmental impact of the material synthesis.

Nanocellulose-based formulations have been widely investigated as this material looked promising for the application in sustainable titanium dioxide sol-gel synthesis. However, the obtained results were not good enough to be able to establish the samples applicability as efficient photocatalyst. The same results were seen, on average, also for the formulations prepared with organic solvents such as isopropanol and ethanol.

Further instrumental analyses helped correlating the photocatalytic properties of the tested samples to their physical ones. DLS was useful to identify the particles size formed during the sol-gel synthesis and the possible clusters formation. Really small nanoparticles were obtained in the best performing formulations. SEM imaging was also fundamental to identify the surface features of the best coatings and, combined with the EDX analysis, it was possible to approximately understand the spot composition of the TiO_2 thin films. High compactness or controlled porosity were found to be the best features for enhanced surface area and photocatalytic activity, confirming the beneficial role of surfactants in promoting homogenous coverage of the samples surface or introducing controlled patterns.

The introduction of surfactants and nanocelluse as templates for the sol-gel synthesis of titanium dioxide led to promising results as the best samples reached high photoactivity in relatively short

ageing times; they also contributed in producing highly stable sol-gels by controlling the size of the synthesized particles, in particular, in the case of water-based formulations. The surfactant Lutensol ON70 also helped in the production of extremely compact and homogeneous TiO_2 thin films, with above average photocatalytic activity and flawless aesthetic appearance, actually solving one of the main issues encountered when dealing with water-based titanium dioxide coatings and making its applicability in larger scale water purification more feasible.

This work was the starting point towards the development of highly photoactive templated TiO_2 sol-gels. Future studies should focus on the optimization of the water and Lutensol ON70 or Ecosurf eh-3 based formulations. This could be achieved by modifying the synthesis parameters and deeply investigating the structure, thickness and composition of the produced thin films via instrumental techniques such as X-Ray diffraction (XRD) and SEM. Further analyses should be performed also for the nanocellulose based formulations, since this material has many advantages related to its sustainability.

Future works should also focus on implementing completely sustainable reagents for the templated synthesis of titanium dioxide. The topic of sustainable and green processes is becoming increasingly important and several new regulations will be surely issued in the future. The introduction of renewable sources such as starch, agar or the already mentioned nanocellulose, should be tested for the production of highly sustainable products.

Titanium is also classified as a critical raw material by the European commission. Future studies should also take into account the life cycle assessment related to the production of titanium-based photocatalysts, and expand towards the usage of alternative photocatalytic materials.

Bibliography

[1] A. Rafiq, M. Ikram, S. Ali, F. Niaz, M. Khan, Q. Khan, and M. Maqbool, "Photocatalytic degradation of dyes using semiconductor photocatalysts to clean industrial water pollution," *Journal of Industrial and Engineering Chemistry*, vol. 97, pp. 111–128, 2021.

[2] A. Kumar and G. Pandey, "A review on the factors affecting the photocatalytic degradation of hazardous materials," *Mater. Sci. Eng. Int. J*, vol. 1, no. 3, pp. 1–10, 2017.

[3] T. Lazar, "Industrial dyes—chemistry, properties, applications," 2005.

[4] N. Daneshvar, D. Salari, and A. Khataee, "Photocatalytic degradation of azo dye acid red 14 in water: investigation of the effect of operational parameters," *Journal of Photochemistry and Photobiology A: Chemistry*, vol. 157, no. 1, pp. 111–116, 2003.

[5] T. Ochiai and A. Fujishima, "Photoelectrochemical properties of tio2 photocatalyst and its applications for environmental purification," *Journal of Photochemistry and photobiology C: Photochemistry reviews*, vol. 13, no. 4, pp. 247–262, 2012.

[6] J. Livage, M. Henry, and C. Sanchez, "Sol-gel chemistry of transition metal oxides," *Progress in solid state chemistry*, vol. 18, no. 4, pp. 259–341, 1988.

[7] A. K. Al-Buriahi, A. A. Al-Gheethi, P. S. Kumar, R. M. S. R. Mohamed, H. Yusof, A. F. Alshalif, and N. A. Khalifa, "Elimination of rhodamine b from textile wastewater using nanoparticle photocatalysts: a review for sustainable approaches," *Chemosphere*, vol. 287, p. 132162, 2022.

[8] I. Yahia, Y. Rammah, and K. Khaled, "Fabrication of an electrochemical cell based on rhodamine b dye for low power applications," *Journal of Materials and Environmental Science*, vol. 4, no. 3, pp. 442–47, 2013.

[9] M. A. Brown and S. C. De Vito, "Predicting azo dye toxicity," *Critical reviews in environmental science and technology*, vol. 23, no. 3, pp. 249–324, 1993.

[10] H. Tahir and M. Saad, "Chapter 3 - using dyes to evaluate the photocatalytic activity," in *Photocatalysis: Fundamental Processes and Applications* (M. Ghaedi, ed.), vol. 32 of *Interface Science and Technology*, pp. 125–224, Elsevier, 2021.

[11] A.-L. Anderson, *Tailoring titanium dioxide thin films for photocatalysis and energy efficient glazing via dye-sensitised solar cells*. PhD thesis, Queen Mary University of London, 2017.

[12] "Electrical conductor, semiconductor and insulator." `https://electric-shocks.com/electrical-conductor-semiconductor-and-insulator/`, Accessed 2023.

[13] M. Pelaez, N. T. Nolan, S. C. Pillai, M. K. Seery, P. Falaras, A. G. Kontos, P. S. Dunlop, J. W. Hamilton, J. Byrne, K. O'Shea, M. H. Entezari, and D. D. Dionysiou, "A review on the visible light active titanium dioxide photocatalysts for environmental applications," *Applied Catalysis B: Environmental*, vol. 125, pp. 331–349, 2012.

[14] T. Tachikawa, M. Fujitsuka, and T. Majima, "Mechanistic insight into the tio2 photocatalytic reactions: design of new photocatalysts," *The Journal of Physical Chemistry C*, vol. 111, no. 14, pp. 5259–5275, 2007.

[15] C. A. Emilio, M. I. Litter, M. Kunst, M. Bouchard, and C. Colbeau-Justin, "Phenol photodegradation on platinized-tio2 photocatalysts related to charge-carrier dynamics," *Langmuir*, vol. 22, no. 8, pp. 3606–3613, 2006.

[16] W. Choi, A. Termin, and M. R. Hoffmann, "The role of metal ion dopants in quantum-sized tio2: correlation between photoreactivity and charge carrier recombination dynamics," *The Journal of Physical Chemistry*, vol. 98, no. 51, pp. 13669–13679, 2002.

[17] A. Manikandan, E. Manikandan, S. Vadivel, M. Kumaravel, D. Maruthamani, and S. Hariganesh, "Photocatalysis: Present, past and future," *Organic Pollutants in Wastewater I*, p. 183, 2018.

[18] B. Das, H. N. Dhara, A. Dahiya, and B. K. Patel, "Recent advances in photocatalytic degradation of dyes using heterogeneous catalysts," *Trends and Contemporary Technologies for Photocatalytic Degradation of Dyes*, pp. 21–64, 2022.

[19] T. Jones, J. Edwards, and J. Kallioinen, "Titanium compounds, inorganic," *Kirk-Othmer Encyclopedia of Chemical Technology*, pp. 1–76, 2000.

[20] D. A. Hanaor and C. C. Sorrell, "Review of the anatase to rutile phase transformation," *Journal of Materials science*, vol. 46, pp. 855–874, 2011.

[21] H. Shi, R. Magaye, V. Castranova, and J. Zhao, "Titanium dioxide nanoparticles: a review of current toxicological data," *Particle and fibre toxicology*, vol. 10, pp. 1–33, 2013.

[22] Z. Hiroi, "Inorganic structural chemistry of titanium dioxide polymorphs," *Inorganic Chemistry*, vol. 61, no. 22, pp. 8393–8401, 2022.

[23] F. Scarpelli, T. F. Mastropietro, T. Poerio, and N. Godbert, "Mesoporous tio2 thin films: State of the art," *Titanium Dioxide-Material for a Sustainable Environment*, vol. 508, no. 1, pp. 135–142, 2018.

[24] L. E. Oi, C. Yee, H. Lee, H. C. Ong, S. B. Abd Hamid, and J. C. Juan, "Recent advances of titanium dioxide (tio2) for green organic synthesis," *RSC Advances*, vol. 6, pp. 108741–108754, 11 2016.

[25] X. Bi, G. Du, A. Kalam, D. Sun, Y. Yu, Q. Su, B. Xu, and A. G. Al-Sehemi, "Tuning oxygen vacancy content in tio2 nanoparticles to enhance the photocatalytic performance," *Chemical Engineering Science*, vol. 234, p. 116440, 2021.

[26] K. Ozawa, M. Emori, S. Yamamoto, R. Yukawa, S. Yamamoto, R. Hobara, K. Fujikawa, H. Sakama, and I. Matsuda, "Electron–hole recombination time at tio2 single-crystal surfaces: Influence of surface band bending," *The Journal of Physical Chemistry Letters*, vol. 5, no. 11, pp. 1953–1957, 2014.

[27] V. Dal Santo and A. Naldoni, "Titanium dioxide photocatalysis," 2018.

[28] A. J. Haider, Z. N. Jameel, and I. H. Al-Hussaini, "Review on: titanium dioxide applications," *Energy Procedia*, vol. 157, pp. 17–29, 2019.

[29] A. J. Haider, Z. N. Jameel, and S. Y. Taha, "Synthesis and characterization of tio2 nanoparticles via sol-gel method by pulse laser ablation," *Eng. & Tech. Journal*, vol. 33, no. 5, pp. 761–771, 2015.

[30] X. Chen and S. S. Mao, "Titanium dioxide nanomaterials: synthesis, properties, modifications, and applications," *Chemical reviews*, vol. 107, no. 7, pp. 2891–2959, 2007.

[31] M. Parashar, V. K. Shukla, and R. Singh, "Metal oxides nanoparticles via sol–gel method: a review on synthesis, characterization and applications," *Journal of Materials Science: Materials in Electronics*, vol. 31, pp. 3729–3749, 2020.

[32] L. L. Hench and J. K. West, "The sol-gel process," *Chemical reviews*, vol. 90, no. 1, pp. 33–72, 1990.

[33] M. Niederberger and N. Pinna, *Metal oxide nanoparticles in organic solvents: synthesis, formation, assembly and application*. Springer Science & Business Media, 2009.

[34] L. L. Hench and R. Orefice, "Sol–gel technology," *Kirk-Othmer Encyclopedia of Chemical Technology*, 2000.

[35] M. Guglielmi and G. Carturan, "Precursors for sol-gel preparations," *Journal of Non-Crystalline Solids*, vol. 100, no. 1-3, pp. 16–30, 1988.

[36] A. E. Danks, S. R. Hall, and Z. Schnepp, "The evolution of 'sol–gel'chemistry as a technique for materials synthesis," *Materials Horizons*, vol. 3, no. 2, pp. 91–112, 2016.

[37] N. Thongdee, S. Watcharamaisakul, and B. Golman, "Effect of peptizing agent concentration on morphology of unsupported alumina membrane," in *Key Engineering Materials*, vol. 766, pp. 71–76, Trans Tech Publ, 2018.

[38] D. Naseer, J.-H. Ha, J. Lee, C. Park, and I.-H. Song, "Effect of the peptization process and thermal treatment on the sol-gel preparation of mesoporous α-alumina membranes," *Membranes*, vol. 12, no. 3, p. 313, 2022.

[39] H. A. Mahmoud, K. Narasimharao, T. T. Ali, and K. M. Khalil, "Acidic peptizing agent effect on anatase-rutile ratio and photocatalytic performance of tio2 nanoparticles," *Nanoscale Research Letters*, vol. 13, pp. 1–13, 2018.

[40] K.-N. P. Kumar, J. Kumar, and K. Keizer, "Effect of peptization on densification and phase-transformation behavior of sol–gel-derived nanostructured titania," *Journal of the American Ceramic Society*, vol. 77, no. 5, pp. 1396–1400, 1994.

[41] B. Bonelli, S. Esposito, F. S. Freyria, *et al.*, "Mesoporous titania: Synthesis, properties and comparison with non-porous titania," *Titanium dioxide*, pp. 119–141, 2017.

[42] Q. Dai, L. Shi, Y. Luo, J. Blin, D. Li, C. Yuan, and B. Su, "Effects of templates on the structure, stability and photocatalytic activity of mesostructured tio2," *Journal of Photochemistry and Photobiology A: Chemistry*, vol. 148, no. 1-3, pp. 295–301, 2002.

[43] R. G. Toro, A. M. Adel, T. de Caro, B. Brunetti, M. T. Al-Shemy, and D. Caschera, "A facile one-pot approach to the fabrication of nanocellulose–titanium dioxide nanocomposites with promising photocatalytic and antimicrobial activity," *Materials*, vol. 15, no. 16, p. 5789, 2022.

[44] H.-F. Zuo, Y.-R. Guo, S.-J. Li, and Q.-J. Pan, "Application of microcrystalline cellulose to fabricate zno with enhanced photocatalytic activity," *Journal of alloys and compounds*, vol. 617, pp. 823–827, 2014.

[45] C. Colleoni *et al.*, "Sol-gel synthesis and hybrid thin film deposition for innovative textile finishing. study, characterization and environmental impact evaluation," 2012.

[46] S. A. Hasan, M. N. Siddique, and M. A. Islam, "Influence of solvent type on the synthesis and properties of tio2 nanoparticles via sol-gel method," *Journal of Sol-Gel Science and Technology*, vol. 79, no. 3, pp. 455–463, 2016.

[47] Y. Gao, J. Jiang, X. Zhou, and Y. Zhang, "Effect of ph value on morphology and photo-

catalytic activity of tio2 nanoparticles synthesized by sol-gel method," *Journal of Sol-Gel Science and Technology*, vol. 64, pp. 39–45, 2012.

[48] M. Mazloom-Jalali, H. Tavakoli, and F. Golestani-Fard, "Effect of ph on optical properties of tio2 thin films prepared by sol-gel method," *Journal of Sol-Gel Science and Technology*, vol. 54, pp. 125–131, 2010.

[49] Y. Shen, H. Xie, and X. Peng, "Influence of temperature on the microstructure and properties of nanosized titanium dioxide thin films prepared by sol-gel method," *Journal of Sol-Gel Science and Technology*, vol. 56, pp. 239–243, 2010.

[50] L. M. Liu, J. M. Bai, and J. F. Zhou, "Effect of synthesis method on the particle size and morphology of nanocrystalline titanium dioxide powders," *Journal of Materials Science and Technology*, vol. 16, no. 6, pp. 493–496, 2000.

[51] D. J. Shaw, D. C. Bradley, and A. J. Wilson, "A comparative study of normal and reverse addition techniques in the sol–gel synthesis of sio2 and tio2," *Journal of Sol-Gel Science and Technology*, vol. 36, no. 2, pp. 175–182, 2005.

[52] M. J. Rosen and M. Dahanayake, *Industrial utilization of surfactants: principles and practice*. American Oil Chemists' Society, 2000.

[53] M. J. Rosen and J. T. Kunjappu, *Surfactants and Interfacial Phenomena*. Wiley, 3rd ed., 2004.

[54] S. Savic, I. Pantelic, M. Lukic, B. Markovic, and J. Milic, "Behind the alkyl polyglucoside-based structures: Lamellar liquid crystalline and lamellar gel phases in different emulsion systems," in *Alkyl Polyglucosides*, pp. 21–52, Elsevier, 2014.

[55] H. Uchida, M. N. Patel, R. A. May, G. Gupta, K. J. Stevenson, and K. P. Johnston, "Highly-ordered mesoporous titania thin films prepared via surfactant assembly on conductive indium–tin-oxide/glass substrate and its optical properties," *Thin Solid Films*, vol. 518, no. 12, pp. 3169–3176, 2010.

[56] J. Yang, H. Peterlik, M. Lomoschitz, and U. Schubert, "Preparation of mesoporous titania by surfactant-assisted sol–gel processing of acetaldoxime-modified titanium alkoxides," *Journal of non-crystalline solids*, vol. 356, no. 25-27, pp. 1217–1227, 2010.

[57] P. Kluson, P. Kacer, T. Cajthaml, and M. Kalaji, "Preparation of titania mesoporous materials using a surfactant-mediated sol–gel methodelectronic supplementary information (esi) available: comments on gel preparation and high resolution n2 adsorption and desorption isotherms at 77 k on the surface of sfe (mode-3) gel. see http://www. rsc.

org/suppdata/jm/b0/b004760k," *Journal of Materials Chemistry*, vol. 11, no. 2, pp. 644–651, 2001.

[58] H. Choi, E. Stathatos, and D. D. Dionysiou, "Synthesis of nanocrystalline photocatalytic tio2 thin films and particles using sol–gel method modified with nonionic surfactants," *Thin Solid Films*, vol. 510, no. 1-2, pp. 107–114, 2006.

[59] J. A. Jebasingh, R. Stanley, and S. M. Vidyavathy, "Sol-gel preparation of surfactants assisted titania for solar photocatalysis," *Materials Letters*, vol. 279, p. 128460, 2020.

[60] Y. Zhang, Y. Yang, J. Zhao, R. Tan, P. Cui, and W. Song, "Preparation of zno nanoparticles by a surfactant-assisted complex sol–gel method using zinc nitrate," *Journal of sol-gel science and technology*, vol. 51, pp. 198–203, 2009.

[61] A. Antonello, G. Soliveri, D. Meroni, G. Cappelletti, and S. Ardizzone, "Photocatalytic remediation of indoor pollution by transparent tio2 films," *Catalysis today*, vol. 230, pp. 35–40, 2014.

[62] O. Galkina, V. Vinogradov, A. Agafonov, and A. Vinogradov, "Surfactant-assisted sol-gel synthesis of tio2 with uniform particle size distribution," *International Journal of Inorganic Chemistry*, vol. 2011, 2011.

[63] L. Singh, S. Bhattacharyya, G. Mishra, and S. Ahalawat, "Functional role of cationic surfactant to control the nano size of silica powder," *Applied nanoscience*, vol. 1, pp. 117–122, 2011.

[64] R. J. Moon, A. Martini, J. Nairn, J. Simonsen, and J. Youngblood, "Cellulose nanomaterials review: structure, properties and nanocomposites," *Chemical Society Reviews*, vol. 40, no. 7, pp. 3941–3994, 2011.

[65] P. Chauhan, C. Hadad, A. Sartorelli, M. Zarattini, A. Herreros-López, M. Mba, M. Maggini, M. Prato, and T. Carofiglio, "Nanocrystalline cellulose–porphyrin hybrids: synthesis, supramolecular properties, and singlet-oxygen production," *Chemical Communications*, vol. 49, no. 76, pp. 8525–8527, 2013.

[66] M. A. S. Azizi Samir, F. Alloin, and A. Dufresne, "Review of recent research into cellulosic whiskers, their properties and their application in nanocomposite field," *Biomacromolecules*, vol. 6, no. 2, pp. 612–626, 2005.

[67] H. Kargarzadeh, M. Mariano, D. Gopakumar, I. Ahmad, S. Thomas, A. Dufresne, J. Huang, and N. Lin, "Advances in cellulose nanomaterials," *Cellulose*, vol. 25, pp. 2151–2189, 2018.

[68] O. Nechyporchuk, M. N. Belgacem, and J. Bras, "Production of cellulose nanofibrils: A review of recent advances," *Industrial Crops and Products*, vol. 93, pp. 2–25, 2016.

[69] M. Oprea and D. M. Panaitescu, "Nanocellulose hybrids with metal oxides nanoparticles for biomedical applications," *Molecules*, vol. 25, no. 18, p. 4045, 2020.

[70] M. Oprea and S. I. Voicu, "Recent advances in composites based on cellulose derivatives for biomedical applications," *Carbohydrate Polymers*, vol. 247, p. 116683, 2020.

[71] D. M. Panaitescu, D. M. Vuluga, H. Paven, M. D. Iorga, M. Ghiurea, I. Matasaru, and P. Nechita, "Properties of polymer composites with cellulose microfibrils," *Molecular Crystals and Liquid Crystals*, vol. 484, no. 1, pp. 86–452, 2008.

[72] D. M. Panaitescu, A. N. Frone, and C. Nicolae, "Micro-and nano-mechanical characterization of polyamide 11 and its composites containing cellulose nanofibers," *European Polymer Journal*, vol. 49, no. 12, pp. 3857–3866, 2013.

[73] X. Wang, Z. Yu, L. Jiao, H. Bian, W. Yang, W. Wu, H. Xiao, and H. Dai, "Aerogel perfusion-prepared h-bn/cnf composite film with multiple thermally conductive pathways and high thermal conductivity," *Nanomaterials*, vol. 9, no. 7, p. 1051, 2019.

[74] E. Vismara, G. Bertolini, C. Bongio, N. Massironi, M. Zarattini, D. Nanni, C. Cosentino, and G. Torri, "Nanocellulose from cotton waste and its glycidyl methacrylate grafting and allylation: Synthesis, characterization and adsorption properties," *Nanomaterials*, vol. 11, no. 2, p. 476, 2021.

[75] A. Ivanova, K. Fominykh, D. Fattakhova-Rohlfing, P. Zeller, M. Doblinger, and T. Bein, "Nanocellulose-assisted formation of porous hematite nanostructures," *Inorganic Chemistry*, vol. 54, no. 3, pp. 1129–1135, 2015.

[76] A. Ivanova, M. C. Fravventura, D. Fattakhova-Rohlfing, J. Rathousky, L. Movsesyan, P. Ganter, T. J. Savenije, and T. Bein, "Nanocellulose-templated porous titania scaffolds incorporating presynthesized titania nanocrystals," *Chemistry of Materials*, vol. 27, no. 18, pp. 6205–6212, 2015.

[77] S. Obregón and V. Rodríguez-González, "Photocatalytic tio 2 thin films and coatings prepared by sol–gel processing: A brief review," *Journal of Sol-Gel Science and Technology*, pp. 1–17, 2021.

[78] "Dip coating technology." `http://www.apexicindia.com/technologies/dip-coating-technology`. Accessed: March 9, 2023.

[79] C. Su, B.-Y. Hong, and C.-M. Tseng, "Sol–gel preparation and photocatalysis of titanium dioxide," *Catalysis today*, vol. 96, no. 3, pp. 119–126, 2004.

[80] M. Lal, P. Sharma, and C. Ram, "Calcination temperature effect on titanium oxide (tio2) nanoparticles synthesis," *Optik*, vol. 241, p. 166934, 2021.

[81] C.-C. Wang and J. Y. Ying, "Sol- gel synthesis and hydrothermal processing of anatase and rutile titania nanocrystals," *Chemistry of materials*, vol. 11, no. 11, pp. 3113–3120, 1999.

[82] D. Dastan, S. L. Panahi, and N. B. Chaure, "Characterization of titania thin films grown by dip-coating technique," *Journal of Materials Science: Materials in Electronics*, vol. 27, pp. 12291–12296, 2016.

[83] N. Arconada, Y. Castro, and A. Durán, "Photocatalytic properties in aqueous solution of porous tio2-anatase films prepared by sol–gel process," *Applied Catalysis A: General*, vol. 385, no. 1-2, pp. 101–107, 2010.

[84] U. Černigoj, U. L. Štangar, P. Trebše, U. O. Krašovec, and S. Gross, "Photocatalytically active tio2 thin films produced by surfactant-assisted sol–gel processing," *Thin Solid Films*, vol. 495, no. 1-2, pp. 327–332, 2006.

[85] G. Liu, Z. Jin, X. Liu, T. Wang, and Z. Liu, "Anatase tio 2 porous thin films prepared by sol-gel method using ctab surfactant," *Journal of sol-gel science and technology*, vol. 41, pp. 49–55, 2007.

[86] J. Krỳsa, M. Baudys, M. Zlámal, H. Krỳsová, M. Morozová, and P. Klusoň, "Photocatalytic and photoelectrochemical properties of sol–gel tio2 films of controlled thickness and porosity," *Catalysis Today*, vol. 230, pp. 2–7, 2014.

[87] D. Spini, "Green synthesis and characterization of tio_2 sol-gel for self-cleaning surfaces," 2021.

[88] Available at - `https://umaine.edu/pdc/nanocellulose/`, Accessed 2023.

[89] N. Corporation, "Ncsu033b-e data sheet." `https://led-ld.nichia.co.jp/api/data/spec/tech/NCSU033B-E.pdf`, 2023. Accessed on: 14 March 2023.

[90] T. Scientific™, "Spectronic™ 200 spectrophotometer." `https://www.thermofisher.com/order/catalog/product/840-281700`, 2023. Accessed on: 15 March 2023.

[91] BRL Test Inc., "Uv-radiometer um-10." `https://www.brltest.com/pdf/pdf_meters/2699.pdf`, 2018. Technical Manual, accessed on: 15 March 2023.

[92] K. Akhtar, S. A. Khan, S. B. Khan, and A. M. Asiri, "Scanning electron microscopy: Principle and applications in nanomaterials characterization," *Handbook of materials characterization*, pp. 113–145, 2018.

[93] M. Abd Mutalib, M. Rahman, M. Othman, A. Ismail, and J. Jaafar, "Scanning electron microscopy (sem) and energy-dispersive x-ray (edx) spectroscopy," in *Membrane characterization*, pp. 161–179, Elsevier, 2017.

[94] E. Eiser, "Dynamic light scattering," *Multi Length-Scale Characterisation*, pp. 233–282, 2014.

[95] S. Brigatti, "A comparative study over differently produced titanium dioxide photocatalyst," 2021.

[96] H. Nishikiori, M. Hayashibe, and T. Fujii, "Visible light-photocatalytic activity of sulfate-doped titanium dioxide prepared by the sol- gel method," *Catalysts*, vol. 3, no. 2, pp. 363–377, 2013.

[97] S. Yamazaki, N. Fujinaga, and K. Araki, "Effect of sulfate ions for sol–gel synthesis of titania photocatalyst," *Applied Catalysis A: General*, vol. 210, no. 1-2, pp. 97–102, 2001.

A | Appendix A

In the following table (Table A.1), all the synthesis parameters, procedures and materials are reported to offer a complete and detailed description of the experimental procedure followed in this work.

For all the nanocellulose-based sol-gels, the relative molar amount of solvent reported is referred to the amount of water and nanocellulose for which the molecular weight of water is used for the calculation.

All the CNF-based formulations have been prepared starting from the CNF suspension preparation. This was done by diluting the 3% slurry to the desired level (1:50, 1:100, 1:200, 1:300) in order to obtain 36 g (or 27 g) of the suspension used as the solvent for the sol-gel synthesis. The mass of CNF reported in Table A.1 refers to the mass of slurry containing 3% of nanocellulose fibers and 97% of water.

All the CNC-based sol-gels were synthesized starting from the preparation of the nanocellulose suspension, similarly to the aforementioned case. For the CNC formulations, the mass reported in Table A.1 refers to the weight of CNC suspension obtained from the acid hydrolysis, hence, containing 0.7% of cellulose nanocrystals and 99.3% of water.

Table A.1: Prepared sol-gels list.

Sol-gel	TTIP [g]	Solvent [g]	Chelating agent [g]	Surfactant/Templating agent [g]	Molar ratio
W-T10-R-I	5.68	36.00 H_2O	6.00 AA	-	1:100:5
I-T10-L20-N	5.68	54.09 *i*-PrOH	6.00 AA	1.88 Lutensol ON70	1:45:5:0.2
I-T12-L20-N	6.82	54.09 *i*-PrOH	6.00 AA	1.88 Lutensol ON70	1.2:45:5:0.2
I-T10-S20-N	5.68	54.09 *i*-PrOH	6.00 AA	1.15 SDS	1:45:5:0.2
I-T12-S20-N	6.82	54.09 *i*-PrOH	6.00 AA	1.15 SDS	1.2:45:5:0.2
I-T10-E50-N	5.68	54.09 *i*-PrOH	6.00 AA	0.50 Ecosurf eh-3	1:45:5:x
I-T12-E50-N	6.82	54.09 *i*-PrOH	6.00 AA	0.50 Ecosurf eh-3	1.2:45:5:x
E-T10-L7-R	5.68	36.86 EtOH	1.20 AA	0.66 Lutensol ON70	1:40:1:0.07
E-T10-S5-R	5.68	36.86 EtOH	1.20 AA	0.29 SDS	1:40:1:0.05
I-T12-L20-R	6.82	54.09 *i*-PrOH	6.00 AA	1.88 Lutensol ON70	1.2:45:5:0.2
I-T12-S20-R	6.82	54.09 *i*-PrOH	6.00 AA	1.15 SDS	1.2:45:5:0.2
W-T10-F200-R	5.68	35.82 H_2O	6.00 AA	0.18 CNF 3%	1:100:5
W-T12-F200-R	6.82	35.82 H_2O	6.00 AA	0.18 CNF 3%	1:100:5
I-T12-L20-N-U	6.82	54.09 *i*-PrOH	6.00 AA	1.88 Lutensol ON70	1.2:45:5:0.2
E-T10-L7-R-U	5.68	36.86 EtOH	1.20 AA	0.66 Lutensol ON70	1:40:1:0.07
W-T12-L20-N	6.82	36.00 H_2O	6.00 AA	1.88 Lutensol ON70	1.2:100:5:0.2
W-T12-E5-N	6.82	36.00 H_2O	6.00 AA	0.05 Ecosurf eh-3	1.2:100:5:x
W-T10-F50-R	5.68	35.30 H_2O	6.00 AA	0.70 CNF 3%	1:100:5
W-T10-F100-R	5.68	35.64 H_2O	6.00 AA	0.36 CNF 3%	1:100:5
W-T10-F300-R	5.68	35.88 H_2O	6.00 AA	0.12 CNF 3%	1:100:5
LA12M2	28.13	206.38 EtOH	0.40 HCl	0.47 Lutensol ON70	-
W75-T10-F50-R	5.68	26.47 H_2O	6.00 AA	0.53 CNF 3%	1:75:5
W75-T10-F100-R	5.68	26.73 H_2O	6.00 AA	0.27 CNF 3%	1:75:5
W75-T10-F300-R	5.68	26.91 H_2O	6.00 AA	0.09 CNF 3%	1:75:5
LA14M3	28.13	206.38 EtOH	0.40 HCl	0.47 Lutensol ON70	-
W-T15-E5-N	8.52	36.00 H_2O	6.00 AA	0.05 Ecosurf eh-3	1.5:100:5:x
W-T10-F100-R-V1	5.68	35.64 H_2O	6.00 AA	0.36 CNF 3%	1:100:5
W-T10-F300-R-V1	5.68	35.88 H_2O	6.00 AA	0.12 CNF 3%	1:100:5
W-T10-F200-R-V1	5.68	35.82 H_2O	6.00 AA	0.18 CNF 3%	1:100:5
W-T12-F200-R-V1	6.82	35.82 H_2O	6.00 AA	0.18 CNF 3%	1:100:5
W-T12-E5-N-V1	6.82	36.00 H_2O	6.00 AA	0.05 Ecosurf eh-3	1.2:100:5:x
W-T10-C200-R	5.68	10.30 H_2O	6.00 AA	25.70 CNC 0.70%	1:100:5
W-T10-C150-R	5.68	1.79 H_2O	6.00 AA	34.21 CNC 0.70%	1:100:5
W-T10-C150-R-I	5.68	1.79 H_2O	6.00 AA	34.21 CNC 0.70%	1:100:5
W-T12-C150-R-I	6.82	1.79 H_2O	6.00 AA	34.21 CNC 0.70%	1:100:5
W-T10-C6-R	5.68	35.23 H_2O	6.00 AA	0.77 CNC 0.70%	1:100:5
W-T10-C3-R	5.68	34.46 H_2O	6.00 AA	1.54 CNC 0.70%	1:100:5
W-T10-C3-R-I	5.68	34.46 H_2O	6.00 AA	1.54 CNC 0.70%	1:100:5
W-T12-C3-R-I	6.82	34.46 H_2O	6.00 AA	1.54 CNC 0.70%	1:100:5
W-T12-E5-N-V2	6.82	36.00 H_2O	6.00 AA	0.05 Ecosurf eh-3	1.2:100:5:x
W-T10-C6-RV1	5.68	35.23 H_2O	6.00 AA	0.77 CNC 0.70%	1:100:5
W-T10-C3-R-V1	5.68	34.46 H_2O	6.00 AA	1.54 CNC 0.70%	1:100:5
W-T10-C3-R-I-V1	5.68	34.46 H_2O	6.00 AA	1.54 CNC 0.70%	1:100:5
W-T12-C3-R-I-V1	6.82	34.46 H_2O	6.00 AA	1.54 CNC 0.70%	1:100:5

List of Figures

1.1 Rhodamine B chemical structure. 3
1.2 Main methods used for dye-polluted wastewater treatment [7]. 5
1.3 Valence and conduction bands in: conductors, semiconductors and insulators [12]. 5
1.4 Schematic representation of the electron-hole pair through the absorption of light. (E_g=bandgap energy, vb=valence band, cb=conduction band) [11]. 6
1.5 Fields of application of photocatalysis [18]. 8
1.6 Crystal structures of TiO_2 three polymorphs: (a) rutile; (b) anatase; (c) brookite [22]. 9
1.7 Oxygen vacancies (coloured in magenta) present inside the crystal lattice of TiO_2. Ti atoms are coloured in blue and O atoms are coloured in yellow [25]. . 10
1.8 Schematic representation of the TiO_2 photocatalytic process [13]. 12
1.9 Steps of the sol-gel method for the preparation of metal oxide nanoparticles [31]. 16
1.10 Scheme of the possible sol-gel process routes and steps to tailor the final product's morphology [11]. 17
1.11 Scheme of the soft and hard template-assisted synthesis of TiO_2 controlled mesoporous strcutures [41]. 21
1.12 (a) General representation of a surfactant molecule; (b) micellar structures formed from the self-organization of the surfactant molecules [11]. 24
1.13 Typical structures of common non-ionic surfactants: a) polyethylene ethoxylate, b) alkyl polyglucoside. (R=alkyl chain, DP=degree of polymerization) [11, 54]. 25
1.14 Chemical structure of the cellulose repeating unit; in the picture the directionality of the β-1,4 glucosidic bond and the intramolecular hydrogen bonds (dashed line) are highlighted [64]. 27
1.15 AFM images of (a) cellulose nanofibrils (CNF) and (b) cellulose nanocrystals (CNC) [69, 72, 73]. 28

1.16 Schematic illustration of the most commonly used techniques to obtain thin films from sol-gel solutions: a) dip-coating, b) spin-coating, c) spray coating, d) electrophoretic deposition. (Adapted from [77]). 30
1.17 Schematic illustration of the dip-coating process highlighting the main stages: a) dipping of the substrate, b) withdrawal of the substrate, c) draining and evaporation of the solvent [77]. 31

2.1 TTIP molecular structure. 36
2.2 Sodium dodecyl sulfate molecular structure. 38
2.3 a) SEM image of Maine University cellulose nanofibers; b) 3% CNF slurry appearance [88]. 40
2.4 Sulfuric acid molecular structure. 41
2.5 General code for the prepared sol-gel formulations denomination. 44
2.6 Falc ultrasonic bath. 46
2.7 a) Dip coater apparatus, b) Arduino code to control the instrument speed. . . . 48
2.8 GEFRAN 1200 muffle-type oven. 50
2.9 UV-LED photocatalytic degradation test laboratory setup. 51
2.10 Emission spectrum of Nichia NCSU033B UV SMD-LED [89]. 52
2.11 Spectrophotometer Thermo Scientific^{TM} SPECTRONIC^{TM} 200E [90]. 52
2.12 ULTRA-VITALUX 300W E27 solar lamp. 54
2.13 Konica Minolta UM-10 optical power meter [91]. 54
2.14 UV-VIS photocatalysis laboratory setup. 55
2.15 Scanning electron microscope EVO 50 Extended Pressure by Zeiss. 57
2.16 Two-step process for the EDX x-ray generation. First, the energy transferred to the atomic electron knocks it off, leaving behind a hole. Second, its position is filled by another electron from a higher energy shell, and the characteristic x-ray is released [93]. 58
2.17 Bruker XFlash® 6-30 EDX detector. 58
2.18 General DLS setup. (I_{in}=incident light intensity, λ=monochromatic light wavelength, θ=scattering angle) [94]. 59
2.19 Typical spectrum for the particles size distribution, output of the DLS measurement. 60
2.20 Zetasizer Nano ZS by Malvern Analytical. 60

3.1 Appearance of synthesized CNC suspension. 62
3.2 Size distribution by intensity plot of CNC synthesized via acid hydrolysis, output of the DLS analysis. 62

3.3 Example: collection of absorbance data in a typical UV-VIS photocatalysis test. Highlighted in red: real absorbance obtained subtracting the tare of the cuvette from the average value. 64
3.4 Example: ΔC% vs t plot for a sample tested 4 times across 8 weeks. 65
3.5 Example: $\ln(C/C_0)$ vs t plot for a sample tested 4 times across 8 weeks. 65
3.6 Example: kinetic constant values for each 2-week measurement. 66
3.7 Shorter caption 67
3.8 Comparison between the photolysis tests that produced the most degradation and an average photocatalysis test. 68
3.9 Results comparison of UV-VIS photocatalysis for isopropanol and SDS based sol-gels. Each plot compares the results obtained at the same amount of ageing time, namely 2 (top left), 4 (top right), 6 (bottom left), 8 (bottom right) weeks. . 70
3.10 Results comparison between the obtained kinetic constants *k* for the isopropanol and SDS based sol-gels at 2, 4, 6, 8 weeks. 71
3.11 Segregation of an isopropanol and SDS based sol-gel (I-T12-S20-N) at the 4th week. 72
3.12 Bulk crystallization at the bottom of the beaker containing an isopropanol and Ecosurf eh-3 based sol-gel (I-T12-E50-N) at the 2nd week. 73
3.13 $\ln(C/C_0)$ vs time plot of isopropanol and Ecosurf eh-3 based sol-gels at the 2nd week compared with the known sample "X". 74
3.14 Results comparison between the obtained kinetic constants *k* for the isopropanol and Ecosurf eh-3 based sol-gels at 2 weeks and known sol-gel "X". 74
3.15 Results comparison of UV-VIS photocatalysis for isopropanol and Lutensol ON70 based sol-gels. Each plot compares the results obtained at the same amount of ageing time, namely 2 (top left), 4 (top right), 6 (bottom left), 8 (bottom right) weeks. 75
3.16 Results comparison between the obtained kinetic constants *k* for the isopropanol and Lutensol ON70 based sol-gels at 2, 4, 6, 8 weeks. 76
3.17 Appearence of an isopropanol and Lutensol ON70 based sol-gel (I-T12-L20-N) at the 2nd week. No visible precipitation is present. 76
3.18 Precipitation of TiO_2 particles inside an isopropanol and Lutensol ON70 based sol-gel (I-T12-L20-N) at the 4th week. 77
3.19 Bulk precipitation of TiO_2 particles inside an isopropanol and Lutensol ON70 based sol-gel (I-T12-L20-R) at the 2nd week. 78
3.20 Aesthetic appearance of samples I-T12-L20-N (a) and I-T12-S20-R (b). 78
3.21 Precipitation of TiO_2 crystals inside sol-gel LA12M2. 79

3.22 Results comparison of UV-VIS photocatalysis for ethanol based sol-gels. Each plot compares the results obtained at the same amount of ageing time, namely 2 (top left), 4 (top right), 6 (bottom left), 8 (bottom right) weeks. 80
3.23 Results comparison between the obtained kinetic constants *k* for the ethanol based sol-gels at 2, 4, 6, 8 weeks. 81
3.24 Aesthetic appearance of samples LA14M3 (a) and E-T10-L7-R (b). 82
3.25 Results comparison between the obtained kinetic constants *k* for the ultrasonicated sol-gels at 1, 2, 3, 4 weeks and the ones obtained for the non-ultrasonicated versions at 2, and 4 weeks, tested with UV-VIS photocatalysis. 83
3.26 Results of UV-VIS photocatalytic test of sol-gel W-T10-R-I at 2, 4, 6 weeks. . . 85
3.27 UV-VIS obtained kinetic constants *k* for sol-gel W-T10-R-I at 2, 4, 6 weeks. . . 85
3.28 Results comparison of UV-VIS photocatalysis for the first water and surfactant based sol-gels. Each plot compares the results obtained at the same amount of ageing time, namely 2 (top left), 4 (top right), 6 (bottom) weeks. 87
3.29 Results comparison between the obtained kinetic constants *k* for the first water and surfactant based sol-gels at 2, 4, 6 weeks, tested with UV-VIS photocatalysis. 87
3.30 Results comparison between the obtained kinetic constants *k* for sol-gels W-T12-L20-N and W-T12-E5-N at 2, 4, 6 weeks, tested with UV-LED photocatalysis. 88
3.31 Results comparison of UV-VIS photocatalysis for the new and repeated water and Ecosurf eh-3 based sol-gels. Each plot compares the results obtained at the same amount of ageing time, namely 2 (top left), 4 (top right), 6 (bottom) weeks. 89
3.32 Results comparison between the obtained kinetic constants *k* for the new and repeated water and Ecosurf eh-3 based sol-gels at 2, 4, 6 weeks, tested with UV-VIS photocatalysis. 90
3.33 Aesthetic appearance of samples W-T12-L20-N (a) and W-T12-E5-N (b). . . . 91
3.34 Results comparison of UV-VIS photocatalysis for water and CNF based sol-gels. Each plot compares the results obtained at the same amount of ageing time, namely 2 (top left), 4 (top right), 6 (bottom left), 8 (bottom right) weeks. . 92
3.35 Results comparison between the obtained kinetic constants *k* for the water and CNF based sol-gels at 2, 4, 6, 8 weeks. 92
3.36 Results comparison between the obtained kinetic constants *k* for the CNF based sol-gels formulated with a lower amount of solvent and sol-gel W-T10-F50-R at 2 weeks. 93
3.37 Results comparison of UV-VIS photocatalysis for water and CNF based sol-gels. Each plot compares the results obtained at the same amount of ageing time, namely 2 (top left), 4 (top right), 6 (bottom) weeks. 95

3.38 Results comparison between the obtained kinetic constants k for the water and CNF based sol-gels at 2, 4, 6 weeks. 95
3.39 Aesthetic appearance of samples W-T10-F200-R (a) and W-T12-F200-R (b). . 96
3.40 Shorter caption 98
3.41 Shorter caption 99
3.42 Aesthetic appearance of samples W-T10-C3-R-I (a) and W-T12-C3-R-I (b). . . 100
3.43 Results comparison between the obtained kinetic constants k for some of the UV-VIS tested samples. 101
3.44 Results comparison between the best obtained kinetic constants k for the UV-LED tested surfactant-based samples. 102
3.45 Time evolution of UV-LED measured k for the water and Ecosurf eh-3 based sol-gels. (Adjacent columns refer to the same sample but at a different ageing week, namely week 2 (left column), week 4 (central column), and week 6 (right column)). 102
3.46 Results comparison between the obtained kinetic constants k for the UV-LED tested nanocellulose-based samples. 103
3.47 Size distribution by intensity plot of sol-gel I-T12-L20-N, output of the DLS analysis. 105
3.48 Size distribution by intensity plot of sol-gel I-T12-S20-N, output of the DLS analysis. 105
3.49 Size distribution by intensity plot of sol-gel W-T12-L20-N, output of the DLS analysis. 107
3.50 Size distribution by intensity plot of sol-gel W-T12-E5-N, output of the DLS analysis. 107
3.51 Size distribution by intensity plot of sol-gel W-T12-F200-R, output of the DLS analysis. 108
3.52 Size distribution by intensity plot of sol-gel W-T12-C3-R-I, output of the DLS analysis. 108
3.53 SEM images at different magnification levels of samples I-T12-L20-N (left) and E-T10-L7-R-U (right). 110
3.54 Thickness measurement using SEM for sample E-T10-L7-R-U. 111
3.55 SEM images at different magnification levels of samples E-T10-S5-R (left) and I-T20-S20-R (right). 111
3.56 EDX analysis of the particles present on the surface of sample E-T10-S5-R. On the left, the spectrum obtained from the particle analysis (F2); on the right, the spectrum obtained from the smoothly coated area (F3). Highlighted in red: sulfur peak position. 112

3.57 SEM images at different magnification levels of samples W-T12-E5-N (left) and W-T12-L20-N (right). 113
3.58 EDX analysis of the craters present on the surface of sample W-T12-E5-N. Highlighted in red: the analyzed crater zone. Highlighted in green: the peak of titanium. 114
3.59 SEM images at different magnification levels of samples W-T15-E5-N (left) and W-T12-E5-N-V1 (right). 115
3.60 SEM images at different magnification levels of samples W-T12-F200-R (left) and W-T12-C3-R-I-V1 (right). 116
3.61 UV-LED kinetic constant *k* at different amounts of TTIP for the different types of water-based formulations. 117
3.62 UV-LED kinetic constant *k* at different nanocellulose suspension dilution. . . . 118

List of Tables

1.1 TiO_2 polymorphs main properties [20, 23]. 10
1.2 The main applications exploiting TiO_2 photocatalytic properties [28]. 14
1.3 List of the most used surfactants in sol-gel formulations. 26
1.4 Formulations for the sol-gel synthesis of photocatalytic TiO_2 found from literature review. (TBT = titanium(IV) butoxide, DEA = diethanolamine, DCIP = 2,6-dichloroindophenol, TEOT = titanium ethoxide). 33

2.1 List of reagents used in sol-gel formulations. (Abv. = abbreviated). 35
2.2 TTIP properties. 36
2.3 Sodium dodecyl sulfate properties. 39
2.4 Lutensol® ON70 properties. (R=saturated, synthetic, short-chain fatty alcohol). 39
2.5 Ecosurf eh-3 properties. 40
2.6 3% CNF slurry properties [88]. 41
2.7 Sulfuric acid properties. 42
2.8 Some of the prepared sol-gel formulations. 45
2.9 Ultrasonicated sol-gel formulations. 48
2.10 Conversion values between the pulse speed and the dip speed. 49

3.1 Results of the evaporation tests to determine the % of solid present in the acid hydrolysis-synthesized CNC dispersion. 63
3.2 Volume and mass variation during UV-VIS photolysis tests. 68
3.3 Temperature increase monitored during the 2 hours ultrasonication procedure. . 83
3.4 Results of DLS analysis. 106

A.1 Prepared sol-gels list. 132

List of Symbols

Variable	Description	Unit
λ	Wavelength	nm
l	Optical path length	cm
ϵ	Molar Absorptivity	L/mol·cm
k	Kinetic constant	min^{-1} h^{-1}
t	Time	min h
T	Temperature	°C